Fiber-enhanced Raman spectroscopy in aqueous media

FRIEDRICH-SCHILLER-
UNIVERSITÄT
JENA

Dissertation

(kumulativ)

zur Erlangung des akademischen Grades doctor rerum naturalium (Dr. rer. nat.)

vorgelegt dem Rat der Chemisch-Geowissenschaftliche Fakultät der Friedrich-Schiller-Universität Jena

von M.Sc. Di Yan
geboren am 02.04.1987 in Henan, China

Gutachter:

1. Prof. Dr. Jürgen Popp

   Institute of Physical Chemistry and Abbe Center of Photonics,
   Friedrich-Schiller University Jena, Helmholtzweg 4, 07743 Jena,
   Germany

2. Prof. Dr. Markus A. Schmidt

   Leibniz Institute of Photonic Technology, Albert-Einstein-Str. 9,
   07745 Jena, Germany

Tag der Verteidigung: 16.01.2019

Zugl.: Dissertation, Friedrich-Schiller-Universität Jena, 2019

Table of Contents

Index of Abbreviations

BR	bilirubin
BV	biliverdin
CARS	coherent anti-Stokes Raman spectroscopy
FERS	fiber-enhanced Raman spectroscopy
HC-PCF	hollow-core photonic-crystal-fiber
LoD	limit-of-detection
NA	numerical aperture
NIR	near-infrared
PCF	photonic-crystal-fiber
RRS	resonance Raman spectroscopy
SERS	surface enhanced Raman spectroscopy
UV	ultraviolet
UV-RRS	ultraviolet-resonance Raman spectroscopy

List of Figures

Abstract

This dissertation focuses on the investigation and development of an optical biosensor based on fiber-enhanced Raman spectroscopy (FERS) that provides chemical selective and sensitive label-free detection of biomolecules. FERS has been achieved by using various types of liquid core optical fibers, which guide the light within the liquid sample and increase the interaction length with the analyte molecules. The first part of this dissertation explains the FERS technique in detail and describes the current state of research of FERS. Several essential characteristics, such as fiber length, attenuation, material and refractive index, are thoroughly discussed in considerations of Raman intensity enhancement. Liquid-core fibers formed with hollow-core photonic-crystal fibers (HC-PCFs) and polymer fibers are introduced and discussed, as they are the most important breakthroughs. The objective of this research is to develop a robust optical fiber platform based on Raman spectroscopy that shows potential for use in bio-analytical and clinical applications. In this work, I demonstrate a combination of UV-resonance Raman spectroscopy (UV-RRS) and liquid-core fibers, to increases the sensitivity for the detection of low-concentrated pharmaceuticals tremendously. This combined enhancement technique was applied for the detection of bile pigments for monitoring of diseases related to hyperbilirubinemia and hyperbiliverdinemia. Their poor optical quality strongly limits the performances of the polymer-based liquid-core fibers. Therefore, the implementation of HC-PCFs was explored in two different types of optical guiding. Waveguiding in the visible range is achieved for the first time in both kinds of liquid-filled HC-PCFs, and therefore the Raman scattering wavelengths are not anymore limited to the insensitive NIR range. In order to achieve easy-to-use and stable FERS devices for further development, the performance of HC-PCFs in the aspect of light-confinement was studied with the help of a specially designed multi-channel Raman chemical imaging. The optimal fiber length, spatial filtering, and optical coupling were thoroughly analyzed, and an automatic coupling system was developed. With the development of optical fibers, FERS shows increasing potential as a robust, fast, chemical selective and sensitive tool for the detection of biomolecules in clinical, pharmaceutical, and biological applications.

Zusammenfassung

Diese Dissertation beschäftigt sich mit der Erforschung und Entwicklung eines optischen Biosensors, basierend auf faserverstärkter Raman Spektroskopie (engl. fiber-enhanced Raman spectroscopy, FERS). Dieser Sensor ermöglicht die chemisch selektive, sensitive und markierungsfreie Detektion von Biomolekülen. FERS wurde durch den Einsatz von verschiedenen optischen Fasern mit flüssigkeitsgefülltem Hohlkern bewerkstelligt. Die Fasern führen das Licht innerhalb der flüssigen Probe und vergrößern so die Strecke, auf der das Licht mit den Analytmolekülen wechselwirkt. Der erste Teil dieser Dissertation erklärt die FERS-Technik detailliert und beschreibt den derzeitigen Stand der Forschung bzgl. FERS. In den Überlegungen zur Verstärkung der Raman-Intensität werden mehrere wesentliche Eigenschaften wie Länge, Dämpfung sowie Material und Brechungsindex der Faser berücksichtigt und ausführlich behandelt. Flüssigkeitsgefüllte Fasern auf der Basis von photonischen Kristallfasern (HC-PCFs) und Polymerfasern mit Hohlkern werden eingeführt und besprochen, da sie den größten wissenschaftlichen Durchbruch darstellen. Das Ziel dieser Forschung ist es, ein stabiles Setup für faserverstärkte Raman-spektroskopische Messungen zu entwickeln, das Potential für den Einsatz in bioanalytischen und klinischen Anwendungen aufweist. In dieser Arbeit zeige ich eine Kombination von UV-Resonanz Raman Spektroskopie (UV-RRS) und flüssigkeitsgefüllten Fasern, um die Sensitivität der Detektion von niedrig konzentrierten Pharmazeutika immens zu verstärken. Diese kombinierte Verstärkungsmethode wurde ebenfalls angewandt, um Blutabbau-Pigmente zu detektieren. Dies kann für die Überwachung von Krankheiten genutzt werden, die mit Hyperbilirubinämie und Hyperbiliverdinämie in Verbindung stehen. Die schlechte optische Qualität von Polymer-basierten flüssigkeitsgefüllten Fasern schränkt deren Leistungsfähigkeit stark ein. Daher wurde der Einsatz von HC-PCFs für zwei verschiedene Lichtleitungsmechanismen untersucht. Erstmalig wurde Wellenleitung im sichtbaren Bereich in beiden flüssigkeitsgefüllten Fasertypen erzielt. Folglich ist die Wellenlänge der Raman-Streuung nicht mehr auf den unempfindlichen NIR-Bereich beschränkt. Um ein FERS-Gerät für die Weiterentwicklung zu realisieren, das leicht zu handhaben und stabil ist, wurden die HC-PCFs bezüglich ihrer Fähigkeit zum Lichteinschluss untersucht. Diese Untersuchung wurde mit Hilfe eines speziell konzipierten Aufbaus für die Raman-spektroskopische chemische Bildgebung durchgeführt. Optimale Faserlänge, Raumfilterung und optische Koppelung wurden sorgfältig ausgewertet und ein automatisches Kopplungssystem wurde entwickelt. Mit der Weiterentwicklung optischer Fasern zeigt FERS steigendes Potential als stabile, schnelle, chemisch selektive und sensitive Messmethode zur Detektion von Biomolekülen in klinischen, pharmazeutischen und biologischen Anwendungen.

1. Introduction

1.1. Raman spectroscopy

Raman spectroscopy, named after Sir C.V. Raman [1], is a spectroscopic technique based on inelastic scattering of light and used to study vibrational, rotational, and other low-frequency modes in a molecular system. Raman spectroscopy is widely used to provide information on chemical structures, to identify substances by the characteristic spectral fingerprint, and to determine the amount of the target substance in the sample quantitatively. The samples for Raman spectroscopy can be used as solids, liquids or vapors, as bulk material or microstructure. Raman spectroscopy has been used widely in chemical characterization of different materials, and it is gaining popularity in the study of biological samples to provide rapid and accurate identification of biomolecules [2]. One of the reasons for the surge in biochemistry applications is the increasing availability of sophisticated Raman spectroscopy instrumentation. The recent developments of Raman spectroscopy in instrument technology have simplified the measurement and increased the performance greatly. As water yields only a very weak Raman spectrum, Raman spectroscopy is ideal for the analytes in the aqueous environment, which is not well possible with IR-absorption spectroscopy. Therefore, there is a rapid growth in the applications of this technique in biological and pharmaceutical research [3], and the need for a robust platform has also become very important.

The Raman effect has been studied for decades, and the physics behind it are well understood [4]. The Raman effect is caused by the inelastic scattering that occurs when the light of frequency v_0 is scattered by the molecules. The incoming electromagnetic wave can be presented as:

$$\vec{E} = \vec{E}_0 \cos(2\pi v_0 t) \qquad (1)$$

where $\vec{E}_0$ is the amplitude of the electric field and v_0 is the frequency of the incident light. The electric field $\vec{E}$ induces an electric dipole $\vec{\mu}_{ind}$ in the molecule.

$$\vec{\mu}_{ind} = \tilde{\alpha}(v)\,\vec{E} \qquad (2)$$

The tensor $\tilde{\alpha}(v)$ is known as the molecular polarizability, which describes how the electron charges are displaced by the oscillating electromagnetic field. A molecule made of *N* atoms has *3N* degrees of freedom in 3-dimensional space. For a non-linear molecule, there are 3 translational motions, *3N - 6* fundamental modes of vibration and 3 modes rotational motions. For a linear molecule, however, rotation around its own axis does not change the molecule. There are only 2 rotational degrees of freedom for a linear molecule, leaving *3N - 5* degrees of freedom for vibration. The mode Q_n (vibrational or rotational) in the molecule at frequency v_n (vibrational) or $\frac{v_n}{2}$ (rotational) with amplitude $\mathring{Q}_n$ can be expressed as:

$$Q_n = \mathring{Q}_n cos(2\pi v_n t) \qquad (3)$$

The polarizability can be expressed in Fourier series expansion for small the amplitudes (higher orders are ignored):

$$\tilde{\alpha}(v) = \tilde{\alpha}_0(v_0) + \sum_n \left(\frac{\partial \tilde{\alpha}}{\partial Q_n}\right) Q_n^{\circ} \cos(2\pi v_n t) \qquad (4)$$

Based on the equations above, the induced dipole moment can be derived as:

$$\vec{\mu}_{ind} = \tilde{\alpha}_0 \vec{E}_0 \cos(2\pi v_0 t) + \frac{1}{2}\vec{E}_0 \sum_n \left(\frac{\partial \tilde{\alpha}}{\partial Q_n}\right)_0 Q_n^{\circ} \cos(2\pi[v_0 + v_n]t) + \frac{1}{2}\vec{E}_0 \sum_n \left(\frac{\partial \tilde{\alpha}}{\partial Q_n}\right)_0 Q_n^{\circ} \cos(2\pi[v_0 - v_n]t) \qquad (5)$$

In the classical theory of Raman scattering, we assume that the polarized electrons will radiate light at their own oscillation frequencies. According to equation 5, the scattered light will be in three frequencies. The first term at the same frequency as the laser (Rayleigh scattering). The second term is anti-Stokes Raman scattering that occurs at $v_0 + v_n$, and the third term is Stokes scattering that occurs at $v_0 - v_n$.

The classical explanation gives some insights in Raman spectroscopy, but cannot explain the scattering at quantized states. A quantum mechanical explanation is needed, but beyond the short introduction in this thesis.

The populations of the various vibrational and rotational states of the molecules are governed by the temperature of the system, and anti-Stokes/Stokes intensity ratio is related to temperature by the Boltzmann distribution [3]:

$$\frac{I_R(v_0 + v_n)}{I_R(v_0 - v_n)} = \left(\frac{v_0 + v_n}{v_0 - v_n}\right)^4 e^{\frac{-hv_n}{kT}} \qquad (6)$$

where I_R is the scattering intensity, *k* is the Boltzmann constant, *T* is the temperature of the system, *h* is the Plank constant. Therefore, at room temperature (T = 293 K), the majority of Raman scattering will be Stokes Raman scattering, and anti-Stokes scattering will be much weaker. The experimental setups in this dissertation rely only on Stokes scattering.

Inelastic scattering is inherently weak, only one in every $10^6 - 10^8$ scattered photons [5]. Thus, it is necessary to exploit and develop enhancement methods which can be assigned to the factors in equation 7 [6].

$$I_R \propto I_0 N \sigma_R \propto I_0 N (v_0 \pm v_n)^4 |\alpha|^2 \qquad (7)$$

N is the number of scattering molecules, I_0 is the incoming excitation intensity, σ_R is the Raman scattering cross-section of that specific transition, and $|\alpha|$ is the magnitude of the molecule's polarizability tensor. As the number of molecules (N) is proportional to the concentration, the Raman intensity is linearly proportional to the concentration of the target analyte. Similarly, by increasing the sample volume involved in the measurement, the same goal can be achieved.

1.2. Fiber-enhanced Raman spectroscopy (FERS)

In the 1970s, scientists from Bell's lab first published the concept of Raman enhancement based on liquid core fiber, employing optical fibers to increase the laser path length in C_6H_6 and C_2Cl_4 [7]. This concept is also promising for the enhancement of the absorption of very weak absorbing analytes, and therefore efforts had followed this idea to construct liquid core optical fibers with organic solutions for enhancing the Raman or absorption spectra [8-14]. Compared to other Raman enhancement techniques, such as resonance Raman spectroscopy (RRS), surface enhanced

Raman spectroscopy (SERS) and coherent anti-Stokes Raman spectroscopy (CARS), fiber-enhanced Raman spectroscopy (FERS) has unique features:

1. The enhancement is non-selective to the Raman bands. As the enhancement is only the result of the increased number of molecules, all Raman peaks are enhanced evenly without shifting or broadening.

2. The efficiency of the sample usage is improved, and less amount of sample is required. In conventional Raman measurements, such as cuvette sensing, only molecules located in or close to the laser focus are excited. In contrast, the liquid sample in the fiber core is excited over an extended path length, and the scattered Raman signal is confined within the numerical aperture of the fiber and travels to the fiber end for collection. Therefore, FERS allows highly sensitive detection with a minimum amount of the liquid sample.

2. State of the art

2.1. Aims and objectives in the development of FERS

As water has a much lower refractive index than that of glass (n_{water}=1.33, n_{glass}=1.46), simple fused-silica capillary waveguides are not capable of forming guidance in a water core. With the purpose of employing FERS in monitoring biomolecules in aqueous media, the development of new types of fibers that compatible with low-refractive-index liquids is of key importance.

The performance of fiber-enhanced Raman spectroscopy (FERS) is mainly determined by the parameters of the liquid-core optical fiber, such as attenuation, length, core diameter, and operating spectral range. Other properties of the liquid core fiber, such as the bending radius and the chemical resistance, are also crucial to FERS.

Attenuation and length. In FERS, the laser intensity is not homogeneous along the fiber. The laser intensity decreases with the path length due to the fiber attenuation, as well as the back-scattered Raman signal. The effective fiber length, which is calculated from the physical fiber length of the waveguide and the transmission function, was considered instead of the physical fiber length [15, 16]:

$$L_{eff} = \int_0^{L_p} T_l(z) \cdot T_r(z)\, dz \qquad (8)$$

where L_{eff} is the effective length; $T_l(z)$ describes the ratio of the laser power at point z in the fiber to the power coupled into the fiber. Similarly, $T_r(z)$ is the ratio of the Raman power at the end face of the fiber to the Raman power at point z. Therefore, the effect of the attenuation over the physical fiber length is canceled out, and the fiber enhancement is proportional to the effective fiber length [15]. The transmission properties are assumed to be an exponential function:

$$\begin{cases} T_l(z) &= e^{-(\mu_{sl}+\varepsilon_l \cdot c)\cdot z} \\ T_r(z) &= e^{-(\mu_{sr}+\varepsilon_r \cdot c)\cdot z} \end{cases} \qquad (9)$$

where μ_{sl} and μ_{sr} are the attenuation coefficients that account for waveguide imperfections for the laser and the Raman-scattered wavelength respectively, ε_l is the extinction coefficient at the laser wavelength, ε_r is the extinction coefficient at the Raman-scattered wavelength, c is the concentration of the light absorbing solute.

When the fiber is filled with the non-absorbing sample or low-concentrated absorbing sample, the effective length is limited by the loss coefficients:

$$\lim_{L_p \to \infty} L_{eff}\left(L_p\right) = \frac{1}{\mu_{sl} + \mu_{sr}} \qquad (10)$$

For example, when the liquid core fiber has an attenuation of 5 dB/m for both excitation and scattering wavelengths, a 20 cm fiber piece has an effective length of 3.9 cm, a 50 cm or even longer fiber piece has an effective length of 4.3 cm (close to the limit). Low attenuation is of key importance to FERS. Strong fiber enhancement will not be possible without a long effective path length of the light in the fiber.

Numerical aperture (NA). As the laser propagates through the liquid core, it interacts with the molecules. The induced Raman scattering from a molecule in the fiber core is a point source which emits light in all directions. The fiber can only confine the light beams in the cones of the acceptance half-angle and guide the radiation to backward and forward directions. In FERS setups demonstrated in this work, only backward guided Raman radiation is collected. Therefore, the maximum efficiency of the collection is 50% at NA = 1. The function of the collection efficiency is:

$$E = \frac{1 - \cos(2 \sin^{-1}(NA))}{2} \times 100\% \qquad (11)$$

Spectral range. In Raman sensing of biomolecules, excitation wavelengths from deep-UV to NIR are all practical. UV-resonance Raman spectroscopy (UV-RRS) is an important analytical tool. The Raman bands of the target molecules can be strongly enhanced by applying excitation wavelengths which are resonant with the electronic absorptions [17-20]. NIR excitation wavelengths at 785 nm and 1064 nm are commonly employed to avoid fluorescence background. In order to have sufficient effective length for the fiber enhancement, the liquid core fiber should have low attenuation for both the wavelengths of excitation and Raman scattered light. The most commonly used Raman fingerprint region is 0 ~ 2000 cm^{-1} shifted from the excitation wavelength, which is 12.5 nm for 250 nm excitation and 264 nm for 1064 nm excitation.

2.2. Approaches based on polymer fiber

In early years, the glass capillary was the only available form of a liquid core optic fiber [7-9]. Its high RI limits strongly the choice of solvent media, fatally, the usage of water. Some polymer materials have lower refractive indices than that of water and can therefore be useful for FERS in aqueous media. Within the last two decades, these new types of fiber were characterized [15, 21-24] and applied to Raman spectroscopy [16, 24-35] and other spectroscopic techniques [36-41]. According to our research, UV-resonance Raman spectroscopy (UV-RRS) can combine with FERS for very low concentrated aqueous solutions [YAN-1, YAN-2].

The most significant limitation of polymer fibers is the poor optical quality of the material. The large inner surface roughness and the poor symmetry limit the light guiding ability of the polymer fiber. The attenuation of the polymer fiber is typically larger than 10 dB/m [YAN-1]; therefore the effective length is limited to ~2cm. Besides, the fabrication process limits polymer fibers from having small core size, and the lowest core diameter of commercially available polymer fibers is around 150 µm, which leads to unnecessary signal loss at the entrance slit of the spectrometer [YAN-1].

Other than polymer, very few solid materials have refractive indices lower than that of water. Ice [42] and patterned nanoporous material [43] have been employed to establish liquid core fibers. With direct light coupling into a water stream, guiding in water-jet can be achieved as well [44-48]. However, these approaches still struggle with the poor optical quality of the material and the strong power losses in the waveguide (>25 dB/m), as well as the instabilities in the optical setup.

2.3. Approaches based on HC-PCF

2.3.1. Introduction to HC-PCF

In conventional step-index optical fibers, light is guided by total internal reflection, which occurs only if the core has a higher refractive index than the surrounding cladding material. Photonic crystal fibers (PCF) [49, 50] consist a solid or hollow core surrounded by a microstructured air-hole cladding along the entire length of the fiber. Thus, PCFs can be divided into two types: solid core and hollow core PCFs. In this dissertation, I focus on hollow core PCF (HC-PCF) which guide light in a hollow core. Hollow core photonic crystal fibers are fabricated from a stack of arranged silica capillaries with optical fiber drawing techniques [51]. The hollow core is formed by removing seven capillaries from the stack. Typical diameters for the hollow cores range from 5 to 30 µm. A periodic microstructure at the dimension of the light wavelength shows strong reflection at specific wavelengths (bandgap effect), which is also the origin of the color in butterfly wings and anti-counterfeiting holograms [51]. Thus, trapping light in a low-refractive material surrounded by glass structures becomes possible. The light propagation in the hollow core has excellent potential for extremely low loss guidance for the light of the bandgap wavelengths, as the light travels predominantly in the air or even vacuum. However, attenuation of HC-PCF is strongly limited, as the bandgap effect is extremely sensitive to structural imperfection and variations that occur over the long fiber length [52]. For the near-IR light guidance, losses of HC-PCFs are low with attenuation at 1550 nm of 30 dB/km. With decreasing wavelength, the corresponding microstructure is smaller and therefore suffers more from the structural imperfection. Thus, the guidance of the light in the UV region has not yet been achieved in HC-PCF.

HC-PCFs can be filled in two ways: non-selective filling and selective filling. The non-selective filling is to fill the hollow core and the microstructured cladding region with the same liquid sample. Selective filling only fills the hollow core of the PCF, which needs special treatment of the fiber ends to make just the fiber core accessible to be filled by a sample. In the next sections, FERS based on both two filling methods are discussed.

2.3.2. Non-selectively filled HC-PCF

In HC-PCFs, the light is guided by the bandgap effect of the two-dimensional photonic crystal in the hollow core. This guiding mechanism is very different from that of conventional optical fibers, and light can be guided in media with low refractive indices (air or water). The bandgap of the liquid filled HC-PCF (nonselectively filled) will shift to a shorter wavelength, due to the decrease in the contrast of refractive indices [YAN-3]. The shift can be estimated according to a simple frequency-scaling law [53-55]:

$$\lambda' = \lambda_0 \sqrt{\frac{1-\left(\frac{n_{liquid}}{n_{glass}}\right)^2}{1-\left(\frac{n_{air}}{n_{glass}}\right)^2}} \tag{12}$$

where λ_0 is the original bandgap wavelength of the air-filled fiber, λ' is the wavelength of the shifted bandgap, n_{air} is the refractive index of air, n_{glass} is the refractive index of fused silica and n_{liquid} is the refractive index of the liquid filled into the fiber. Fiber enhancements of the Raman signal has been achieved in prior studies by confining the excitation laser in the fiber core with this shifted bandgap effect [53, 55-64]. Monitoring of heparin concentration in serum has been demonstrated recently with an HC-1550 fiber and a 785 nm excitation laser [58, 65]. We have pushed this concept further to the visible range and achieved Raman enhancement at 532 nm excitation wavelength [YAN-3]. In experimental conditions that the excitation wavelength is 532 nm corresponding to λ', and the liquid under examination is water (n_{liquid} = 1.33), we can find λ_0 (the wavelength of the original fiber bandgap) to be 950 nm. The laser wavelength should be at the short edge of the shifted bandgap as possible, in order to allow the entire spectral range of a Raman spectrum (532 nm ~ 676 nm, 4000 cm^{-1} Raman shift) to be guided in that bandgap. Figure 5 shows the shift of the original bandgap of the HC-PCF at 1060 nm (experimental results) [YAN-3].

The FERS setup can also be applied to enhance the gas Raman signal [66, 67]. Raman gas analysis enables the detection of homonuclear diatomic gases (N_2, O_2, and H_2) and their isotopes, which are very difficult to be monitored simultaneously with other established techniques [YAN-4]. As the refractive index is not changed in the fiber core, there is no bandgap shift in HC-PCF. When monochromatic laser light is guided through a gas sample, the photons can interact with a larger number of gas molecules, and therefore the Raman signal is enhanced [YAN-4]. With the remarkable fiber enhancement, HC-PCFs have been employed in detections of low-concentrated volatiles for clinical [66], environmental [68], and industrial studies [68].

2.3.3. Selectively filled HC-PCF

The bandwidth of the bandgap in HC-PCF depends strongly on the dielectric contrast in the microstructure [69]. With the liquid filling of the air holes in HC-PCF, the dielectric contrast decreases and the spectral width narrows down [69]. This effect limits the selection of the excitation laser wavelength and narrows the accessible spectral range for the Raman signal. In order to overcome the drawback of the limited bandgap in non-selectively filled HC-PCFs, the liquid sample can be filled into the central hollow core of the HC-PCF selectively, and the step-index guidance, which allows guiding in a broad spectral range, can be achieved in the liquid core [YAN-6].

The air cladding with an extremely low effective refractive index is needed to achieve step-index guiding in the water-filled core, as water has a low refractive index of 1.33. To form step-index guidance in aqueous samples, the effective refractive index of the cladding should at least be lower than that of aqueous solutions (n=1.33). The effective refractive index of a microstructure can be calculated numerically according to the wavelength (λ), the fiber pitch size (Λ), and the air-filling fraction (*R*) of the microstructure [70]. As a proof of principle, fiber enhancement of fluorescence spectroscopy has been demonstrated in the HC-PCF selectively filled with ethylene glycol (n=1.43) [71]. Selectively filled fibers HC19-1550 [72], HC800 [73], and HC1060 [73] were discussed for Raman enhancement of aqueous samples. A similar approach enhancing fluorescence spectra of aqueous samples with a NIR-guiding HC-PCF was also addressed [74]. However, these types of HC-PCFs cannot provide a refractive index lower than that of water in the visible spectral range [YAN-6]. Some studies combined SERS and HC-PCFs with visible laser excitation, but the enhancement was mainly achieved by SERS and not by waveguiding [64, 72, 75]. According to the simulation, the HC-440 fiber has an air-clad with an effective RI of 1.25. This type of HC-PCF was thoroughly studied [YAN-6], which is explained in chapter 4.3.

In order to achieve selective filling, the process of using a fiber splicer to collapse the microstructure of the HC-PCF was explored and applied in prior studies [71, 72, 74, 76-80]. Various techniques such as splicing HC-PCF to a single mode fiber [81], micro-drilling [82], glue filling [83], and MEMS-based sealing ring [84] were demonstrated in other prior studies. Air-clad collapsing is so far the most promising method for HC-PCFs, as the processed fiber ends consist only of fused silica from fiber itself [YAN-6]. However, the secondary effect is a “bottleneck” at the fiber end, which strongly affects the quality of optical coupling. In our latest work, we developed a novel two-step collapsing technique that maintains excellent optical guidance properties [YAN-6]. The length of the manufactured bottleneck reduced tremendously from 200 µm [71] to 20 µm [YAN-6].

2.3.4. Analysis of HC-PCF based on Raman imaging

In fiber-enhanced Raman spectroscopy (FERS) based on HC-PCFs that with small core size, laser intensity leaks from the liquid core into fiber cladding region inevitably, and therefore raises the undesired background from the fused silica [85]. These strong silica signals can increase the shot noise of the collected Raman spectra, or even saturate the CCD detector. This deteriorates the sensitivity of FERS, especially in the low wavenumber region (<800 cm^{-1}) for weak Raman peaks. To suppress the background, the Raman signal from the hollow core must be separated from the silica signal from the cladding region. This separation can be achieved by employing a spatial filtering system based on their different spatial distribution [85]. In the prior work, the outcome of the spatial filtering with various pinhole sizes was examined, and the optimal pinhole size was determined [85].

Raman imaging technique brings an opportunity for deeper understanding of fiber-enhanced Raman sensing in HC-PCFs [YAN-5]. The spatial distributions of the Raman peaks of interest and the unwanted background are important parameters for building proper spatial filtering system. The leakage of the laser intensity can also be investigated with the Raman imaging technique, in order to reveal the potential for further improvements.

The most common method to obtain the spatial distribution of Raman signal is the point-by-point scanning of the sample. The system measures an array of spots by moving the stage after each measurement. The total time elapses of the scanning procedure consist of the total exposure time of the measurements. The sample might change over time or affected by the movement of the stage, and therefore distort the acquired Raman image. Multi-channel Raman imaging based on fiber array is a robust tool for analysis of Raman signal distribution at fiber ends [YAN-5]. Spatially resolved Raman images can be obtained in one exposure without moving the sample [YAN-5]. The effect of spatial filtering can be evaluated with the help of the Raman image, and the optimal size of the spatial filter can be selected to balance the suppression of the background and the decrease of the Raman signal in the setup [YAN-5].

3. Experimental setup and data analysis

In a fiber-enhanced Raman sensing system, the laser light is coupled into the liquid-filled optical fiber, and the Raman scattered light is confined in the fiber core and directed towards a spectrometer. The hollow core optical fiber is used to extend the path-length of the laser light, and also as a miniaturized sample container for the liquid sample. In order to achieve a stable optical coupling of the laser to the liquid core fiber for quantitative and reproducible Raman detection, a fiber adapter was also developed in [YAN1, YAN-2] (Figure 1). The custom-made fiber adapter provides an optical window for coupling the laser light into the fiber and two side-ports for filling analyte and convenient cleaning procedure [YAN1, YAN-2]. To avoid photo-degradation, the samples are kept flowing in the liquid core fiber at a small flow rate with the help of a pump. The assembly has minimized dead volume, and all tubing consists of polymer material with excellent mechanical and chemical resistance. Therefore, the samples passed through the strong laser focus within a short time and are not damaged by the laser radiation.

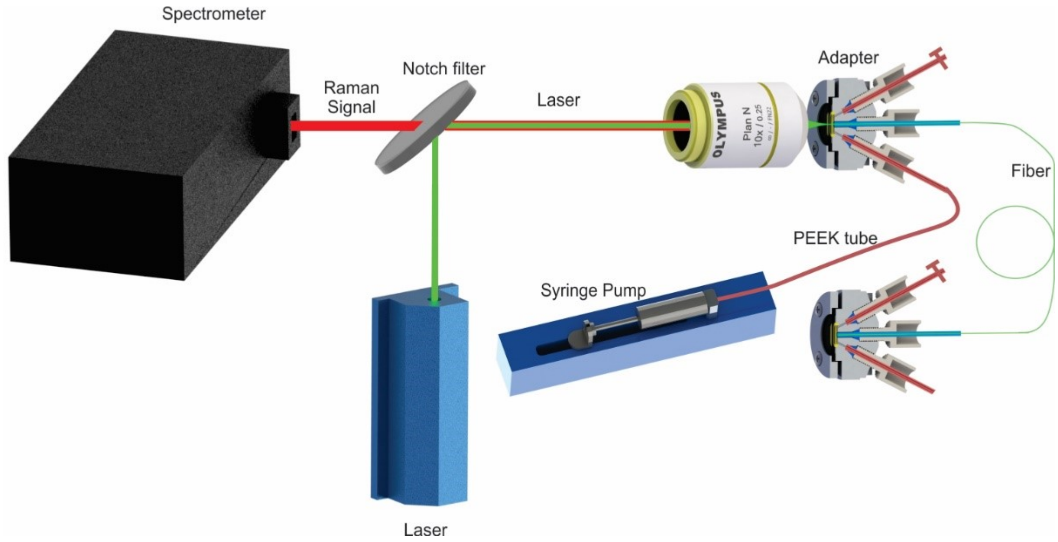

Figure 1: *Schematic view of a typical experimental setup for FERS [YAN-2]. Reproduced from [YAN-2] with permission from the Royal Society of Chemistry. Copyright 2016 Royal Society of Chemistry. The laser light is focused into the fibers with an objective lens, and the backscattered Raman signal is collected by the same objective lens, passes through the notch filter, is dispersed in the spectrometer, and detected with the help of a CCD detector. A syringe pump keeps the liquid media flowing through the fiber, such that the analyte passes through the laser focus within a very short time and no photodegradation occurs.*

In fiber-enhanced Raman sensing, imprecise light coupling and guiding attenuations in the filled fiber can lead to unwanted background signals. These signals are contributed by the Raman scattering and fluorescence of the cladding and/or coating material of the optical fiber. Furthermore, coupling errors also cause leakage of the laser power from the liquid core to the exterior layers and therefore decrease the Raman intensity of the liquid sample. Especially in a FERS setup that employs an HC-PCF, the alignment of the laser coupling is difficult and time-consuming, due to the small mode field in the hollow core of the photonic crystal fiber. The mode field diameter of the photonic crystal fiber HC-440 is only around 4 µm, and even small coupling errors can lead to a great drop of the sensitivity. An automatic alignment system has been developed to achieve an easy-to-use FERS system with stable performance [YAN-5]. The working principle of this system is briefly summarized in chapter 4.5.

As the Raman signal of the analyte is all confined in the fiber core and the silica Raman signal distribute mainly on the surrounding microstructure, the spatial filter is a useful tool for background reduction and SNR improvement. In fiber enhancement with HC-PCF, pinholes of various diameters can be inserted in the focal plane in order to eliminate the silica signal. A pinhole with a suitable size, which fits the diameter of the mode field in the fiber core, can improve the SNR of the Raman signal prominently [YAN-5].

The Raman spectra of low-concentrated analytes contained a spectral background from the solvent. In order to achieve precise and reproducible quantification of the analyte, all acquired Raman spectra were normalized to the water Raman band at 1645 cm^{-1} or the Raman band of the buffer solution. The quantity of the solvent in each measurement could be assumed as constant. Thus, the Raman peak of the solvent was employed as an internal standard [86] to cancel out all systematic variations and fluctuations (laser intensity, optical coupling efficiency, effective fiber length, etc.), and therefore improve the quantitative detection ability. When calculating the signal-to-noise ratio (SNR) values, the signal and the noise were defined as the peak height of the Lorentzian fit and the root-mean-square (RMS) values of the baseline, respectively. The limit-of-detection (LoD) concentrations were derived when the SNR was equal to three.

4. Results and discussion

4.1. Fiber-enhanced UV-Raman sensing of drugs [YAN-1]

Malaria is a serious and sometimes fatal disease widespread in the tropical and subtropical regions. The complexity of the malaria parasite makes the development of malaria vaccines very difficult. Currently, there is no commercially available malaria vaccine, and malaria control is still heavily dependent upon the use of the antimalarial drugs. Malaria resistance evolves even to the newest cures [87-89], and there is a continuing need for the development of new effective drugs. For the design of new structure-based drugs, a better understanding of the mechanism of action of the drugs on a molecular level is essential [18, 90]. Resonance Raman spectroscopy is a competent technique and selectively enhances the Raman signals of biomolecules even in complex biological environments [18]. Specific vibrational modes are enhanced when the electrons in the molecule are excited to a higher energy level by the laser [91-96].

The developed FERS setup utilizes a polymer fiber as the analyte container and the light guide [YAN-2]. In resonance Raman spectroscopy, reabsorption of the liquid in the fiber varies with the concentration of the analyte. Therefore, the fiber enhancement factor is not constant for samples in various concentrations. To remove the difference of the signal intensities caused by the various effective lengths, the spectrum of the solvent was taken as an internal reference. The normalization canceled the variation caused by the difference of the enhancement factors of the fiber and improved the quantitative detection ability.

The Raman spectra of mefloquine (MQ) aqueous solutions were measured by fiber-enhanced Raman detection and conventional Raman detection. An excitation wavelength of 532nm was employed to explore the fiber enhancement separated from UV and resonance Raman enhancement. The MQ Raman peaks at 1365 cm^{-1} were detected in the 1 mM mefloquine solution. That is the most active peak of mefloquine, referring to very strong ν(C=C)-stretching and ring breathing vibrations in the quinolone ring [93]. The Raman signal of chloroquine (CQ) at 1557 cm^{-1}, which is referring to strong ν(C=C) and ν(C-C) stretching and breathing vibrations in the quinolone ring of CQ, showed a similar enhancing effect in fiber detection. The intensities of mefloquine's 1365 cm^{-1} peak and chloroquine's 1557 cm^{-1} peak in conventional measurements and fiber detections were contrasted with different concentrations. As a result, the fiber detection has a sensitivity enhancement factor of 14.2 in fiber detection compared to the conventional detection in bulk volume measurement (Figure 2).

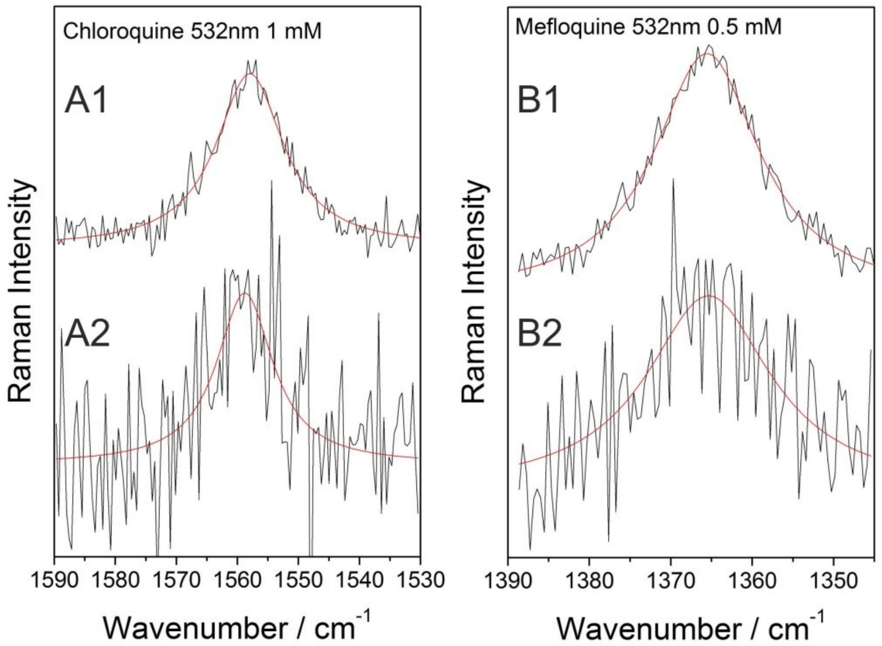

Figure 2: *Comparison of conventional (A2, B2) and fiber-enhanced (A1, B1) non-resonance Raman spectra of chloroquine and mefloquine respectively. Reproduced from [YAN-1] with permission from the American Chemical Society. Copyright 2013 American Chemical Society.*

Two deep UV excitation wavelengths, 244 nm and 257 nm, were employed to explore UV-resonance Raman spectroscopy in liquid core fiber. Strong, selective enhancements of the Raman bands of MQ and CQ were observed, which were not easy to detect in non-resonance Raman spectroscopic, with a good agreement with their peak assignment [92, 93]. There was a particularly strong enhancement of the molecular vibration at 1636 cm^{-1} of CQ for $\lambda_{exc.}$= 244 nm excitation [YAN-1]. The Raman peaks of CQ and MQ in the 1500 cm^{-1} to 1650 cm^{-1} Raman shift region were strongly enhanced for the applied UV excitation wavelengths [YAN-1]. This region can be assigned to ν(C=C) stretching vibrations in the quinolone part of the drug molecules [92]. Vibrational spectroscopy of characteristic molecular groups will provide useful information to study how these vibrational modes are influenced in future drug-target-interaction experiments [92]. The enhancement obtained from the fiber in UV-resonance Raman was not as good as it was in non-resonance Raman sensing, as the light-absorbing solution attenuated the UV laser and shortened the effective length strongly. Therefore, Raman signals of high-concentrated absorbing solutions (>0.1 mM) were not enhanced by the fiber. The fiber-enhanced sensing shows better performance than the conventional sensing in the low concentration range (<0.1 mM).

The sensitivity for mefloquine of the polymer fiber detection was 5 and 8.2 times higher compared with that of the conventional detection in 244 nm and 257 nm excitation respectively [YAN-1]. The lowest mefloquine concentration that can be detected by fiber-enhanced UV-RRS were 5 µM (244 nm) and 2.5 µM (257 nm), and the LoDs were 25 µM (244 nm) and 10 µM (257 nm) in conventional sensing [YAN-1]. The LoD of mefloquine in the non-resonance conventional detection was 0.5 mM, hundreds of times higher than what the UV-resonance fiber can detect. The lowest chloroquine concentrations that can be detected with the polymer fiber were 0.5 µM and 0.75 µM at 244 nm and 257 nm respectively. The concentrations can be detected in conventional detection were 2.5 µM (244 nm) and 5 µM (257 nm) [YAN-1].

The minimum absolute quantities of pharmaceuticals were calculated from the lowest detectable concentration and the sample volume. For mefloquine, the minimum absolute quantity was 9.5×10^{-11} mol at $\lambda_{exc.}$= 257 nm [YAN-1]. The minimum quantity of chloroquine to reach the LoD at $\lambda_{exc.}$= 244 nm was 1.9×10^{-11} mol [YAN-1].

In order to exploit further improvements of FERS based on UV and electronic resonant excitation, fiber attenuations and self-absorption effects were studied. Self-absorption is the absorbing of the Raman scattered light take places at the analytes chloroquine and mefloquine itself. Strong optical attenuation will be caused by the high-concentrated absorbing analytes, and therefore the path length of the light in the fiber will be shortened. According to the equations 8 and 9 in the previous chapter, the Raman intensity can be expressed as follows:

$$I_R = A' \cdot I_0 \cdot \sigma(\tilde{\upsilon}) \cdot L_{eff} \cdot c \qquad (13)$$

The coefficient A' describes the overall performance of the system such as the quality of the optical coupling. This coefficient is expected to be constant in a series of measurements. I_0 is the laser intensity, $\sigma(\tilde{\upsilon})$ is the Raman scattering cross-section, and c is the concentration of the analyte.

There is also a thin layer of light-absorbing solution present under the optical window. This layer (thickness $L_d = 1\ mm$) does not contribute to the Raman signal, but will still diminish the laser and Raman scattered light in case of high concentrations of absorbing analytes. Therefore L_{eff} can be modified to L'_{eff}:

$$L'_{eff} = T_{dl} \cdot T_{dr} \cdot \int_0^{L_p} T_l(z) \cdot T_r(z)\, dz = e^{-(\varepsilon_l \cdot c \cdot L_d)} \cdot e^{-(\varepsilon_r \cdot c \cdot L_d)} \cdot \frac{1 - e^{-(\mu_{sl} + \mu_{sr} + \varepsilon_l \cdot c + \varepsilon_r \cdot c) \cdot L_p}}{\mu_{sl} + \mu_{sr} + \varepsilon_l \cdot c + \varepsilon_r \cdot c} \qquad (14)$$

where L_d is the thickness of the dead volume and T_{dl} and T_{dr} are the transmissions of the laser and the Raman wavelengths through the layer of dead volume. Here μ_{sl} and μ_{sr} are the effective fiber loss coefficients at the laser and the Raman wavelengths respectively, while ε_l and ε_r represent the analyte extinction coefficients at the wavelengths of the laser and the Raman scattered radiation. Thus the effective length can be expressed as [YAN-1]:

$$I_R(\tilde{\upsilon}, c) = \mathbf{A} \cdot L_{eff} \cdot c = \mathbf{A} \cdot e^{-(\mathbf{B} \cdot c \cdot L_d)} \cdot \frac{1 - e^{-(\mathbf{C} + \mathbf{B}c) \cdot L_p}}{\mathbf{C} + \mathbf{B}c} \cdot c \qquad (15)$$

$$\mathbf{A} = A' \cdot I_0 \cdot \sigma(\tilde{v});\ \mathbf{B} = \varepsilon_l + \varepsilon_r;\ \mathbf{C} = \mu_{sl} + \mu_{sr};$$

Factor A describes the overall performance of the FERS system. The intensity of the excitation laser, the quality of the optical coupling, and the Raman scattering cross-section of the analyte are included. Factor B represents the extinction coefficients. Factor C describes the loss caused by the fiber. As explained in chapter 2, light-absorbing samples (large factor B) shortens the effective length of the fiber and therefore decrease the sensitivity of FERS. It is necessary to find a balance between the attenuation due to self-absorption and the UV resonance Raman enhancement in sensing of ultra-low-concentrated analytes. According to the equation, liquid core optical fiber can still provide long effective length for ultrasensitive detection in the low concentrated absorbing analyte, as factor B appears together with the concentration of the analyte. The development of the optical fiber can result in a smaller factor C, leading to an even longer effective length of the liquid core fiber. Unfortunately, the guiding ability of the polymer fiber is relatively poor, regarding strong attenuation due to the rough inner surface. Thorough simulation of the sensitivities with various improved parameters has been demonstrated in the published work [YAN-1].

In this work, the UV-resonance Raman measurement was at the first time enhanced by the liquid core fiber, and the detectability was improved in comparison to the conventional UV-resonance Raman spectroscopy. The calculations based on the effective length also reveal the potential of fiber-enhanced Raman spectroscopy in further developments as an ultrasensitive chemical sensing technique for a wide range of biomolecules.

4.2. UV-FERS monitoring of bile pigments [YAN-2]

Heme chromophores are iron protoporphyrin IX complexes and fulfill essential roles in several regulating processes in biological systems [98]. The heme group is converted to biliverdin (BV) and bilirubin (BR) in enzyme-catalyzed reactions and subsequently eliminated via bile after biotransformation (conjugation) in the liver [98]. Hyperbilirubinemia is a condition in which bilirubin concentration is above the normal range. It causes a yellowing of the patient’s skin, sclera, and other tissues [99]. The toxicity of bilirubin is especially critical in neonatal hyperbilirubinemia due to incomplete formation of the blood-brain barrier [100]. The increased unconjugated bilirubin in the circulating system may enter the central nervous system and thereby leads to irreversible neurological damage such as athetoid cerebral palsy, hearing loss, vision problems, or mental retardation [101]. Normal biliverdin concentrations in serum are reported as 0.9 ~ 6.5 µM and correlate with bilirubin concentration strongly [102]. Thus, a detection technique that quantifies small changes in bilirubin and biliverdin concentrations simultaneously would be greatly helpful for the diagnosis. Fiber-enhanced Raman spectroscopy (FERS) has great potential as a tool for sensitive and selective analysis of the biomolecules. FERS can also be minimally invasive in clinical applications, as it requires only minimal sample volumes for quantification. In the published work, fiber-enhanced Raman spectra of hematin, hemoglobin, and whole erythrocytes were demonstrated and compared to the conventional Raman spectroscopy [YAN-2].

To benchmark the effect of fiber-enhanced Raman separately, the excitation wavelength λ = 532 nm was applied to avoid electronic transitions of the molecules. The characteristic Raman peak of hematin at 1626 cm^{-1}, which is assigned to the vibrational mode ν_{10} [103, 104], was detected with identical experimental parameters in a series of concentrations in fiber-enhanced Raman sensing and conventional cuvette measurements. The intensities of the Raman peaks and the root-mean-square values were analyzed for quantification of the limit-of-detection (LoD, 3x root-mean-square noise).

The LoDs of hematin were determined as 36 µM and 3.6 µM for conventional and fiber enhanced Raman sensing respectively [YAN-2].

The excitation wavelength λ = 413 nm was applied to exploit fiber-enhanced resonance Raman sensing of hematin, as it matches the strong electronic absorption band. The Raman peak at 1373 cm^{-1}, which can be assigned to the totally symmetric mode ν_4 [104-106], was intensely enhanced by the resonance Raman effect. As a result, a significantly improved LoD of only 0.1 µM was achieved with fiber-enhanced resonance Raman spectroscopy [YAN-2]. The spectra of hematin showed an excellent linearity between the Raman peak and the analyte concentration. Therefore, quantification of the analyte can be achieved with simple linear calibration, and the linear fit can be utilized to quantify the actual hematin concentration.

Hemoglobin was analyzed with the same experimental setup. The hemoglobin band at 1373 cm^{-1}, which was assigned to mode ν_4 of the heme group [107], was also significantly enhanced in FERS [YAN-2]. This Raman peak is also an important marker band for monitoring the oxygenation and deoxygenation of hemoglobin in red blood cells [107, 108], which provides additional information of the blood sample and supports a differential diagnosis. The LoDs of hemoglobin were improved from 10.7 µM for non-resonance Raman measurements with λ = 532 nm excitation down to 0.25 µM in fiber-enhanced resonance Raman sensing. Furthermore, an excellent linearity was achieved for quantification of hemoglobin [YAN-2].

To explore the potential of FERS for investigating complex biological samples, fiber enhanced Raman spectra of oxygenated intact erythrocytes were also acquired and analyzed. The strongest Raman peak at 1376 cm^{-1} in the resonance Raman spectra of the erythrocytes (λ = 413 nm) corresponds to the vibrational mode ν_4 in hemoglobin (Figure 3). Fiber-enhanced resonance Raman spectroscopy showed the promising capability of avoiding photodegradation with delicate intact erythrocytes [YAN-2]. This brings FERS great potential for medical diagnosis of diseases, for example, different types of anemia and hemolytic disorders.

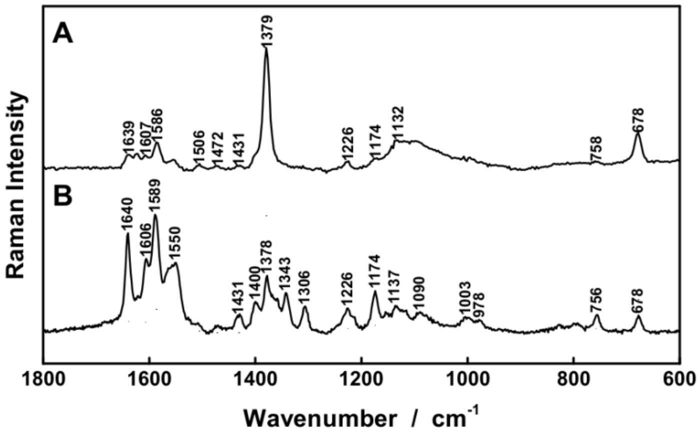

Figure 3: *Fiber-enhanced Raman spectra of whole erythrocytes. Reproduced from [YAN-2] with permission from the Royal Society of Chemistry. Copyright 2016 Royal Society of Chemistry. Intact red blood cells (1:199 diluted in 1x PBS) were gently guided through the hollow fiber and Raman spectra were taken with* $\lambda_{exc.}$ *= 413 nm (A) and* $\lambda_{exc.}$ *= 532 nm (B).*

According to the experimental results, biliverdin and bilirubin have extremely strong fluorescence with visible excitation lasers [YAN-2]. Therefore, Raman sensing of biliverdin and bilirubin is very challenging. The fluorescence signal was found to be weak with 364 nm excitation wavelength. The Raman spectra were enhanced, and sub-µM detection for biliverdin and bilirubin were achieved with good linearity [YAN-2]. A two-component solution, consisting of 1 µM biliverdin and 50 µM bilirubin was analyzed [YAN-2] as a simulation to the typical concentration of patients presenting hyperbilirubinemia [109]. Similarly, a two-component solution of 25 µM bilirubin and 75 µM biliverdin was utilized as a simulation to the typical concentration of patients with hyperbiliverdinemia [YAN-2]. The Raman spectra of biliverdin and bilirubin are very similar due to the similarity in their molecular structure. Bilirubin shows a Raman peak at 1272 cm^{-1}, which can be assigned to a combination of CC- stretching vibration in one pyrrole unit as well as CH-, CH_3-, and OH- wagging and scissoring vibrations (Figure 4A) [YAN-2]. The Raman band of biliverdin at 1282 cm^{-1} can be assigned to a combined vibration consists of strong CC-, and CN-stretching vibrations in several pyrrole units as well as CH-, CH_2-, and OH- wagging and scissoring vibrations (Figure 4B) [YAN-2]. By employing a least-square deconvolution method of the Raman spectrum, the peak heights of the 1272 cm^{-1} and 1282 cm^{-1} bands were computed to 0.96 ± 0.20 µM for biliverdin and 56 ± 8.0 µM for bilirubin [YAN-2]. For the mixture solution of 25 µM bilirubin and 75 µM biliverdin (hyperbiliverdinemia), also $\lambda_{exc.}$ = 752 nm (non-resonance FERS) can be applied to analyze a two-component solution [YAN-2]. The Raman peaks at 1253 cm^{-1} (bilirubin) and 1243 cm^{-1} (biliverdin) were identified as suitable marker bands to distinguish both bile pigments simultaneously. The molecular vibration of bilirubin at 1253 cm^{-1} is assigned to C-H-, N-H- and O-H bending vibrations (Figure 4C) [YAN-2]. The Raman band of biliverdin at 1243 cm^{-1} also comes from C-H, N-H, and O-H- bending vibrations (Figure 4D) [YAN-2]. The concentrations were calculated to be 24.1 ± 1.8 µM for bilirubin and 77.2 ± 5.0 µM for biliverdin respectively [YAN-2].

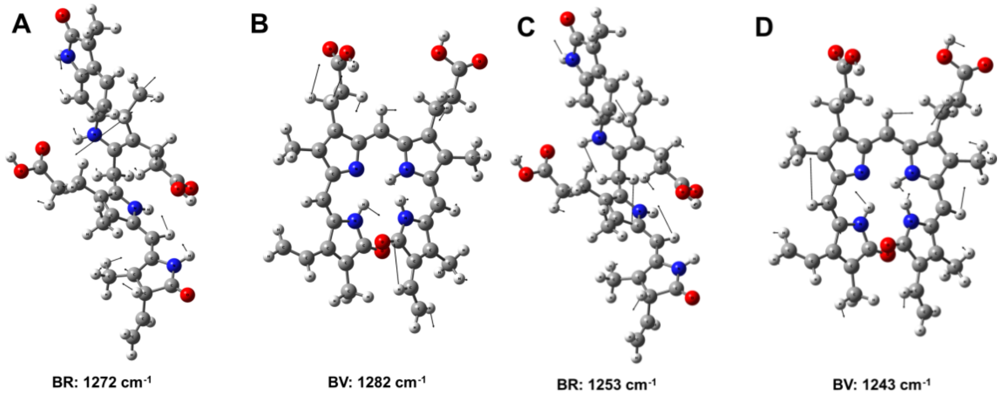

Figure 4: *Vibrational modes of biliverdin (BV) and bilirubin (BR) that were used for quantification. Reproduced from [YAN-2] with permission from the Royal Society of Chemistry. Copyright 2016 Royal Society of Chemistry.*

4.3. FERS of antibiotics in HC-PCF [YAN-3]

Early administration of appropriate antibiotic therapy is the cornerstone of the sepsis treatment [110]. In clinical studies, plasma levels of antibiotics show large interindividual variations in patients with severe sepsis and septic shock due to the changes in various pharmacokinetic parameters [111]. The pharmacokinetic parameters can change quickly within hours and result in increased treatment failure or drug toxicity [112]. The approved doses recommendations are found to be incorrect for some critically ill patients with severe infections, as they are derived from the studies in healthy volunteers or patients with moderate infections [113]. For some anti-infectives, for example, vancomycin, aminoglycosides, and voriconazole, dose adjustment based on therapeutic drug monitoring have already successfully improved the outcome of the treatment [113-115]. The current method for the quantification of antibiotics is based on high-performance liquid chromatography (HPLC) [116-118]. However, chromatography-based methods are time-consuming and labor-intensive as they require complex sample treatment procedures. Therefore, fast-response or point-of-care diagnostics of antibiotics level are not yet available in the clinic. Thus, an easy-to-use, fast, and highly selective detection technique is needed for individualized quantification of antibiotics concentrations.

As mentioned in the previous chapter, microstructured optical fibers are superior regarding optical quality. Hollow core photonic crystal fibers (HC-PCF) [52, 119-122] have drawn much attention in various research fields, including FERS. In hollow core photonic crystal fibers, the laser excitation wavelengths must be matched to the bandgap wavelength of the liquid filled fiber. The bandgap can be shifted to lower wavelengths by filling the microstructure completely with liquid media [53, 55]. In this work, we demonstrate the improved FERS based on HC-PCFs which support visible laser excitation for the first time [YAN-3]. According to the calculation (equation 12), an HC-PCF with an original bandgap at 1060 nm was employed. However, the equation can only predict the center of the transmission band [YAN-3]. The precise position of the starting and the end of the transmission band can only be determined experimentally. The center of the shifted transmission spectrum of the water-filled fiber is predicted at 593 nm according to the equation. The experimental results (Figure 5) show that the transmission band ranges from 510 nm to 680 nm, which has a good agreement to the prediction [YAN-3]. Thus, a laser excitation wavelength of λ = 532nm was employed, and the liquid core optical fiber provides excellent transmission for a Raman spectral range of up to 4000 cm^{-1}.

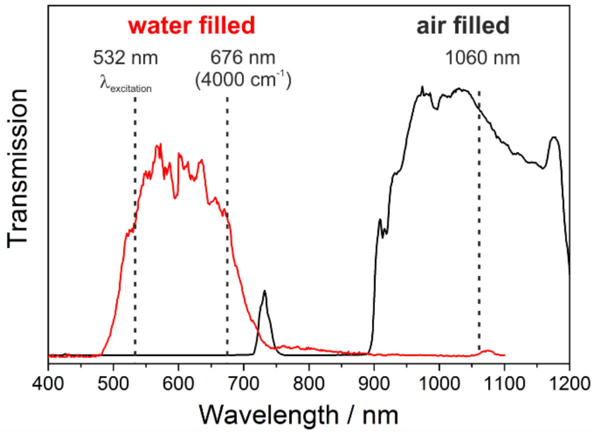

Figure 5: *The bandgap of HC-PCF shifts to short wavelength with non-selectively filling. The sensor fiber provides a low loss optical guidance for an excitation with the laser wavelength of λ= 532 nm and a Raman spectrum up to 4000 cm^{-1} (corresponds to 676 nm). Reproduced from [YAN-3] with permission from the Royal Society of Chemistry. Copyright 2018 Royal Society of Chemistry.*

The enhancement factor of FERS relies strongly on high-quality laser confinement in the liquid core [YAN-3]. In HC-PCF, the size of the central hollow core is small (<10 µm), and the laser confinement is easily affected by the mismatch of the focus and the fiber core [YAN-3].

An automatic fiber coupling has been developed, which is proved to be very useful in FERS with HC-PCF [YAN-3, YAN-5]. In order to demonstrate the influence of the coupling error, the system was set to coupling positions with offsets [YAN-3]. The results show that the Raman performance drops by 10% with a small error in the lateral coupling position of only ± 1.5 µm (Figure 6). Offsets in optical coupling also raise the background Raman bands of the silica fiber material and therefore cause an increased noise level. In order to keep a good performance (>90%) and reasonable low background, the precision requirement of the lateral position is ± 1.5 µm. In the laboratory, stable performance of optical coupling is easily achieved. This requirement should also be considered in the design of a portable miniaturized setup for clinical application.

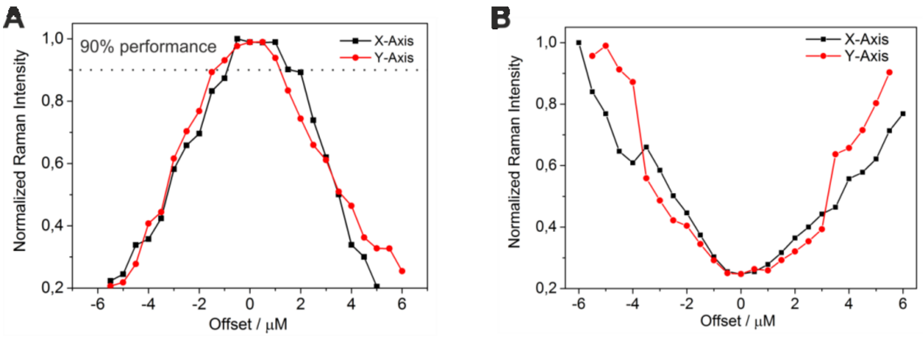

***Figure 6:** Analysis of the coupling position of the sensor fiber. Reproduced from [YAN-3] with permission from the Royal Society of Chemistry. Copyright 2018 Royal Society of Chemistry. **A**: The height of the Raman peak of ethanol at 880 cm^{-1} was measured with lateral offsets relative to the optimized coupling position. The analysis shows that the Raman signals maintains 90% peak intensity within a ±1.5 µm of lateral offset and strongly decreases for higher lateral misalignments. **B**: The background Raman signal of the fiber silica material (normalized Raman peak intensity at 490 cm^{-1}) increases for a misalignment of the lateral coupling position and thus causes a rise of the noise level.*

According to the research, the levofloxacin concentration in plasma reaches 27 µM after the administration (500mg, intravenous) [123]. The strongest characteristic Raman peak of levofloxacin at 1619 cm^{-1} (Figure 7) was employed to quantify the concentration [YAN-3]. This Raman band can be assigned to strong combined νC=C stretching vibrations of the aromatic ring structure [YAN-3]. The Raman peak at 1398 cm^{-1}, which is assigned to the νC-C breathing vibration of the quinolone ring system, was also employed as a supplementary for identification of levofloxacin [YAN-3].

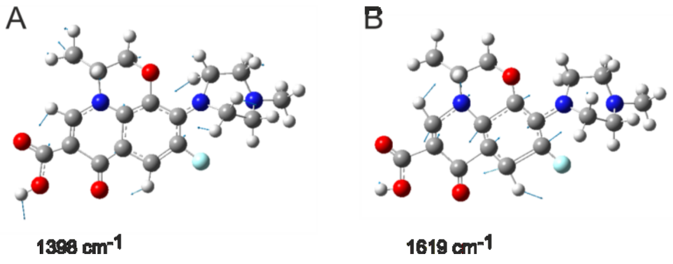

***Figure 7:** Assignment of the vibrational modes of levofloxacin that were used as Raman marker bands for quantification. Reproduced from [YAN-3] with permission from the Royal Society of Chemistry. Copyright 2018 Royal Society of*

Chemistry. The atomic displacements of the associated vibrational modes are given for the Raman peaks at 1398 cm^{-1} (A) and 1619 cm^{-1} (B).

Aqueous solutions of levofloxacin were measured with FERS in various concentrations. The sensitivity was improved strongly by the HC-PCF, and the LoD (limit-of-detection) of levofloxacin was found to be 20 µM [YAN-3]. The characteristic peaks in the levofloxacin FERS measurements show much higher SNR than that of the conventional cuvette measurements (Figure 8A). The excellent linearity of the peak heights to the analyte concentrations enabled robust calibration function for the quantification of levofloxacin (Figure 8B). The results show that fiber-enhanced Raman spectroscopy has great potential for ultrasensitive monitoring of levofloxacin levels rapidly, minimally invasive, and individually for every intensive care patient, without cross-sensitivity to other antibiotics.

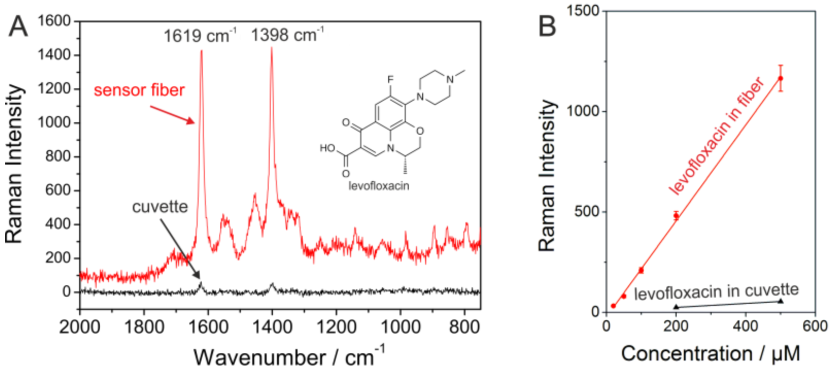

Figure 8: *Comparison of conventional and fiber-enhanced Raman measurements of levofloxacin. Reproduced from [YAN-3] with permission from the Royal Society of Chemistry. Copyright 2018 Royal Society of Chemistry.* ***A:*** *The peaks in the fiber-enhanced Raman spectrum (red) show higher intensities compared to the conventional spectrum (black) of a solution of levofloxacin with the concentration of 0.5 mM.* ***B:*** *The Raman peak intensities of levofloxacin show excellent linearity to the analyte concentration.*

4.4. FERS of biogenic gases in HC-PCF [YAN-4]

Fiber-enhanced Raman spectroscopic (FERS) analysis of gases allows quantification of multiple gases with just one single measurement [YAN-4]. Raman gas sensing has the unique ability for simultaneous identification of all gases and volatiles (except noble gases) in a broad range of concentrations [124-127]. Hollow-core photonic crystal fibers (HC-PCF) can guide the light with low attenuation within a spectral bandgap and achieve sensitive gas analysis [128, 129]. The Raman enhancement of gaseous samples can be obtained with a similar FERS setup as described in chapter 3.3. Furthermore, as gases are compressible, the tight fiber filling setup also allows us to compress the gas to high pressure, and therefore a larger number of molecules are in the fiber core, leading to a stronger Raman signal. Raman intensities of gas samples are proportional to the pressure.

Mixtures of the climate-relevant gases CH_4, CO_2, N_2O, N_2, and O_2 important biogenic gases were analyzed in order to demonstrate the performance of the new FERS-setup [YAN-4]. FERS measurement of the gas mixtures with defined concentrations show high specificity and sensitivity, and all five gases showed enhanced Raman peaks separated from each other [YAN-4]. By measuring individual gas samples with known concentrations at a defined pressure, temperature, laser power, and fiber length, a calibration of the setup was performed for reliable and reproducible fiber-enhanced Raman gas sensing [YAN-4].

As a demonstration of the capabilities of FERS for gas sensing, the gas sample consists of natural N_2 and CO_2 including all their natural isotopes was measured. The low-concentrated components $^{14}N^{15}N$ and $^{13}CO_2$ can be quantified simultaneously within one single measurement the high-concentrated N_2 and CO_2 and the dynamic range covers four orders of magnitude. The isotope $^{13}C^{16}O_2$ and $^{14}N^{15}N$ were quantified to (1.08 ± 0.03) % and (0.80 ± 0.05) % respectively [YAN-4], which were very close to the reference values of 1.09% and 0.737% [130].

4.5. Analysis of FERS in HC-PCF based on Raman imaging [YAN-5]

In this study, a novel Raman imaging setup was developed, and the performance of FERS gas sensing was analyzed with the Raman imaging setup [YAN-5]. Utilizing chemical imaging, the spatial distribution of the fiber-enhanced Raman signals and silica signals at the fiber end-face can be evaluated [YAN-5].

Multi-channel Raman imaging system can obtain Raman spectra with a bundle of fibers simultaneously without moving any part [131-133]. The fiber array collected the Raman scattering in the image plane; therefore the acquired Raman spectra were spatially resolved by the channels [YAN-5]. The optical fibers at the distal end were linearly aligned at the spectrometer. Therefore, the spectral information obtained from the channels were arranged along the vertical axis of the CCD detector. By dividing the CCD readout into multiple ROIs (region-of-interest), Raman intensities in cooperation with spatial distributions at the image plane can be reconstructed.

The region-of-interest (ROI) on the CCD (Figure 9, inset) for each fiber was recognized by plotting the total counts of each horizontal CCD lines (Figure 9, black), where the peaks were signal from the fibers and the valleys were the space in between two optical fibers. As the optical attenuation of the fibers in the bundle were different from each other. In order to obtain reliable and quantitative spatial distribution of the Raman signals, a calibration of the system was performed with a measurement of the homogenous light source and the variation of the attenuation can be corrected (Figure 9, red dash line). The full width of each ROI was set to 11 lines to obtain sufficient Raman signal and minimized cross-talk (0.4%) [YAN-5]. The calibrated system recreated the image of the homogenous light source with excellent flatness of ±1.3% peak-to-peak [YAN-5].

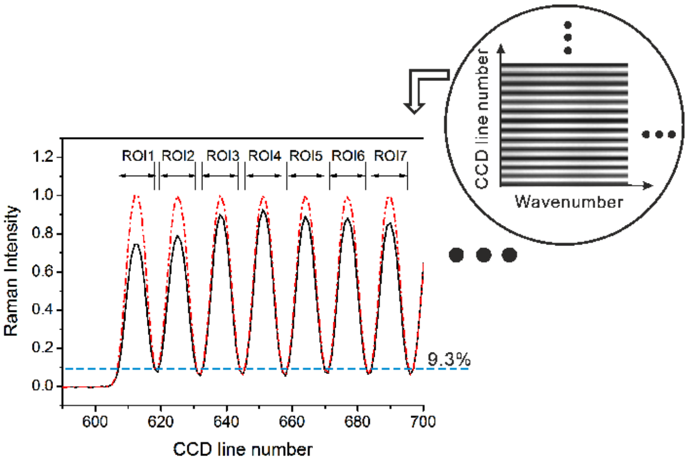

Figure 9: *Calibration of the Raman imaging system. Reproduced from [YAN-5] with permission from the American Chemical Society. Copyright 2017 American Chemical Society. The region-of-interest of each Raman spectrum was recognized and uses the peak positions as the centers of the ROIs. The plot of the total counts of each horizontal CCD lines shows a multi-peak pattern (black solid-line, only the first 7 peaks are displayed in this figure). The Raman signal in all ROIs is normalized to the same intensity in order to obtain data points with correct intensity distribution (red dash-line). The CCD counts in the valleys are 9.3% of the counts at the peaks in average (blue dash-line), indicating very little cross-talk from one fiber to another. Inset: the CCD image records Raman spectra of all fibers in a single frame with vertical offsets.*

The Raman images were acquired and studied for fiber-enhanced gas Raman signals and unwanted background signals in HC-PCF [YAN-5]. According to the results, the spatial distribution of the fused silica background at 1061 cm^{-1} was mainly at the first ring of the surrounding cladding microstructure (Figure 10), while the Raman signal of the target gas mainly located in the center of the fiber core (Figure 10). The effect of the spatial filtering can be simulated with the Raman image of the HC-532 fiber. As a result, the separation of the silica signal and the gas signal reached a maximum with a 3.9 µm pinhole diameter [YAN-5].

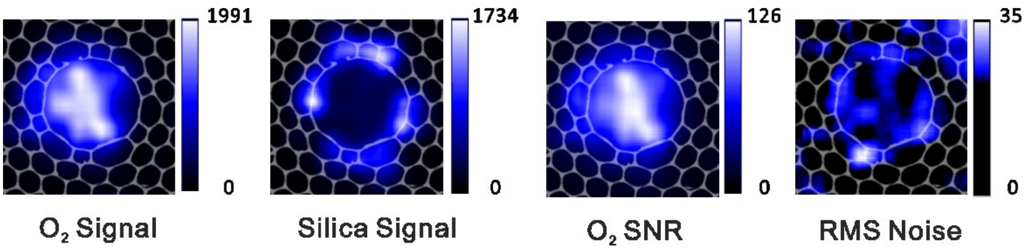

Figure 10: *Raman images of photonic crystal fiber. Reproduced from [YAN-5] with permission from the American Chemical Society. Copyright 2017 American Chemical Society. The Raman scattering of oxygen (1555 cm^{-1} peak) originates mainly from the central hollow core of the HC-PCF. The signal of the fused silica appears strong at the first ring of the surrounding microstructure. The baseline noise shows similar distribution as the silica signal, which is the main source of the baseline noise.*

The mode field diameter of the photonic crystal fiber is very small. Therefore, even very small offsets from the best coupling can cause a strong drop in the coupling efficiency, and thus increase the background. This effect has been demonstrated with liquid-filled HC-PCF in chapter 4.3 [YAN-3]. With an offset of 1 µm away from the optimal position, the gas Raman signal decreased tremendously and the unwanted background from the surrounding microstructure increased by one order of magnitude [YAN-5]. Therefore, a very precise alignment of the laser coupling is of key importance in fiber-enhanced Raman gas sensing. To achieve an easy-to-use gas monitoring system, an automated laser coupling system was achieved. With this coupling system, it was ensured that the gas sensing setup worked with optimal laser coupling. The automated system also simplified the procedure of aligning the photonic crystal fiber in the FERS setup.

4.6. FERS in selectively filled HC-PCF [YAN-6]

In this work, step-index light guidance in water-filled photonic crystal fibers across the whole visible and NIR spectral range was for the first time demonstrated. This waveguiding effect leads to strong fiber enhancement of Raman signal of antibiotics in the aqueous environment.

The liquid-of-interest can be filled selectively into the central hollow core of the HC-PCF. The refractive index of the aqueous-solution-filled fiber core (n = 1.33) can be higher than the effective refractive index of the cladding structure, as the effective refractive index is between that of air ($n_{air} = 1.00$) and the glass material ($n_{fused\ silica} = 1.46$), depending on the wavelength, the pitch size, and the air-filling fraction of the microstructure. In other words, the microstructured air-clad region can be utilized as a low refractive index cladding. The low effective refractive index of the cladding leads to the high numerical aperture of the filled HC-PCF and high performance of the light confinement in the liquid core. However, if the effective refractive index of the air-clad is close to or even higher than that of water, the HC-PCF is not suitable for Raman enhancement of aqueous solutions [YAN-6].

The effective refractive index can be predicted according to the wavelength (λ) the air-filling ratio (R), and the fiber pitch size (Λ) [70]. The effective refractive indices for all types of commercially available HC-PCFs were calculated and plotted together for comparison [YAN-6]. The plotted refractive indices of different types of HC-PCF (Figure 11) shows that only one fiber (Figure 11, black line) provides low enough refractive indices across the whole visible-NIR spectral range.

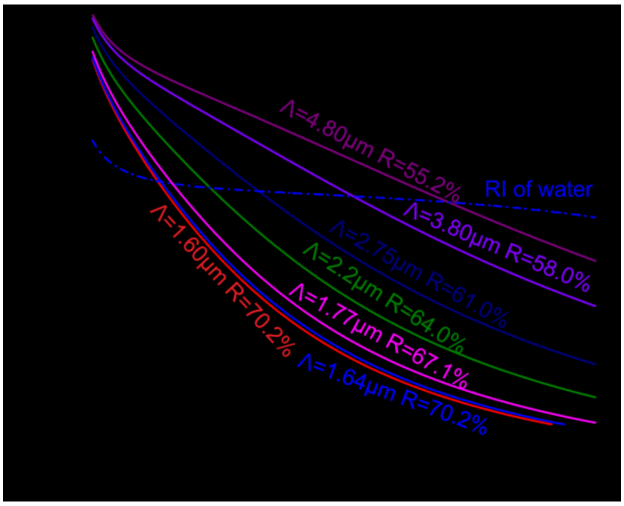

Figure 11: *Effective refractive indices for various possible pitch size (Λ) and air-filling ratio (R), of HC-PCFs. The effective refractive index needs to be lower than that of water to provide step-index guidance. Reproduced from [YAN-6] with permission from the American Chemical Society. Copyright 2017 American Chemical Society.*

In order to only fill the hollow core of the fiber with the liquid sample, it is necessary to preprocess the fiber ends and seal the air holes in the cladding region. In the conventional one-step method which was firstly reported in [71], a long bottleneck (200 µm [71] or even 1 mm [80] depends on the type of the fiber) is inevitable, as the heat always influences a large part of the fiber. The bottleneck region causes power loss and additional background, as total internal reflection is not happening at the bottleneck [80]. In this work, we demonstrate a novel two-step process for the fiber ends, in order to achieve excellent optical coupling and guidance [YAN-6]. The long bottleneck was avoided in this novel two-step process, and therefore optical guidance and coupling of the fiber ends were improved. The process steps were as follows [YAN-6]:

Step 1: A piece of HC-PCF is fixed on the fiber splicer and then heat is applied. The fine-structured air cladding in the fiber melted and collapsed under the influence of the heat. The heating parameters were adjusted to collapse only the air cladding and keep the central hole still open.

Step 2: The fiber is precisely cleaved as close as possible to the edge of the fused region with a customized cleaving setup, consisting of a microscope and an adjustable diamond blade. With precise adjustment of the blade position, flat fiber ends were obtained, and a minimized length of the bottleneck of typically only 20 µm was achieved (Figure 12) [YAN-6].

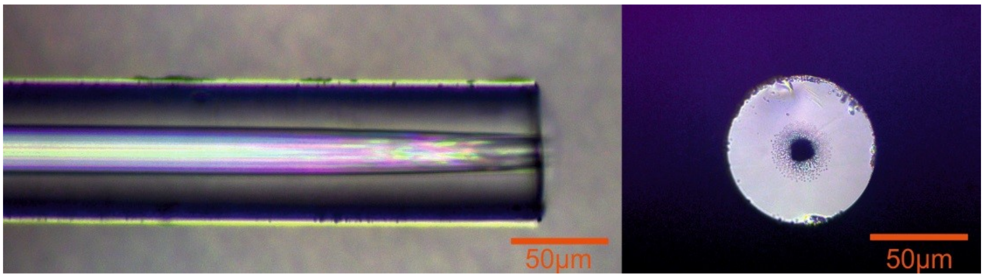

Figure 12: *Microscopic image of the selectively sealed HC-PCF. Flat fiber ends were achieved with a minimized length of the bottleneck (20 µm). Reproduced from [YAN-6] with permission from the American Chemical Society. Copyright 2017 American Chemical Society.*

According to the transmission spectra, an empty (air-filled) and a selectively filled fiber have different guidance mechanisms (Figure 13). The empty hollow fiber shows typical bandgap guidance in a narrow spectral region from 400 nm to 520 nm. However, the sensor fiber with selectively water-filled central hollow core displayed a tremendously improved broadband transmission spectrum from 400 nm up to the NIR range [YAN-6]. The transmission of the fiber was predicted based on the acceptance angle (dashed line in Figure 13). The water absorption bands appear at 0.98 µm and 1.2 µm [134], which were enhanced by the extended path length.

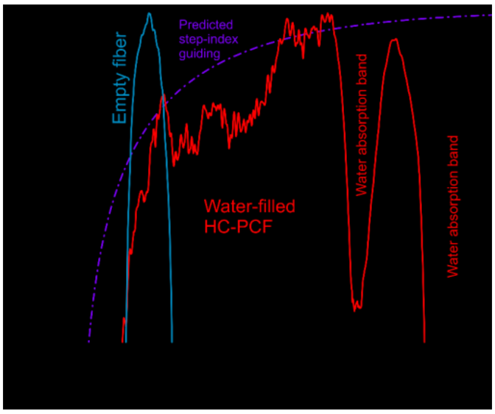

Figure 13: *The empty HC-PCF shows narrow bandgap guidance. By contrast, the HC-PCF with selectively water-filled central hollow core provides a broadband transmission spectrum from 400 nm up to the NIR range. Reproduced from [YAN-6] with permission from the American Chemical Society. Copyright 2017 American Chemical Society.*

Moxifloxacin, which is a fourth-generation fluoroquinolone antibacterial agent, was employed as the target analyte in the published work [YAN-6]. The moxifloxacin level has been reported to be 8 µM in plasma [135] after a single 400 mg oral administration. The elimination of moxifloxacin is mainly by renal excretion, and approximately 45% of moxifloxacin is excreted in urine unchanged. The moxifloxacin level in urine can reach a peak value of 161 µM after standard oral dose [136]. Broadband visible light guidance in aqueous solution was achieved in the liquid-filled HC-PCF for the first time [YAN-6]. Strong Raman enhancements were achieved with three laser excitation wavelengths at 532 nm, 676 nm, and 752 nm, showing prominent broadband capability as a sensor fiber. The intense characteristic Raman bands of moxifloxacin were detected at 1620 cm^{-1} and 1373 cm^{-1}, which are the νC=C-stretching vibration of the aromatic ring and the stretching vibration of the quinolone ring system of moxifloxacin [YAN-6], respectively (Figure 14). The 1620 cm^{-1} band was chosen for the concentration study. As a result, the limit-of-detection (LoD) of moxifloxacin was improved down to 1.7 µM (SNR=3). For the same concentration (20 µM), multiple characteristic Raman peaks were detected clearly in FERS (Figure 14, red), but not distinguishable in conventional Raman sensing with the same parameters (Figure 14, black). Therefore, FERS is capable of providing sufficient sensitivity in the clinically relevant measurements. Furthermore, only a volume of 4 nL liquid sample was needed in the sensor fiber, reduces the demand for sample volume tremendously [YAN-6]. Therefore, FERS has great potential as a diagnostic tool for rapid investigation of the antibiotic status of critically ill patients, which allowing quick adjustment of the dose for the maximized effectiveness of antibiotics administration.

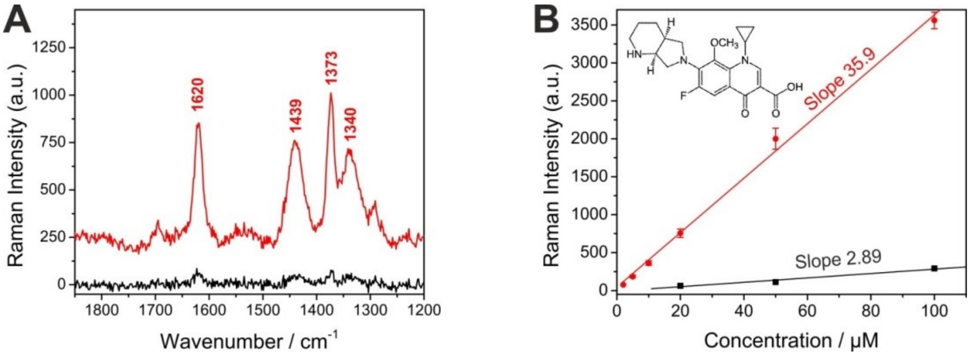

Figure 14: *Fiber-enhanced Raman spectroscopy of antibiotics. Reproduced from [YAN-6] with permission from the American Chemical Society. Copyright 2017 American Chemical Society. A: Comparison of the fiber-enhanced Raman spectrum (red) with the conventional Raman spectrum (black) of 20 µM moxifloxacin with* $\lambda_{exc.}$ *= 532 nm. The signal-to-noise ratios (SNR) of the Raman peak at 1620 cm*$^{-1}$ *(*ν*C=C-stretching vibration of the aromatic ring) was enhanced by one order of magnitude. The spectra in the graph are slightly vertically shifted for the sake of clarity. B: Raman intensity dependency from the drug concentration (fiber-enhanced Raman spectrum (red), conventional (black)). A very good linearity and thus a robust calibration can be achieved. The inset shows the chemical structure of moxifloxacin.*

5. Summary and outlook

This dissertation has presented the development of Raman sensors for biomolecules based on fiber-enhanced Raman spectroscopy (FERS). FERS was achieved by employing liquid-core optical fibers, which guided the light in the liquid media and cause strong light-matter interaction. In the first part of this thesis, the FERS technique was explained in detail, and the current state of research was introduced. Regarding the characteristics, such as fiber length, attenuation, and refractive index, liquid-core fibers such as polymer fibers and hollow-core photonic-crystal fibers (HC-PCFs) were thoroughly evaluated and discussed.

We demonstrated a combination of UV-resonance Raman spectroscopy (UV-RRS) and FERS, which increased the sensitivity for low-concentrated pharmaceuticals tremendously [YAN-1, YAN-2]. A complete model of fiber-enhanced Raman spectroscopy in liquid core fibers was established, and the enhancements of the Raman intensity with both non-absorbing and absorbing samples were thoroughly discussed [YAN-1]. This combined enhancement technique was also applied to detect bile pigments, which are target analytes in the diagnoses of the diseases associated with hyperbilirubinemia and hyperbiliverdinemia [YAN-2].

In order to overcome the performance issue caused by the poor optical quality of the polymer-based liquid-core fibers, we explored the implementation of HC-PCFs [YAN-3]. FERS in HC-PCF with shifted bandgap effect in the visible range was achieved for the first time [YAN-3]. Thus, the Raman scattering wavelengths are not anymore limited to the insensitive NIR range, and the Raman sensitivity of antibiotics was remarkably improved [YAN-3]. FERS was also applied to gas sensing [YAN-4]. Breath analysis is fast and allows the rapid diagnosis and continuous point-of-care observation of intensive care patients. With fiber-enhanced Raman gas sensing, a sensitive and reliable quantification of CH_4, CO_2, N_2, O_2 and their isotopic forms were achieved with just one single measurement [YAN-4].

We used a multi-channel Raman imaging setup to study the light confinement of the sensor fiber and the spatial distribution of the Raman signals in the fiber core [YAN-5]. The effects of the fiber type, fiber length, and the size of the spatial filter for gas-FERS were thoroughly analyzed and discussed [YAN-5]. The results showed that even small offsets in the coupling position could decrease the sensitivity of the system for more than one order of magnitude [YAN-5].

The narrow bandgap in non-selectively filled HC-PCFs limits the selection of the excitation wavelengths and Raman spectral range [YAN-6]. The liquid-of-interest was filled selectively into the central hollow core of the HC-PCF, and step-index guidance in the liquid-core was achieved in HC-PCFs, which allowed Raman sensing in a broad spectral range with various excitation wavelengths [YAN-6]. The step-index guiding in the selectively filled HC-PCF was demonstrated and compared with the original bandgap effect. According to the results, selectively filled HC-PCFs have a broad transmission, covering the entire visible-NIR range [YAN-6].

The results of this work showed that FERS can be used as a robust, easy-to-use, chemical selective and sensitive tool for detection of biomolecules and biogenic gases in various applications.

6. References

1. Raman, C.V. and K.S. Krishnan, *A New Type of Secondary Radiation.* Nature, 1928. **121(3048)**: p. 501-502.
2. Neugebauer, U., P. Rosch, and J. Popp, *Raman spectroscopy towards clinical application: drug monitoring and pathogen identification.* International Journal of Antimicrobial Agents, 2015. **46**: p. S35-S39.
3. Smith, E. and G. Dent, *Introduction, Basic Theory and Principles*, in *Modern Raman Spectroscopy – A Practical Approach*. 2005, John Wiley & Sons, Ltd. p. 1-21.
4. Workman, J.J.J., *Concise Handbook Of Analytical Spectroscopy, The: Theory, Applications, And Reference Materials (In 5 Volumes)*. 2016: World Scientific Publishing Company.
5. Smith, E. and G. Dent, *The Theory of Raman Spectroscopy*, in *Modern Raman Spectroscopy – A Practical Approach*. 2005, John Wiley & Sons, Ltd. p. 71-92.
6. McCreery, R.L., *Magnitude of Raman Scattering*, in *Raman Spectroscopy for Chemical Analysis*. 2005, John Wiley & Sons, Inc. p. 15-33.
7. Walrafen, G.E. and J. Stone, *Intensification of Spontaneous Raman Spectra by Use of Liquid Core Optical Fibers.* Applied Spectroscopy, 1972. **26**(6): p. 585-589.
8. Görner, H., M. Maier, and W. Kaiser, *Raman gain in liquid-core fibers.* Journal of Raman Spectroscopy, 1974. **2**(4): p. 363-371.
9. Ross, H.B. and W.M. McClain, *Liquid Core Optical Fibers in Raman Spectroscopy.* Appl. Spectrosc., 1981. **35**(4): p. 439-442.
10. Li, Z., et al., *EFFECT OF OPTICAL FIBER LOSS ON RESONANCE RAMAN SPECTRA OF SAMPLES WITH LOW CONCENTRATION.* Spectroscopy Letters, 2001. **34**(5): p. 569-578.
11. Gao, S., B. Huang, and Z. Li, *Application of liquid-core optical fiber in the measurements of Fourier transform Raman spectra ☆.* Chemical Physics Letters, 2004. **392**(1-3): p. 123-126.
12. Xu, W.Q., et al., *Ultrasensitive detection of 1,4-bis(4-vinylpyridyl)phenylene in a small volume of low refractive index liquid by surface-enhanced Raman scattering-active light waveguide.* Applied Spectroscopy, 2004. **58**(4): p. 414-419.
13. Keller, B.K., M.D. DeGrandpre, and C.P. Palmer, *Waveguiding properties of fiber-optic capillaries for chemical sensing applications.* Sensors and Actuators B: Chemical, 2007. **125**(2): p. 360-371.
14. Bescherer, K., J.A. Barnes, and H.P. Loock, *Absorption measurements in liquid core waveguides using CRD spectroscopy.* Anal Chem, 2013.
15. Altkorn, R., et al., *Intensity Considerations in Liquid Core Optical Fiber Raman Spectroscopy.* Appl. Spectrosc., 2001. **55**(4): p. 373-381.
16. Qi, D.H. and A.J. Berger, *Correction method for absorption-dependent signal enhancement by a liquid-core optical fiber.* Applied Optics, 2006. **45**(3): p. 489-494.
17. Frosch, T., et al., *In vitro polarization-resolved resonance Raman studies of the interaction of hematin with the antimalarial drug chloroquine.* Journal of Raman Spectroscopy, 2004. **35**(10): p. 819-821.
18. Frosch, T., et al., *In situ localization and structural analysis of the malaria pigment hemozoin.* Journal of Physical Chemistry B, 2007. **111**(37): p. 11047-11056.
19. Frosch, T., et al., *Device for Raman difference spectroscopy.* Analytical Chemistry, 2007. **79**(16): p. 6159-6166.
20. Wood, B.R., et al., *Raman imaging of hemozoin within the food vacuole of Plasmodium falciparum trophozoites.* Febs Letters, 2003. **554**(3): p. 247-252.
21. Dress, P., et al., *Physical analysis of teflon coated capillary waveguides.* Sensors and Actuators B: Chemical, 1998. **51**(1-3): p. 278-284.

22. Altkorn, R., et al., *Low-loss liquid-core optical fiber for low-refractive-index liquids: fabrication, characterization, and application in Raman spectroscopy.* Applied Optics, 1997. **36**(34): p. 8992-8998.

23. Altkorn, R., I. Koev, and A. Gottlieb, *Waveguide capillary cell for low-refractive-index liquids.* Applied Spectroscopy, 1997. **51**(10): p. 1554-1558.

24. Altkorn, R., I. Koev, and M.J. Pelletier, *Raman Performance Characteristics of Teflon®-AF 2400 Liquid-Core Optical-Fiber Sample Cells.* Appl. Spectrosc., 1999. **53**(10): p. 1169-1176.

25. Song, L., et al., *Application of liquid waveguide to Raman spectroscopy in aqueous solution.* Applied Spectroscopy, 1998. **52**(10): p. 1364-1367.

26. Pelletier, M.J. and R. Altkorn, *Efficient Elimination of Fluorescence Background from Raman Spectra Collected in a Liquid Core Optical Fiber.* Applied Spectroscopy, 2000. **54**(12): p. 1837-1841.

27. Marquardt, B.J., et al., *A Raman waveguide detector for liquid chromatography.* Analytical Chemistry, 1999. **71**(21): p. 4808-14.

28. Holtz, M., P.K. Dasgupta, and G. Zhang, *Small-Volume Raman Spectroscopy with a Liquid Core Waveguide.* Analytical Chemistry, 1999. **71**(14): p. 2934-2938.

29. Gooijer, C., et al., *On-line coupling of column liquid chromatography and raman spectroscopy using a liquid core waveguide.* Analytical Chemistry, 1999. **71**(20): p. 4575-4579.

30. Pelletier, M.J. and R. Altkorn, *Raman sensitivity enhancement for aqueous protein samples using a liquid-core optical-fiber cell.* Analytical Chemistry, 2001. **73**(6): p. 1393-7.

31. Dijkstra, R.J., et al., *Liquid-core waveguide technology for coupling column liquid chromatography and Raman spectroscopy.* Journal of Chromatography A, 2001. **918**(1): p. 25-36.

32. Tian, Y., et al., *Raman sensitivity enhancement for aqueous absorbing sample using Teflon-AF 2400 liquid core optical fibre cell.* Anal Chim Acta, 2007. **581**(1): p. 154-8.

33. Qi, D. and A.J. Berger, *Quantitative concentration measurements of creatinine dissolved in water and urine using Raman spectroscopy and a liquid core optical fiber.* Journal of Biomedical Optics, 2005. **10**(3): p. 031115.

34. Qi, D. and A.J. Berger, *Quantitative analysis of Raman signal enhancement from aqueous samples in liquid core optical fibers.* Applied Spectroscopy, 2004. **58**(10): p. 1165-71.

35. Dijkstra, R.J., et al., *Hyphenation of column liquid chromatography and Raman spectroscopy via a liquid-core waveguide: chemometrical elimination of spectral eluent background.* Anal Chim Acta, 2004. **519**(2): p. 129-136.

36. Dress, P., et al., *Water-Core Waveguide for Pollution Measurements in the Deep Ultraviolet.* Appl. Opt., 1998. **37**(21): p. 4991-4997.

37. Tsunoda, K., et al., *Liquid core waveguide spectrophotometry for the sensitive determination of nitrite in river water samples.* Analytical Sciences, 2006. **22**(7): p. 1017-1019.

38. George, C., et al., *A new approach for studying aqueous phase OH kinetics: application of Teflon waveguides.* Physical Chemistry Chemical Physics, 2003. **5**(8): p. 1562-1569.

39. Li, Q.Y., et al., *Portable flow-injection analyzer with liquid-core waveguide based fluorescence, luminescence, and long path length absorbance detector.* Anal Chim Acta, 2003. **479**(2): p. 151-165.

40. Larsson, H. and P.K. Dasgupta, *Liquid core waveguide-based optical spectrometry for field estimation of dissolved BTEX compounds in groundwater - A feasibility study.* Anal Chim Acta, 2003. **485**(2): p. 155-167.

41. Robles, T., D. Paige, and C. Anastasio, *Lens-coupled liquid core waveguide for ultraviolet-visible absorption spectroscopy.* Review of Scientific Instruments, 2006. **77**(7): p. 073103.

42. Sugiya, K., M. Harada, and T. Okada, *Water-ice chip with liquid-core waveguide functionality. Toward lab on ice.* Lab Chip, 2009. **9**(8): p. 1037-9.

43. Gopalakrishnan, N., et al., *UV patterned nanoporous solid-liquid core waveguides.* Optics Express, 2010. **18**(12): p. 12903-8.

44. Porter, J., et al., *Cutting thin sheet metal with a water jet guided laser using various cutting distances, feed speeds and angles of incidence.* The International Journal of Advanced Manufacturing Technology, 2007. **33**(9-10): p. 961-967.

45. Persichetti, G., G. Testa, and R. Bernini, *High sensitivity UV fluorescence spectroscopy based on an optofluidic jet waveguide.* Optics Express, 2013. **21**(20): p. 24219-30.

46. Persichetti, G., G. Testa, and R. Bernini. *Liquid jet waveguide for Raman spectroscopy*. 2014.

47. Persichetti, G., G. Testa, and R. Bernini, *Optofluidic jet waveguide enhanced Raman spectroscopy.* Sensors and Actuators B: Chemical, 2015. **207**: p. 732-739.

48. Persichetti, G. and R. Bernini, *Water monitoring by optofluidic Raman spectroscopy for in situ applications.* Talanta, 2016. **155**: p. 145-52.

49. Knight, J.C., et al., *Photonic band gap guidance in optical fibers.* Science, 1998. **282**(5393): p. 1476-8.

50. Cregan, R.F., et al., *Single-mode photonic band gap guidance of light in air.* Science, 1999. **285**(5433): p. 1537-1539.

51. Russell, P., *Photonic crystal fibers.* Science, 2003. **299**(5605): p. 358-62.

52. Benabid, F. and P.J. Roberts, *Linear and nonlinear optical properties of hollow core photonic crystal fiber.* Journal of Modern Optics, 2011. **58**(2): p. 87-124.

53. Antonoppolos, G., et al., *Experimental demonstration of refractive index scaling in photonic bandgap fibers*, in *Conference on Lasers and Electro-Optics/International Quantum Electronics* 2004: San Francisco, California, United States. p. 2 pp. vol.2.

54. Birks, T.A., et al., *Scaling laws and vector effects in bandgap-guiding fibres.* Optics Express, 2004. **12**(1): p. 69-74.

55. Antonopoulos, G., et al., *Experimental demonstration of the frequency shift of bandgaps in photonic crystal fibers due to refractive index scaling.* Optics Express, 2006. **14**(7): p. 3000-3006.

56. Khetani, A., et al., *Hollow core photonic crystal fiber for monitoring leukemia cells using surface enhanced Raman scattering (SERS).* Biomed Opt Express, 2015. **6**(11): p. 4599-609.

57. Khetani, A., et al., *Hollow core photonic crystal fiber as a reusable Raman biosensor.* Opt Express, 2013. **21**(10): p. 12340-50.

58. Khetani, A., et al., *Monitoring of heparin concentration in serum by Raman spectroscopy within hollow core photonic crystal fiber.* Optics Express, 2011. **19**(16): p. 15244-15254.

59. Naji, M., et al. *A novel method of using hollow-core photonic crystal fiber as a Raman biosensor*. 2008.

60. Yang, X., et al., *Direct molecule-specific glucose detection by Raman spectroscopy based on photonic crystal fiber.* Analytical and Bioanalytical Chemistry, 2012. **402**(2): p. 687-691.

61. Yang, X., et al., *Hollow-Core Photonic Crystal Fibers for Surface-Enhanced Raman Scattering Probes.* International Journal of Optics, 2011. **2011**: p. 1-11.

62. Yang, X., et al., *High-sensitivity molecular sensing using hollow-core photonic crystal fiber and surface-enhanced Raman scattering.* J. Opt. Soc. Am. A, 2010. **27**(5): p. 977-984.

63. Tiwari, V.S., et al., *Optimum Size and Volume of Nanoparticles Within Hollow Core Photonic Crystal Fiber.* Ieee Journal of Selected Topics in Quantum Electronics, 2014. **20**(3).

64. Zhang, Y., et al., *Liquid core photonic crystal fiber sensor based on surface enhanced Raman scattering.* Applied Physics Letters, 2007. **90**(19): p. 193504.

65. Khetani, A., et al., *Hollow core photonic crystal fiber as a reusable Raman biosensor.* Optics Express, 2013. **21**(10): p. 12340-50.

66. Hanf, S., et al., *Fast and highly sensitive fiber-enhanced Raman spectroscopic monitoring of molecular H2 and CH4 for point-of-care diagnosis of malabsorption disorders in exhaled human breath.* Anal Chem, 2015. **87**(2): p. 982-8.

67. Jochum, T., et al., *All-in-one: a versatile gas sensor based on fiber enhanced Raman spectroscopy for monitoring postharvest fruit conservation and ripening.* Analyst, 2016. **141**(6): p. 2023-2029.

68. Jochum, T., et al., *Direct Raman Spectroscopic Measurements of Biological Nitrogen Fixation under Natural Conditions: An Analytical Approach for Studying Nitrogenase Activity.* Analytical Chemistry, 2016.

69. Joannopoulos, J.D., R.D. Meade, and J.N. Winn, *Photonic Crystals: Molding the Flow of Light*. 1995: Princeton University Press.

70. Mahnke, C. and F. Mitschke, *A useful approximation for the cladding index of holey fibers.* Applied Physics B-Lasers and Optics, 2010. **99**(1-2): p. 241-245.

71. Smolka, S., M. Barth, and O. Benson, *Highly efficient fluorescence sensing with hollow core photonic crystal fibers.* Optics Express, 2007. **15**(20): p. 12783-91.

72. Han, Y., et al., *Index-guiding liquid-core photonic crystal fiber for solution measurement using normal and surface-enhanced Raman scattering.* Optical Engineering, 2008. **47**(4).

73. Eftekhari, F., et al., *A comparative study of Raman enhancement in capillaries.* Journal of Applied Physics, 2011. **109**(11): p. 113104.

74. Nielsen, K., et al., *Selective filling of photonic crystal fibres.* Journal of Optics A: Pure and Applied Optics, 2005. **7**(8): p. L13.

75. Shi, C., et al., *Inner wall coated hollow core waveguide sensor based on double substrate surface enhanced Raman scattering.* Applied Physics Letters, 2008. **93**(15): p. 153101.

76. Xiao, L., et al., *Fabrication of selective injection microstructured optical fibers with a conventional fusion splicer.* Optics Express, 2005. **13**(22): p. 9014-22.

77. Smolka, S., M. Barth, and O. Benson, *Selectively coated photonic crystal fiber for highly sensitive fluorescence detection.* Applied Physics Letters, 2007. **90**(11): p. 111101.

78. Irizar, J., *Raman Spectroscopy of Colloidal Nanoparticles in Liquid Core Photonic Crystal Fibers*, in *Electrical and Computer Engineering*. 2008, University of Toronto.

79. Irizar, J., et al. *Raman Spectroscopy of Nanoparticles in Photonic Crystal Fibers*. in *Conference on Lasers and Electro-Optics/Quantum Electronics and Laser Science Conference and Photonic Applications Systems Technologies*. 2008. San Jose, California: Optical Society of America.

80. Irizar, J., et al., *Raman Spectroscopy of Nanoparticles Using Hollow-Core Photonic Crystal Fibers.* Selected Topics in Quantum Electronics, IEEE Journal of, 2008. **14**(4): p. 1214-1222.

81. Aghaie, K.Z., M.J.F. Digonnet, and S.H. Fan, *Optimization of the splice loss between photonic-bandgap fibers and conventional single-mode fibers.* Optics Letters, 2010. **35**(12): p. 1938-1940.

82. Cordeiro, C.M.B., et al., *Lateral access to the holes of photonic crystal fibers - selective filling and sensing applications.* Optics Express, 2006. **14**(18): p. 8403-8412.

83. Huang, Y., Y. Xu, and A. Yariv, *Fabrication of functional microstructured optical fibers through a selective-filling technique.* Applied Physics Letters, 2004. **85**(22): p. 5182.

84. Kuo, S.M., et al., *Liquid crystal modified photonic crystal fiber (LC-PCF) fabricated with an un-cured SU-8 photoresist sealing technique for electrical flux measurement.* Optics Express, 2011. **19**(19): p. 18372-9.

85. Hanf, S., et al., *Fast and highly sensitive fiber enhanced Raman spectroscopic monitoring of molecular H2 and CH4 for point-of-care diagnosis of malabsorption disorders in exhaled human breath.* Analytical Chemistry, 2015. **87**(2): p. 982-988.

86. Hehre, W.J., *Self-Consistent Molecular-Orbital Methods. I. Use of Gaussian Expansions of Slater-Type Atomic Orbitals.* The Journal of Chemical Physics, 1969. **51**(6): p. 2657.

87. White, N.J., *Artemisinin resistance-the clock is ticking.* Lancet, 2010. **376**(9758): p. 2051-2052.

88. *Global plan for artemisinin resistance containment (GPARC)*. 2011, Switzerland WHO Press.

89. Dondorp, A.M., et al., *Artemisinin Resistance in Plasmodium falciparum Malaria.* New England Journal of Medicine, 2009. **361**(5): p. 455-467.

90. Frosch, T. and J. Popp, *Structural analysis of the antimalarial drug halofantrine by means of Raman spectroscopy and density functional theory calculations.* J Biomed Opt, 2010. **15**(4): p. 041516.

91. Robert, B., *Resonance Raman spectroscopy.* Photosynthesis Research, 2009. **101**(2): p. 147-155.

92. Frosch, T., et al., *Structural Analysis of the Anti-Malaria Active Agent Chloroquine under Physiological Conditions.* The Journal of Physical Chemistry B, 2007. **111**(7): p. 1815-1822.

93. Frosch, T., M. Schmitt, and J. Popp, *Raman spectroscopic investigation of the antimalarial agent mefloquine.* Anal Bioanal Chem, 2007. **387**(5): p. 1749-57.

94. Frosch, T., M. Schmitt, and J. Popp, *In situ UV resonance Raman micro-spectroscopic localization of the antimalarial quinine in cinchona bark.* Journal of Physical Chemistry B, 2007. **111**(16): p. 4171-4177.

95. Frosch, T., et al., *Ultrasensitive in situ tracing of the alkaloid dioncophylline A in the tropical liana Triphyophyllum peltatum by applying deep-UV resonance Raman microscopy.* Analytical Chemistry, 2007. **79**(3): p. 986-993.

96. Frosch, T., et al., *In vivo localization and identification of the antiplasmodial alkaloid dioncophylline A in the tropical liana Triphyophyllum peltatum by a combination of fluorescence, near infrared Fourier transform Raman microscopy, and density functional theory calculations.* Biopolymers, 2006. **82**(4): p. 295-300.

97. Pagola, S., et al., *The structure of malaria pigment beta-haematin.* Nature, 2000. **404**(6775): p. 307-310.

98. Kikuchi, G., T. Yoshida, and M. Noguchi, *Heme oxygenase and heme degradation.* Biochemical and Biophysical Research Communications, 2005. **338**(1): p. 558-567.

99. Houlihan, D.D., M.J. Armstrong, and P.N. Newsome, *Investigation of jaundice.* Medicine, 2011. **39**(9): p. 518-522.

100. Ryter, S.W., *Bile pigments in pulmonary and vascular disease.* Frontiers in pharmacology, 2012. **3**.

101. Vitek, L. and J.D. Ostrow, *Bilirubin chemistry and metabolism; harmful and protective aspects.* Current pharmaceutical design, 2009. **15**(25): p. 2869-2883.

102. Greenberg, A.J., I. Bossenmaier, and S. Schwartz, *Green jaundice.* The American journal of digestive diseases, 1971. **16**(10): p. 873-880.

103. Wood, B.R., et al., *Resonance Raman spectroscopy reveals new insight into the electronic structure of beta-hematin and malaria pigment.* J Am Chem Soc, 2004. **126**(30): p. 9233-9.

104. Frosch, T., et al., *In Situ Localization and Structural Analysis of the Malaria Pigment Hemozoin.* J. Phys. Chem. B, 2007. **111**(37): p. 11047-11056.

105. Cinta-Pinzaru, S., et al., *FT-Raman and NIR-SERS characterization of the antimalarial drugs chloroquine and mefloquine and their interaction with hematin.* Journal of Raman Spectroscopy, 2006. **37**(1-3): p. 326-334.

106. Wood, B.R., et al., *Resonance Raman spectroscopy reveals new insight into the electronic structure of beta-hematin and malaria pigment.* Journal of the American Chemical Society, 2004. **126**(30): p. 9233-9239.

107. Wood, B.R. and D. McNaughton, *Raman excitation wavelength investigation of single red blood cells in vivo.* Journal of Raman Spectroscopy, 2002. **33**(7): p. 517-523.

108. Torres, I.P., et al., *Measurement of hemoglobin oxygen saturation using Raman microspectroscopy and 532-nm excitation.* Journal of Applied Physiology, 2008. **104**(6): p. 1809-1817.

109. Gåfvels, M., et al., *A novel mutation in the biliverdin reductase ‐ A gene combined with liver cirrhosis results in hyperbiliverdinaemia (green jaundice).* Liver International, 2009. **29**(7): p. 1116-1124.

110. de Molina, F.J.G. and R. Ferrer, *Appropriate antibiotic dosing in severe sepsis and acute renal failure: factors to consider.* Critical Care, 2011. **15**(4).

111. Pletz, M.W., et al., *Pharmacokinetics of moxifloxacin in patients with severe sepsis or septic shock.* Intensive Care Med, 2010. **36**(6): p. 979-83.

112. Pea, F., P. Viale, and M. Furlanut, *Antimicrobial therapy in critically ill patients: a review of pathophysiological conditions responsible for altered disposition and pharmacokinetic variability.* Clin Pharmacokinet, 2005. **44**(10): p. 1009-34.

113. Barlam, T.F., et al., *Implementing an Antibiotic Stewardship Program: Guidelines by the Infectious Diseases Society of America and the Society for Healthcare Epidemiology of America.* Clin Infect Dis, 2016. **62**(10): p. e51-77.

114. Steinmetz, T., et al., *Association of vancomycin serum concentrations with efficacy in patients with MRSA infections: a systematic review and meta-analysis.* Clin Microbiol Infect, 2015. **21**(7): p. 665-73.

115. Troke, P.F., H.P. Hockey, and W.W. Hope, *Observational study of the clinical efficacy of voriconazole and its relationship to plasma concentrations in patients.* Antimicrob Agents Chemother, 2011. **55**(10): p. 4782-8.

116. Vishwanathan, K., M.G. Bartlett, and J.T. Stewart, *Determination of moxifloxacin in human plasma by liquid chromatography electrospray ionization tandem mass spectrometry.* Journal of Pharmaceutical and Biomedical Analysis, 2002. **30**(4): p. 961-968.

117. Lemoine, T., et al., *Determination of moxifloxacin (BAY 12-8039) in plasma and lung tissue by high-performance liquid chromatography with ultraviolet detection using a fully automated extraction method with a new polymeric cartridge.* Journal of Chromatography B, 2000. **742**(2): p. 247-254.

118. Vella, J., et al., *A simple HPLC-UV method for the determination of ciprofloxacin in human plasma.* Journal of Chromatography B-Analytical Technologies in the Biomedical and Life Sciences, 2015. **989**: p. 80-85.

119. Benabid, F., *Hollow-core photonic bandgap fibre: new light guidance for new science and technology.* Philosophical Transactions of the Royal Society A - Mathematical Physical and Engineering Sciences, 2006. **364**(1849): p. 3439-3462.

120. Benabid, F., et al., *Compact, stable and efficient all-fibre gas cells using hollow-core photonic crystal fibres.* Nature, 2005. **434**(7032): p. 488-491.

121. Benabid, F., et al., *Stimulated Raman Scattering in Hydrogen-Filled Hollow-Core Photonic Crystal Fiber.* Science, 2002. **298**(5592): p. 399-402.

122. Russell, P., *Photonic Crystal Fibers.* Science, 2003. **299**(5605): p. 358-362.

123. Furlanut, M., et al., *Pharmacokinetic aspects of levofloxacin 500 mg once daily during sequential intravenous/oral therapy in patients with lower respiratory tract infections.* J Antimicrob Chemother, 2003. **51**(1): p. 101-6.

124. Frosch, T., et al., *Investigation of gas exchange processes in peat bog ecosystems by means of innovative Raman gas spectroscopy.* Anal Chem, 2013. **85**(3): p. 1295-9.

125. Keiner, R., et al., *Raman Spectroscopy-An Innovative and Versatile Tool To Follow the Respirational Activity and Carbonate Biomineralization of Important Cave Bacteria.* Anal Chem, 2013. **85**: p. 8708−8714.

126. Keiner, R., et al., *Enhanced Raman multigas sensing – a novel tool for control and analysis of 13CO2 labeling experiments in environmental research.* The Analyst, 2014.

127. Salter, R., J. Chu, and M. Hippler, *Cavity-enhanced Raman spectroscopy with optical feedback cw diode lasers for gas phase analysis and spectroscopy.* Analyst, 2012. **137**(20): p. 4669-76.

128. Buric, M.P., et al., *Enhanced spontaneous Raman scattering and gas composition analysis using a photonic crystal fiber.* Appl. Opt., 2008. **47**(23): p. 4255-4261.

129. Buric, M.P., et al., *Improved sensitivity gas detection by spontaneous Raman scattering.* Appl. Opt., 2009. **48**(22): p. 4424-4429.

130. Rosman, K.J.R. and P.D.P. Taylor, *Isotopic compositions of the elements 1997.* Pure and Applied Chemistry, 1998. **70**(1): p. 217-235.

131. Okuno, M. and H. Hamaguchi, *Multifocus confocal Raman microspectroscopy for fast multimode vibrational imaging of living cells.* Optics Letters, 2010. **35**(24): p. 4096-4098.

132. Brueckner, M., et al., *Fiber array based hyperspectral Raman imaging for chemical selective analysis of malaria-infected red blood cells.* Anal Chim Acta, 2015. **894**: p. 76-84.

133. Samuel, A.Z., et al., *Rapid microstructure characterization of polymer thin films with 2D-array multifocus Raman microspectroscopy.* Analyst, 2015. **140**(6): p. 1847-1851.

134. George M. Hale, M.R.Q., *Optical Constants of Water in the 200-nm to 200-µm Wavelength Regin.* Applied Optics, 1973. **12**(3): p. 555-563.

135. Soman, A., et al., *Concentrations of moxifloxacin in serum and pulmonary compartments following a single 400 mg oral dose in patients undergoing fibre-optic bronchoscopy.* J Antimicrob Chemother, 1999. **44**(6): p. 835-8.

136. Wagenlehner, F.M., et al., *Concentrations of moxifloxacin in plasma and urine, and penetration into prostatic fluid and ejaculate, following single oral administration of 400 mg to healthy volunteers.* Int J Antimicrob Agents, 2008. **31**(1): p. 21-6.

7. Manuscripts

[YAN-1]

Title	**Ultrasensitive fiber-enhanced UV resonance Raman sensing of drugs**
Authors	T. Frosch, D. Yan, J. Popp
Citation	Analytical Chemistry, 2013, 85 (13), pp 6264-6271

[YAN-2]

Title	**Fiber-enhanced Raman spectroscopic analysis as a novel method for diagnosis and monitoring of diseases related to hyperbilirubinemia and hyperbiliverdinemia**
Authors	D. Yan, C. Domes, R. Domes, T. Frosch, J. Popp, M.W. Pletz, T. Frosch
Citation	Analyst, 2016, 141 (21), pp 6104–6115

[YAN-3]

Title	**Fiber-enhanced Raman sensing of levofloxacin by PCF bandgap-shifting into the visible range**
Authors	D. Yan, J. Popp, M.W. Pletz, T. Frosch
Citation	Analytical Methods, 2018, 10 (6), pp 586–592

[YAN-4]

Title	**Fiber-enhanced Raman multigas spectroscopy: a versatile tool for environmental gas sensing and breath analysis**
Authors	S. Hanf, R. Keiner, D. Yan, J. Popp, T. Frosch
Citation	Analytical Chemistry, 2014, 86 (11), pp 5278–5285

[YAN-5]

Title	**Analysis of fiber-enhanced Raman gas sensing based on Raman chemical imaging**
Authors	D. Yan, J. Popp, T. Frosch
Citation	Analytical Chemistry, 2017, 89 (22), pp 12269–12275

[YAN-6]

Title	**Highly Sensitive Broadband Raman Sensing of Antibiotics in Step-Index Hollow-Core Photonic Crystal Fibers**
Authors	D. Yan, J. Popp, M.W. Pletz, T. Frosch
Citation	ACS Photonics, 2017, 4 (1), pp 138–145

7.1. Ultrasensitive fiber-enhanced UV resonance Raman sensing of drugs

Reproduced from Torsten Frosch, Di Yan, Juergen Popp; Ultrasensitive Fiber-enhanced UV Resonance Raman Sensing of Drugs. Analytical Chemistry (2013), 85, 6264−6271 with permission from American Chemical Society.

analytical chemistry
Article
pubs.acs.org/ac

Ultrasensitive Fiber Enhanced UV Resonance Raman Sensing of Drugs

Torsten Frosch,*[†,‡,∥] Di Yan,[†,∥] and Jürgen Popp[†,‡,§]

[†]Institute of Photonic Technology, Jena, Germany
[‡]Friedrich-Schiller University, Institute for Physical Chemistry, Jena, Germany
[§]Friedrich-Schiller University, Abbe School of Photonics, Jena, Germany

Supporting Information

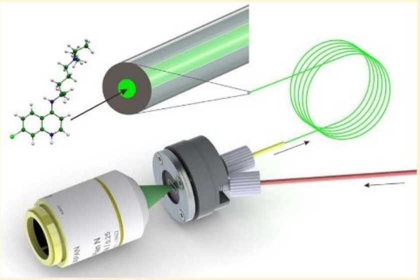

ABSTRACT: Fiber enhanced UV resonance Raman spectroscopy is introduced for chemical selective and ultrasensitive analysis of drugs in aqueous media. The application of hollow-core optical fibers provides a miniaturized sample container for analyte flow and efficient light-guiding, thus leading to strong light−analyte interactions and highly improved analytical sensitivity with the lowest sample demand. The Raman signals of the important antimalaria drugs chloroquine and mefloquine were strongly enhanced utilizing deep UV and electronic resonant excitation augmented by fiber enhancement. An experimental design was developed and realized for reproducible and quantitative Raman fiber sensing, thus the enhanced Raman signals of the pharmaceuticals show excellent linear relationship with sample concentration. A thorough model accounts for the different effects on signal performance in resonance Raman fiber sensing, and conclusions are drawn how to improve fiber enhanced Raman spectroscopy (FERS) for chemical selective analysis with picomolar sensitivity.

Novel photonic analytical techniques develop rapidly due to innovative technological improvements in highly efficient and miniaturized lasers, detectors, optical fibers, and components. Thus compact and hand-held devices allow nowadays for onsite detection of biomolecules with high sensitivity and selectivity and become essential tools that pave the way for new discoveries in biomedical and environmental research. In pharmaceutical research it is crucial to develop high-throughput assays for rapid screening of drug efficacy. One prominent example is the urgent need[1] for a tailor-made design of new antimalarial active agents based on the elucidation of their molecular mode of action.[1b,2] Therefore, novel analytical techniques with high chemical selectivity and sensitivity are needed[3] to elucidate the details of chemical drug−target-interactions in *in vitro* assays and consequently for the detection of antimalarial drugs (such as chloroquine (CQ)[4] and mefloquine (MQ)[1b]) at physiological concentrations in an aqueous environment. Raman spectroscopy is a chemical selective, noninvasive technique that has evolved as an extremely powerful analytical tool in malaria research.[5] However Raman scattering is an intrinsically weak process and therefore needs elaborated enhancement techniques[6] for tracing of low-concentration analytes. Equation 1 provides an expression for the Stokes Raman scattering intensity

$$I_{\text{Stokes}} \propto N I_0 (\omega_0 - \omega_r)^4 |\alpha|^2 \qquad (1)$$

where N is the number of molecules, I_0 the incoming excitation intensity, ω_0 the Raman excitation frequency, ω_r the excited vibrational frequency, and α the molecules' polarizabilty. Equation 1 reveals that in order to enhance the Stokes Raman intensity (I_{Stokes}), four parameters can be discovered. Thus I_{Stokes} can either be increased by application of stronger excitation intensity (I_0), higher excitation frequencies, i.e., UV excitation[6a,b] or the frequency dependency of the polarizabilty α can be utilized by resonantly matching the excitation frequency with an electronic transition of the molecule. Furthermore, the number (N) of target molecules that are involved in the Raman scattering process can be increased. In conventional Raman spectroscopy, the signal is excited and collected from a small scattering volume, which is limited by the scattering volume in the focus spot of the optical setup (Figure 1A). This limitation can be overcome with the help of liquid core optical fibers, where light and analyte are both guided within the fiber hollow core and thus the analyte is efficiently excited over an extended path length and the number of scattering molecules is strongly increased (Figure 1B). Additionally, the required sample amount is significantly reduced by the minimized volume of the fiber hollow core. Thus, fiber enhanced Raman sensing provides an opportunity to detect traces of analytes at very low sample volume. In other words, the Raman fiber sensor can be seen as an optimized cuvette and provides highly enhanced analytical sensitivity

Received: February 3, 2013
Accepted: May 28, 2013
Published: June 11, 2013

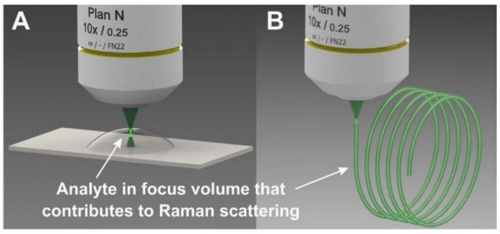

Figure 1. Comparison of different detection schemes: (A) In conventional measurements, the interaction volume of excitation light and analyte is limited by the focusing optic of the laser beam, thus the excited and acquired Raman signal originates only from a very limited focus volume. (B) The excitation light is guided over an extended range within the hollow core of the optical fiber, which also functions as a minimized analyte container. Thus an excellent light−analyte-interaction is achieved in fiber enhanced Raman spectroscopy, and a high number of molecules contributes to the Raman signal.

In order to achieve light guiding in the liquid core of the fiber by means of total internal reflection (TIR), a capillary of Teflon AF material was chosen. Teflon AF 2400 has the lowest refractive index of all known polymeric materials (n = 1.29, which is lower than that of the water core n = 1.33), has good optical quality, and shows no fluorescence.[7] Teflon AF fibers were used for Raman analysis of transparent samples[8] and were coupled with chromatography,[9] and it was shown that Raman spectra of absorbing samples should be corrected and were decreased at high concentrations.[10] Fiber enhanced UV resonance Raman spectroscopy (UV-RRS) was not discovered yet, despite the unique abilities for bioanalysis.[11] UV-RRS is also an important analytical tool for the investigation of antimalarials, since the Raman signals of the vibrational modes of the quinolone-unit of the drugs can be selectively enhanced by tuning the laser excitation wavelengths into the electronic absorption bands of the molecules.[6a,b,12]

■ MATERIALS AND METHODS

Chemicals. All chemicals were purchased from Sigma-Aldrich and used without further purification. Ultrapure deionized water (conductivity lower than 0.056 μS/cm) was prepared with an ultraclear water feed system from SG Water GmbH. Mefloquine was kindly provided by Roche Diagnostic GmbH. The UV−vis absorption spectra were acquired with a Specord M400 (Carl Zeiss Jena) spectrometer. The sample absorption values at λ = 244 nm and λ = 257 nm are for Chloroquine: 3352 mol^{-1} mm^{-1} and 3845 mol^{-1} mm^{-1} and for Mefloquine: 261 mol^{-1} mm^{-1} and 489 mol^{-1} mm^{-1}, respectively (see Figure SM1 in the Supporting Information).

Experimental Setup for Fiber Enhanced Raman Spectroscopy. A fiber of Teflon AF 2400 with an outer diameter o.d. = 889 μm, inner diameter i.d. = 168 μm, length L_p = 43 cm, and inner volume of 38 μL was applied as a hollow core optical waveguide. For quantitative and reproducible Raman analysis, a stable optical coupling geometry of the fiber is of key importance. This was achieved by the design of a custom-made fiber-adapter assembly (Figure 2A), which provides an optical window for coupling the laser light into the fiber and two side-ports for analyte flow and convenient cleaning procedure. The assembly provides minimal dead volume (path-length L_d = 1 mm) and all tubing consist of PEEK (polyether ether ketone), a material with excellent mechanical and chemical resistances.

The laser excitation light was focused into the fibers with an objective lens, and the backscattered Raman signal was collected by the same objective (Figure 2B). Raman spectra were acquired with a LabRAM systems (Horiba JobinYvon, HR800) equipped with liquid-nitrogen-cooled CCD detectors and laser excitation wavelengths: λ = 532 nm (Oxxius SLIM-532, I_{Laser} = 30 mW at the sample) as well as λ = 244 nm and λ = 257 nm (SHG, Innova300-MotoFreD, Coherent Inc., I_{Laser} = 0.5 mW and 2.4 mW at the sample, respectively). For visible wavelengths, an Olympus 10x/NA0.25 objective lens was used and the slit size was 100 μm (fiber image in the entrance slit plane, 470 μm) and for UV resonance Raman measurements, a UV achromatic objective of fused-silica/CaF$_2$ (LMU-15X-UVB/NA0.32) was employed with a hole size of 300 μm (fiber image in the entrance hole plane, 1109 μm). In order to avoid photodegradation of chloroquine and mefloquine in UV resonance Raman measurements, the samples were kept flowing through the fiber with the help of a syringe pump. The flow rate was set to 40 μL/s; thus, the speed of liquids in the Teflon AF fiber was about 0.6 m/s. The moving liquid media passed through the laser focus within a very short time and were not damaged by the laser radiation. The performance of the fiber enhanced Raman setup (Figure 1B) was compared with conventional measurements, where the interaction efficiency is limited by the focus volume of the optical setup in a sample droplet of defined volume 200 μL (Figure 1A). The acquisition time of the Raman spectra was always 120 s for good comparison.

Vibrational Assignment of Normal Modes with Help of Density Functional Theory Calculation. A thorough assignment and interpretation of the normal modes and Raman activities of chloroquine and mefloquine was performed with the help of density functional theory calculations with Gaussian 03.[13] Hybrid exchange correlation functionals provide reliable estimates of experimental frequencies of organic molecules and were therefore applied with Becke's three-parameter exchange functional[14] (B3) as slightly modified by Stephens et al.,[15] coupled with the correlation part of the functional from Perdew and Wang[16] (B3PW91), and triple (6-311+G(d,p)) split valence basis sets of contracted Gaussian functions with polarized and diffuse functions.[17]

■ RESULTS AND DISCUSSION

In this study, a thorough examination is presented of the potential and the various factors in eq 1 that govern the performance of fiber enhanced Raman spectroscopy (FERS) as an analytical tool for ultrasensitive detection of minimal amounts of the important antimalarial drugs chloroquine and mefloquine in the biological relevant aqueous milieu.

Nonresonant Raman Fiber Sensing of the Antimalarials Chloroquine and Mefloquine. In a first step, the fiber enhancement is separated from UV and resonance Raman enhancement in eq 1 by nonresonant excitation with wavelength λ_{exc} = 532 nm (Figure SM1A in the Supporting Information). In doing so, the green laser was coupled through an optical window of a custom-made fiber-adapter assembly (Figure 2) in the Teflon AF hollow core fiber which works as an optical waveguide but also as miniaturized analyte container (Figure 1B). Thus the required sample volume is reduced to 38 μL as compared to conventional measurements (Figure 1A). Because of the application of the fiber-adapter assembly, the

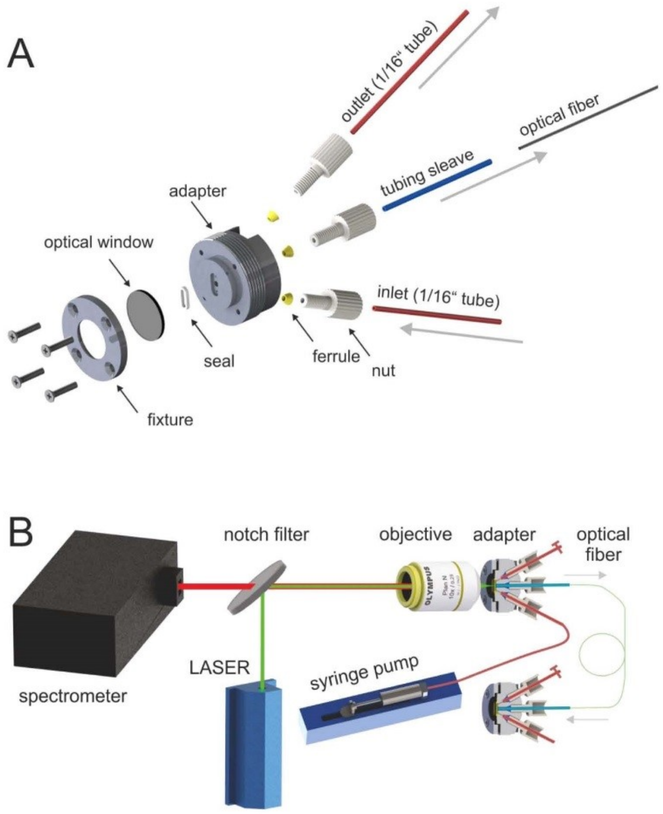

Figure 2. (A) Exploded view of the fiber adapter assembly that was developed for reproducible and quantitative Raman fiber sensing. The assembly provides an optical window for coupling of excitation light into the hollow core fiber and three 10-32 coned ports for tube connectors. The fiber is connected to the middle port by NanoTight tubing sleeves from Upchurch Scientific, which adapt the fiber to a standard o.d. of 1/16 in. The liquid media is filled in from one of the side ports. All tubes consist of poly(ether ether ketone) (PEEK), with excellent mechanical and chemical resistance properties. (B) Schematic view of the fiber sensing setup. The laser light is focused into the fibers with an objective lens, and the backscattered Raman signal is collected by the same objective lens, passes through the notch filter, is dispersed in the spectrometer, and detected with help of a CCD detector. A syringe pump keeps the liquid media flowing through the fiber, such that the analyte passes through the laser focus within a very short time and no photodegradation occurs.

liquid surface of the analyte solution and the optical coupling geometry are perfectly stable. In order to achieve very good long-term reproducibility for precise quantification of the antimalarial drugs, all measured Raman spectra are normalized to the Raman peak of the solvent water at 1645 cm^{-1}. The concentration of the solvent water can be considered as a constant for trace analysis of the pharmaceuticals, and the Raman peaks of the drugs are very close to this reference band ($\Delta\lambda = \sim 2$ nm). Thus the Raman peak of water can be taken as an internal reference[18] and allows us to cancel out all random factors (fluctuations in laser intensity and of the whole optical arrangement, etc.) and to improve the quantitative detection ability.

For sensing of mefloquine (MQ), the most intense peak in the nonresonant Raman spectrum of MQ at 1365 cm^{-1} was chosen.[12b] This Raman band can be assigned to a strong ν(C=C)-stretching and ring breathing vibrations in the quinolone ring[12b] (Figure SM2 in the Supporting Information). The intensities of this Raman peak were compared for a series of concentrations in a conventional droplet measurement (Figure 1A) with the peak intensities of the same MQ solutions in a fiber enhanced Raman experiment (Figure 1B) with identical spectrometer settings. Similarly, the intensities of the Raman peak of chloroquine[12a] at wavenumber position 1557 cm^{-1}, assigned to strong ν(C=C) and ν(C−C) stretching and breathing vibrations in the quinolone ring of CQ[12a] (Figure SM2 in the Supporting Information), were contrasted for a concentration series in conventional droplet sampling and in fiber Raman sensing. The lowest detectable concentrations were derived when the peak heights of the Lorentz-fits of the Raman peaks of MQ and CQ at 1365 cm^{-1} and 1557 cm^{-1} were equal to 3 times the values of the baseline root-mean-square values (Figure 3). In doing so, the limits-of-detection (LOD) of mefloquine and chloroquine in conventional nonresonant Raman sensing were determined as 0.5 μM and 1 μM, respectively. These Raman spectra are illustrated in

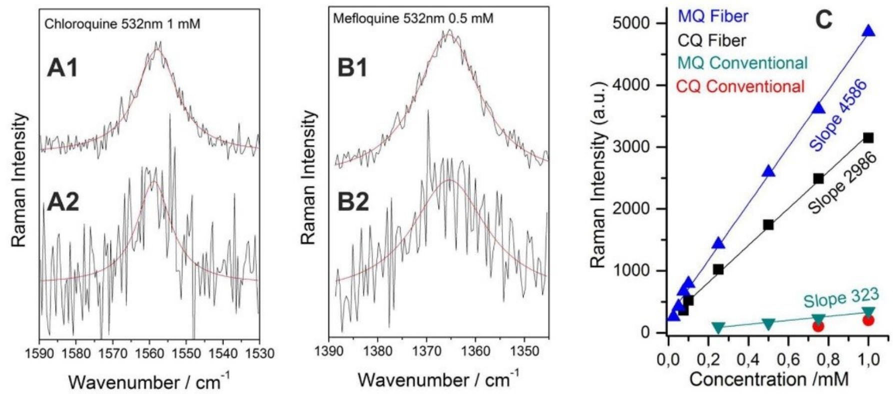

Figure 3. Comparison of conventional (Figure 1A) and fiber enhanced (Figure 1B) nonresonant Raman spectra. The limits of detection in conventional Raman measurements are 1 mM and 0.5 mM for chloroquine and mefloquine, respectively (Figure 3A2,B2). In comparison, the fiber enhanced Raman spectra of chloroquine (Figure 3A1) and mefloquine (Figure 3B1) show much better signal-to-noise ratio at the same concentration. (C) The Raman intensity shows excellent linearity with analyte concentration.

Table 1. Comparison of the Detection Ability of Chloroquine and Mefloquine in the Case of Conventional (Figure 1A), Nonresonant Fiber Enhanced, and UV Resonance Fiber Enhanced (Figure 1B) Raman Spectroscopy[a]

		λ_{exc} = 532 nm nonresonant conventional	λ_{exc} = 532 nm nonresonant fiber-enhanced	λ_{exc} = 257 nm resonant fiber-enhanced		λ_{exc} = 244 nm resonant fiber-enhanced	
MQ	LOD (μM)	500	25	2.5	0.2	5	0.08
CQ	LOD (μM)	1000	75	0.75	0.06	0.5	0.008

[a]Two different UV excitation wavelengths λ_{exc} = 244 nm and λ_{exc} = 257 nm were applied. The analytical limits of detection (LOD) are given in μM. As the applied laser intensities differ significantly ($I_{Laser\ 532}$ = 30mW, $I_{Laser\ 257}$ = 2.4 mW, and $I_{Laser\ 244}$ = 0.5 mW), the first column shows the measured values and an additional second column accounts for the improved detection ability in the case of UV resonance Raman fiber sensing with applied intensity scaling factors.

Figure 3 together with the fiber enhanced Raman spectra of the same solutions of MQ and CQ with identical laser power and spectrometer setting. One can clearly see that the signal-to-noise ratio (SNR) for CQ and MQ is much improved in fiber enhanced Raman sensing (Figure 3A1,B1) as compared to conventional measurements (Figure 3A2,B2). Consequently the LODs for mefloquine and chloroquine are improved in fiber enhanced Raman sensing to 25 μM and 75 μM, respectively (all values are summarized in Table 1).

An excellent linearity between Raman signal intensity and drug concentration can be observed (Figure 3C). The higher sensitivity of fiber enhanced Raman sensing is clearly seen in the steeper slope of the linear fit. With the help of this calibration function, one can measure the Raman signal of an unknown solution of chloroquine and mefloquine and calculate the actual drug concentration. From Figure 3C it is obvious that Raman fiber sensing is capable of measuring very low drug concentrations that are not detectable anymore with conventional Raman measurements.

Fiber-Enhanced UV Resonance Raman Sensing of Chloroquine and Mefloquine. In order to exploit additional enhancement factors according to eq 1, two deep UV excitation wavelengths λ_{exc} = 244 nm and λ_{exc} = 257 nm were applied. The UV−vis absorption spectra of chloroquine (CQ) and mefloquine (MQ) show strong electronic absorptions in the UV spectral range (Figure SM1 in the Supporting Information). Thus one can expect strong enhancement of vibrational bands of CQ that are coupled to these electronic transitions and preresonance enhancement for Raman bands of MQ (Figure SM1 in the Supporting Information). The UV resonance Raman intensity pattern for chloroquine in the wavenumber region 1500 cm^{-1} to 1650 cm^{-1} differs for both excitation wavelengths λ_{exc} = 244 nm and λ_{exc} = 257 nm (Figure SM1 in the Supporting Information). A particularly strong enhancement can be seen for the molecular vibration at 1636 cm^{-1} of CQ for λ_{exc} = 244 nm excitation. These vibrational modes of CQ and MQ in the 1500 cm^{-1} to 1650 cm^{-1} wavenumber region, which are strongly enhanced for the applied UV excitation wavelengths, can be assigned to ν(C═C) stretching vibrations in the quinolone part of the drug molecules (Figure SM2 in the Supporting Information), and are very promising maker bands for the elucidation of chemical $\pi\pi$-stacking interactions of the antimalarials with the biological targets hematin[3] and hemozoin.[2,19]

The combined improvements in the fiber enhanced UV resonance Raman spectra of chloroquine and mefloquine are shown in Figure 4 in comparison with conventional non-resonant Raman spectra (compare Figure 4 with Figure 3). The fiber enhanced UV resonance Raman spectra of the pharmaceutical drugs at 0.1 mM concentration (Figure 4A3,A2,B3,B2) show much better SNR than the conventional Raman spectra of CQ (Figure 4A1) and MQ (Figure 4B1) recorded for 10 times higher concentrations (which is close to the LOD values, see Table 1). Accordingly, the limits-of detection were significantly improved at λ_{exc} = 257 nm to 0.75 μM and 2.5 μM for CQ and MQ, respectively, while excitation with λ_{exc} = 244 nm results in LODs of 0.5 μM for CQ and 5 μM for MQ. As expected from the discussion above, we

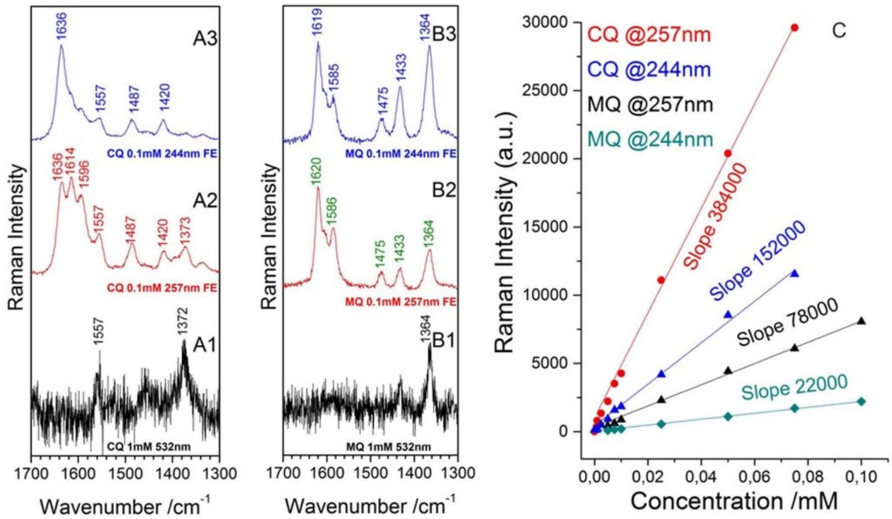

Figure 4. Comparison of conventional nonresonant (Figure 1A) and fiber enhanced UV resonance (Figure 1B) Raman spectra of chloroquine (A) and mefloquine (B). The fiber enhanced UV resonance Raman spectra of CQ (Figure 4A2,A3) and MQ (Figure 4B2,B3) at 0.1 mM concentration show much better signal-to-noise ratio compared to the conventional Raman spectra at 1 mM concentration (Figure 4A1,B1). (C) The Raman intensities show excellent linearity with analyte concentration and thus allow for calibration of the device and quantitative analysis of samples with unknown concentration.

observe a lower detection limit for CQ in comparison to MQ due to the stronger resonance Raman enhancement (Figure SM1 in the Supporting Information).

Furthermore the minimum absolute quantities of pharmaceuticals were calculated that could be detected by means of the applied fiber enhanced UV resonance Raman sensing in the corresponding sampling volumes. For mefloquine, the minimal quantity of molecules that could be detected is 9.5×10^{-11} mol at $\lambda_{\text{exc}} = 257$ nm. The minimum quantity of chloroquine to reach the LOD at $\lambda_{\text{exc}} = 244$ nm was 1.9×10^{-11} mol. All experimental values are summarized in Table 1. As explained above (see Materials and Methods), the intensities of the applied UV lasers were significantly lower ($I_{\lambda=244\text{ nm}} = 0.5$ mW and $I_{\lambda=257\text{ nm}} = 2.4$ mW) as compared to the nonresonant measurements ($I_{\lambda=532\text{ nm}} = 30$ mW). Thus, scaling with according intensity factors was applied (Table 1). The acquired Raman peak intensities of chloroquine and mefloquine show very good linearity with the different drug concentrations for both UV excitation wavelengths (Figure 4C). The linear fits can therefore be taken as calibration functions in order to calculate the analyte quantities of unknown drug samples with the help of the measured Raman peak intensities. Thus it was demonstrated that UV resonance Raman sensing in Teflon AF hollow core fibers is very capable for chemical selective and sensitive analysis of chloroquine and mefloquine and can be exploited for detection of very small sample quantities.

Quantitative Analysis of Fiber Enhanced Resonance Raman Sensing of Absorbing Analytes and Conclusions for Further Improvements. In order to fully understand and exploit additional improvements of the Raman signals by UV and electronic resonant excitation as given by eq 1, it is important to analyze attenuation effects that are introduced by self-absorption of the Raman scattered light by the analytes chloroquine and mefloquine itself. In other words absorbing analytes at high concentration will cause additional optical attenuation and therefore shorten the effective path length of the light in the fiber. Thus it is necessary to balance between this attenuation due to self-absorption and the UV resonance enhancement in case of ultralow-concentration sensing.

First one can expect that the light intensity is not homogeneous along the fiber in the case of UV-resonance Raman spectroscopy. The effective length L_{eff} of the fiber can be calculated by integrating the transmission functions[20] $T_l(z)$ of the laser and $T_r(z)$ of the Raman scattered light along the physical length of the waveguide:

$$L_{\text{eff}} = \int_{L_p}^{0} T_l(z) T_r(z)\, dz \tag{2}$$

$T_l(z)$ describes the ratio of the laser intensity at point z in the fiber to the intensity coupled into the fiber. Similarly, $T_r(z)$ is the ratio of the Raman intensity at the end face of the fiber to the Raman intensity at scattering point z. The transmission functions are assumed to decay exponentially:[20,21]

$$\begin{cases} T_l(z) = e^{-(\mu_{sl} + \varepsilon_l c) z} \\ T_r(z) = e^{-(\mu_{sr} + \varepsilon_r c) z} \end{cases} \tag{3}$$

Herein $\mu_{sl}(\lambda)$ and $\mu_{sr}(\lambda)$ represent the effective scattering loss coefficients that account for waveguide imperfections at the laser and the Raman wavelengths, respectively, while $\varepsilon_l(\lambda)$ and $\varepsilon_r(\lambda)$ account for the analyte extinction coefficients at the wavelengths of the laser and the Raman scattered radiation, and c is the concentration of the sample solution.

As shown in (Figure 2A), there is also a small layer of solution present between the fiber end face and the optical window in the adapter-assembly. This layer is out of focus of the objective lens, thus does not contribute to the collected Raman signal. Though this layer of dead volume is very thin, it will still attenuate the laser and Raman scattered radiation in the case of high concentrations of absorbing analytes:

$$L_{\text{eff}}' = T_{\text{dl}}T_{\text{dr}}\int_{L_{\text{p}}}^{0} T_{\text{l}}(z)T_{\text{r}}(z)\,\text{d}z \tag{4}$$

$$\begin{cases} T_{\text{dl}} = \text{e}^{-(\varepsilon_{\text{l}}cL_{\text{d}})} \\ T_{\text{dr}} = \text{e}^{-(\varepsilon_{\text{r}}cL_{\text{d}})} \end{cases} \tag{5}$$

L_{d} is the thickness of the dead volume and T_{dl} and T_{dr} are the transmissions through the layer of dead volume. Thus the effective length can be expressed as

$$L_{\text{eff}}'(c) = \text{e}^{-(\varepsilon_{\text{l}}cL_{\text{d}})}\,\text{e}^{-(\varepsilon_{\text{r}}cL_{\text{d}})}\frac{1 - \text{e}^{-(\mu_{\text{sl}}+\mu_{\text{sr}}+\varepsilon_{\text{l}}c+\varepsilon_{\text{r}}c)L_{\text{p}}}}{\mu_{\text{sl}} + \mu_{\text{sr}} + \varepsilon_{\text{l}}c + \varepsilon_{\text{r}}c} \tag{6}$$

The intensity $I_{\text{R}}(\tilde{\upsilon},c)$ of a specific Raman peak of the analyte is proportional to the effective fiber length, the laser intensity I_0, the Raman scattering cross section $\sigma(\tilde{\upsilon})$, and the concentration c.

$$I_{\text{R}}(\tilde{\upsilon}, c) = A'I_0\sigma(\tilde{\upsilon})L_{\text{eff}}'(c)c \tag{7}$$

The coefficient A' describes the quality of the optical coupling and the overall performance of the spectroscopic system and it is assumed to be constant in a series of measurements. Combining eqs 6 and 7, the Raman intensity can be expressed as follows:

$$I_{\text{R}}(\tilde{\upsilon}, c) = A'I_0\sigma(\tilde{\upsilon})\,\text{e}^{-((\varepsilon_{\text{l}}+\varepsilon_{\text{r}})\cdot cL_{\text{d}})}\frac{1 - \text{e}^{-(\mu_{\text{sl}}+\mu_{\text{sr}}+(\varepsilon_{\text{l}}+\varepsilon_{\text{r}})c)L_{\text{p}}}}{\mu_{\text{sl}} + \mu_{\text{sr}} + (\varepsilon_{\text{l}} + \varepsilon_{\text{r}})c}c \tag{8}$$

Equation 8 can be simplified to the function (eq 9) with the parameters A, B, and C and the constants L_{d} and L_{p}.

$$\begin{gathered} x = c; \quad y = I_{\text{R}}(\tilde{\upsilon}, x); \quad A = A'I_0\sigma(\tilde{\upsilon}); \quad B = \varepsilon_{\text{l}} + \varepsilon_{\text{r}}; \\ C = \mu_{\text{sl}} + \mu_{\text{sr}}; \quad L_{\text{d}} = 1\text{ mm}; \quad L_{\text{p}} = 430\text{ mm}; \\ y = A\,\text{e}^{-(BxL_{\text{d}})}\frac{1 - \text{e}^{-(C+Bx)L_{\text{p}}}}{C + Bx}x \end{gathered} \tag{9}$$

According to eq 9, one can see that the Raman intensity $I_{\text{R}}(\tilde{\upsilon},c)$ will be strongly enhanced by improvements of parameters A and C and that the influence of attenuation B by the analyte will be small in the case of low concentration measurements.

The peak intensities of the experimentally derived fiber enhanced UV resonance Raman spectra of chloroquine and mefloquine fit well to eq 9 (Figure 5). For low concentration, the peak intensities grow linearly with concentrations (Figures 4C and 5). However, in a high concentration range, one can observe a decrease of the peak intensities with the increasing analyte concentration (Figure 5). From Figure 5 one can conclude that fiber enhanced UV resonance Raman spectroscopy is advantageous for detection of chloroquine and mefloquine at concentrations below 100 μM (which is the measurement range for ultrasensitive drug detection) as the effective length is long and the fiber improves the sensitivity of the measurement. For very low concentrations, the Raman intensity of CQ, excited with λ_{exc} = 244 nm, shows the steepest gradient and strongest enhancement in agreement with our previous findings (Table 1).

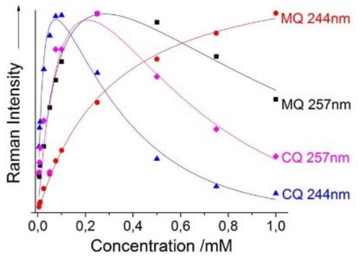

Figure 5. Nonlinear fitting of the experimentally acquired fiber enhanced Raman peak intensities $I_{\text{R}}(c)$ of chloroquine and mefloquine (at λ_{exc} = 244 nm and λ_{exc} = 257 nm, respectively), with the help of eq 9. The peak intensities can be approximated as a linear function of the analyte concentration in the range of trace detection (c < 50 nM).

According to eq 9, the function of the Raman intensity $I_{\text{R}}(\tilde{\upsilon},c)$ is defined by five factors: A, B, C, L_{d}, and L_{p}. The thickness of the thin layer of dead volume L_{d} and the physical fiber length L_{p} are constant for all experiments (see the section Materials and Methods). Factor A comprises the intensity of the excitation laser, the quality of the optical coupling, and the overall system performance. Factor B will become larger when stronger absorbing samples are involved, and parameter C describes the waveguiding quality of the fiber. A thorough discussion of these five factors (A, B, C, L_{d}, and L_{p}) helps to draw conclusions on how to improve the performance of this promising analytical technique for future developments. The interdependencies of these parameters and their influences on the Raman intensity are shown in Figure 6.

According to eq 9, the Raman intensity I_{R} is linearly dependent on factor A. Parameter A is given by $A = A'I_0\sigma(\tilde{\upsilon})$ and can be improved by stronger laser intensities and for molecules with larger Raman scattering cross sections. Further enhancement of the acquired Raman intensity can be achieved by an overall improvement of the spectroscopic system (better optical components, sensitive detector, etc.) as well as better optical fiber coupling. Figure 6,1 demonstrates the additional improvements one can gain by an improvement of factor A, based on the values for chloroquine for λ_{exc} = 244 nm excitation (A = 12 340, B = 3252, and C = 0.107).

Factor C in eq 9 is a very important parameter describing the quality and light guiding ability of the optical fiber. For improved analytical sensitivity, the optical fiber should accept excitation light with a high numerical aperture; guide the light along extended path lengths, such that a large number of molecules are excited; and collect the Raman scattered light with high numerical aperture and guide the Raman light with minimal attenuation to the collection optic. As shown in Figure 6,2, an improvement of the optical fiber can strongly enhance the Raman signal. Obviously the guiding ability of the TeflonAF hollow core fiber is relatively poor, both in terms of numerical aperture and strong attenuation due to the inner surface roughness. For instance, particles and micro gas bubbles that adhere to the inner wall of the Teflon hollow core fiber can raise losses by scattering the light. Therefore, a proper cleaning procedure is essential for maintenance of good fiber enhancement in Teflon capillaries. Thus one can imagine high potential

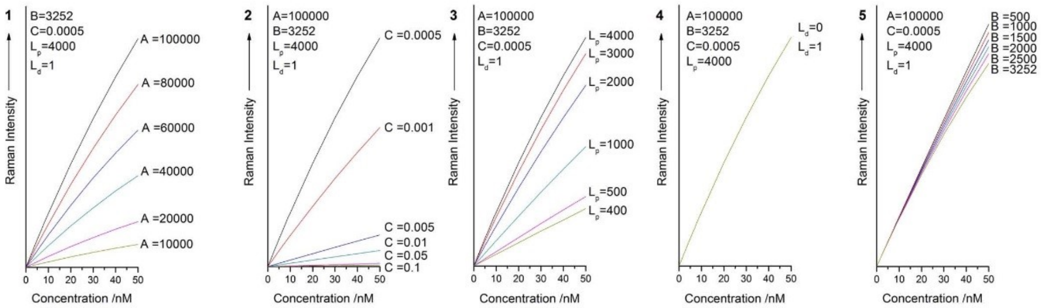

Figure 6. Analysis of the different parameters A, B, C, L_d, and L_p that govern the Raman intensity $I_R(c)$ in fiber enhanced sensing and their interdependencies, according to eq 9. These simulations allow estimations how to increase the performance of Raman fiber sensing with improved parameters. (1) Parameter A rises with stronger laser intensity, molecules with higher Raman scattering cross section, and an overall improvement of the optical coupling and sensing system. Thus $I_R(c)$ will increase linearly with the rise of A. (2) The quality and light guiding ability of the optical fiber has a significant effect on the Raman intensity. Improvements of the optical quality will also allow one to exploit increasing lengths of the fiber. (3) In the case of good optical quality and low analyte concentration, an increase of the physical fiber length will considerably enhance the Raman signal. The impact of the optimal fiber length saturates in the case of backscattering geometry. (4) The thickness of the dead volume decreases the Raman signals at high concentrations and has a negligible effect for trace analysis. (5) The analyte absorption attenuates the light transmission but only occurs as product with the concentration, thus it will not have strong effect for low concentrations.

for the analytical performance in the improvement of the optical fiber, which is in the focus of our current efforts.

The physical fiber length L_p appears in eq 9 as the exponential factor in product with parameters Bx and C. Thus for sensing in an ultralow concentration range and under application of high-quality optical waveguides, a sufficient physical length of the fiber will increase the number of molecules that efficiently contribute to the Raman intensity (Figure 6,3). The impact of L_p saturates for optimal lengths in the case of backscattering geometry.

The thickness L_d of the layer of dead volume in the fiber adapter assembly (Figure 2A) attenuates the Raman intensity for higher concentrated absorbing analytes. Thus the Raman intensity decreases with increasing analyte concentration. This happened in the performed experiments for CQ at λ_{exc} = 244 nm above 100 μM, for CQ at λ_{exc} = 257 nm above 200 μM, and MQ at λ_{exc} = 257 nm above 250 μM (see Figure 5). In an ideal case where the thickness of the dead volume is negligible, the Raman intensity will saturate for high concentrations. However, the dead volume has very little influence in the range of ultralow concentration measurements, which are the main interest of this work (Figure 6,4).

As explained above, with growth of factor B at higher analyte absorption, the physical length of the fiber that contributes to the signal enhancement shortens and the sensitivity is decreasing. However, factor B appears together with the analyte concentration and does not play a major role for ultrasensitive detection (Figure 6,5).

Thus, some additional efforts will be worth pursuing especially for an improvement of parameters A and C in eq 9 in order to improve this promising analytical technique. On the basis of eq 9, one can calculate (with parameters A = 100 000, B = 3 252, C = 0.0005, L_p = 4000, L_d = 1, and I_{Laser} = 30 mW at λ_{exc} = 244 nm) and predict a highly improved limit of detection of chloroquine of only 1.7 pM.

■ CONCLUSION

Fiber enhanced UV resonance Raman sensing was demonstrated to be an extremely capable technique for ultrasensitive, chemical selective analysis of drugs in aqueous media. A robust experimental setup was designed for reproducible and quantitative Raman sensing in hollow core optical fibers. Fiber enhanced Raman spectra of the two antimalaria drugs chloroquine and mefloquine showed much better signal-to-noise ratios as compared to conventional sampling. Accordingly, the concentration limit of detection was improved by an overall factor of 1.25 × 10^5 for chloroquine and 6.25 × 10^3 for mefloquine with the help of fiber enhanced UV resonance Raman sensing. As the hollow core of the fiber was exploited as a minimized sample container, the performance of the fiber as an optical waveguide was thoroughly analyzed in the case of absorbing samples. It was shown that the ability of fiber enhanced Raman spectroscopy (FERS) can be significantly improved, and a detection limit of picomolar concentration could be reached for the important antimalarial active agent chloroquine. Considering the potential of UV-resonance Raman spectroscopy for bioanalysis,[11] UV-FERS has high potential as an ultrasensitive chemical sensing technique for a wide range of biomolecules and can be exploited, e.g., for detection of minimal quantities of rare and expensive pharmaceuticals.

■ ASSOCIATED CONTENT

Ⓢ Supporting Information

Additional information as noted in text. This material is available free of charge via the Internet at http://pubs.acs.org.

■ AUTHOR INFORMATION

Corresponding Author

*E-mail: torsten.frosch@uni-jena.de.

Author Contributions

‖T.F. and D.Y. contributed equally to this work.

Notes

The authors declare no competing financial interest.

■ ACKNOWLEDGMENTS

Funding from the federal state of Thuringia (Forschergruppe Fasersensorik and FaserINFRA) and ESF is highly acknowledged. We thank the colleagues from our workshop for their help in the realization of the fiber adapter assembly.

■ REFERENCES

(1) (a) *World Malaria Report: 2011*; WHO Press, World Health Organization: Switzerland, 2011. (b) Ridley, R. G. *Nature* **2002**, *415*, 686−693.

(2) Pagola, S.; Stephens, P. W.; Bohle, D. S.; Kosar, A. D.; Madsen, S. K. *Nature* **2000**, *404*, 307−310.

(3) (a) Frosch, T.; Meyer, T.; Schmitt, M.; Popp, J. *Anal. Chem.* **2007**, *79*, 6159−6166. (b) Frosch, T.; Kustner, B.; Schlucker, S.; Szeghalmi, A.; Schmitt, M.; Kiefer, W.; Popp, J. *J. Raman Spectrosc.* **2004**, *35*, 819−821.

(4) (a) Peyton, D. H. *Curr. Top. Med. Chem.* **2012**, *12*, 400−407. (b) Hastings, I. M.; Bray, P. G.; Ward, S. A. *Science* **2002**, *298*, 74−75. (c) Wellems, T. E. *Science* **2002**, *298*, 124−126.

(5) (a) Frosch, T.; Koncarevic, S.; Becker, K.; Popp, J. *Analyst* **2009**, *134*, 1126−1132. (b) Frosch, T.; Popp, J. *J. Biomed. Opt.* **2010**, *15*, 041516. (c) Frosch, T.; Schmitt, M.; Schenzel, K.; Faber, J. H.; Bringmann, G.; Kiefer, W.; Popp, J. *Biopolymers* **2006**, *82*, 295−300. (d) Frosch, T.; Popp, J. *J. Mol. Struct.* **2009**, *924−926*, 301−308. (e) Frosch, T.; Meyer, T.; Schmitt, M.; Popp, J. *Anal. Chem.* **2007**, *79*, 6159−6166.

(6) (a) Frosch, T.; Schmitt, M.; Noll, T.; Bringmann, G.; Schenzel, K.; Popp, J. *Anal. Chem.* **2007**, *79*, 986−993. (b) Frosch, T.; Schmitt, M.; Popp, J. *J. Phys. Chem. B* **2007**, *111*, 4171−4177. (c) Frosch, T.; Tarcea, N.; Schmitt, M.; Thiele, H.; Langenhorst, F.; Popp, J. *Anal. Chem.* **2007**, *79*, 1101−1108. (d) Frosch, T.; Keiner, R.; Michalzik, B.; Fischer, B.; Popp, J. *Anal. Chem.* **2013**, *85*, 1295−1299.

(7) Yang, M. K.; French, R. H.; Tokarsky, E. W. *J. Micro/Nanolithogr., MEMS and MOEMS* **2008**, *7*, 033010.

(8) (a) Pelletier, M. J.; Altkorn, R. *Anal. Chem.* **2001**, *73*, 1393−1397. (b) Altkorn, R.; Koev, I.; Pelletier, M. J. *Appl. Spectrosc.* **1999**, *53*, 1169−1176. (c) Altkorn, R.; Malinsky, M. D.; Van Duyne, R. P.; Koev, I. *Appl. Spectrosc.* **2001**, *55*, 373−381. (d) Qi, D.; Berger, A. J. *J. Biomed. Opt.* **2005**, *10*, 031115. (e) Qi, D.; Berger, A. J. *Appl. Spectrosc.* **2004**, *58*, 1165−1171.

(9) (a) Dijkstra, R. J.; Slooten, C. J.; Stortelder, A.; Buijs, J. B.; Ariese, F.; Brinkman, U. A. T.; Gooijer, C. *J. Chromatogr., A* **2001**, *918*, 25−36. (b) Marquardt, B. J.; Vahey, P. G.; Synovec, R. E.; Burgess, L. W. *Anal. Chem.* **1999**, *71*, 4808−4814.

(10) Qi, D. H.; Berger, A. J. *Appl. Opt.* **2006**, *45*, 489−494.

(11) (a) Asher, S. A.; Ludwig, M.; Johnson, C. R. *J. Am. Chem. Soc.* **1986**, *108*, 3186−3197. (b) DeVito, V. L.; Asher, S. A. *J. Am. Chem. Soc.* **1989**, *111*, 9143−9152. (c) Rodgers, K. R.; Spiro, T. G. *Science* **1994**, *265*, 1697−1699. (d) Jayaraman, V.; Rodgers, K. R.; Mukerji, I.; Spiro, T. G. *Science* **1995**, *269*, 1843−1848. (e) Xue, Y.; Davis, A. V.; Balakrishnan, G.; Stasser, J. P.; Staehlin, B. M.; Focia, P.; Spiro, T. G.; Penner-Hahn, J. E.; O'Halloran, T. V. *Nat. Chem. Biol.* **2008**, *4*, 107−109.

(12) (a) Frosch, T.; Schmitt, M.; Bringmann, G.; Kiefer, W.; Popp, J. *J. Phys. Chem. B* **2007**, *111*, 1815−1822. (b) Frosch, T.; Schmitt, M.; Popp, J. *Anal. Bioanal. Chem.* **2007**, *387*, 1749−1757.

(13) Frisch, M. J.; Trucks, G. W.; Schlegel, H. B.; Scuseria, G. E.; Robb, M. A.; Cheeseman, J. R.; Montgomery, J. A., Jr.; Vreven, T.; Kudin, K. N.; Burant, J. C.; Millam, J. M.; Iyengar, S. S.; Tomasi, J.; Barone, V.; Mennucci, B.; Cossi, M.; Scalmani, G.; Rega, N.; Petersson, G. A.; Nakatsuji, H.; Hada, M.; Ehara, M.; Toyota, K.; Fukuda, R.; Hasegawa, J.; Ishida, M.; Nakajima, T.; Honda, Y.; Kitao, O.; Nakai, H.; Klene, M.; Li, X.; Knox, J. E.; Hratchian, H. P.; Cross, J. B.; Bakken, V.; Adamo, C.; Jaramillo, J.; Gomperts, R.; Stratmann, R. E.; Yazyev, O.; Austin, A. J.; Cammi, R.; Pomelli, C.; Ochterski, J. W.; Ayala, P. Y.; Morokuma, K.; Voth, G. A.; Salvador, P.; Dannenberg, J. J.; Zakrzewski, V. G.; Dapprich, S.; Daniels, A. D.; Strain, M. C.; Farkas, O.; Malick, D. K.; Rabuck, A. D.; Raghavachari, K.; Foresman, J. B.; Ortiz, J. V.; Cui, Q.; Baboul, A. G.; Clifford, S.; Cioslowski, J.; Stefanov, B. B.; Liu, G.; Liashenko, A.; Piskorz, P.; Komaromi, I.; Martin, R. L.; Fox, D. J.; Keith, T.; Al-Laham, M. A., Peng, C. Y.; Nanayakkara, A.; Challacombe, M.; Gill, P. M. W.; Johnson, B.; Chen, W.; Wong, M. W.; Gonzalez, C.; Pople, J. A. *Gaussian 03*, revision C.02; Gaussian, Inc.: Wallingford, CT, 2004.

(14) Becke, A. D. *J. Chem. Phys.* **1992**, *97*, 9173−9177.

(15) Stephens, P. J.; Devlin, F. J.; Chabalowski, C. F.; Frisch, M. J. *J. Phys. Chem.* **1994**, *98*, 11623−11627.

(16) (a) Perdew, J. P.; Wang, Y. *Phys. Rev. B* **1992**, *45*, 13244−13249. (b) Perdew, J. P.; Chevary, J. A.; Vosko, S. H.; Jackson, K. A.; Pederson, M. R.; Singh, D. J.; Fiolhais, C. *Phys. Rev. B* **1992**, *46*, 6671−6687.

(17) Pople, J. A.; Schlegel, H. B.; Krishnan, R.; Defrees, D. J.; Binkley, J. S.; Frisch, M. J.; Whiteside, R. A.; Hout, R. F.; Hehre, W. J. *Int. J. Quantum Chem.* **1981**, 269−278.

(18) Chi, Z. H.; Chen, X. G.; Holtz, J. S. W.; Asher, S. A. *Biochemistry* **1998**, *37*, 2854−2864.

(19) Frosch, T.; Konearevic, S.; Zedler, L.; Schmitt, M.; Schenzel, K.; Becker, K.; Popp, J. *J. Phys. Chem. B* **2007**, *111*, 11047−11056.

(20) Vickers, T. J.; Mann, C. K.; Zhu, J. X.; Chan, K. C. *Appl. Spectrosc. Rev.* **1991**, *26*, 341−375.

(21) (a) Strekas, T. C.; Adams, D. H.; Packer, A.; Spiro, T. G. *Appl. Spectrosc.* **1974**, *28*, 324−327. (b) Ludwig, M.; Asher, S. A. *Appl. Spectrosc.* **1988**, *42*, 1458−1466.

7.2. Fiber-enhanced Raman spectroscopic analysis as a novel method for diagnosis and monitoring of diseases related to hyperbilirubinemia and hyperbiliverdinemia

Reproduced from Yan, D.; Domes, C.; Domes, R.; Frosch, T.; Popp, J.; Pletz, M. W.; Frosch, T., Fiber-enhanced Raman spectroscopic analysis as a novel method for diagnosis and monitoring of diseases related to hyperbilirubinemia and hyperbiliverdinemia. Analyst 2016, 141 (21), 6104-6115. with permission from Royal Society of Chemistry.

Analyst

ROYAL SOCIETY OF CHEMISTRY

PAPER

View Article Online
View Journal | View Issue

CrossMark
click for updates

Cite this: *Analyst*, 2016, **141**, 6104

Fiber enhanced Raman spectroscopic analysis as a novel method for diagnosis and monitoring of diseases related to hyperbilirubinemia and hyperbiliverdinemia†

Di Yan,[a] Christian Domes,[a] Robert Domes,[a] Timea Frosch,[a] Jürgen Popp,[a,c,d]
Mathias W. Pletz[b] and Torsten Frosch*[a,c,d]

Fiber enhanced resonance Raman spectroscopy (FERS) is introduced for chemically selective and ultrasensitive analysis of the biomolecules hematin, hemoglobin, biliverdin, and bilirubin. The abilities for analyzing whole intact, oxygenated erythrocytes are proven, demonstrating the potential for the diagnosis of red blood cell related diseases, such as different types of anemia and hemolytic disorders. The optical fiber enables an efficient light-guiding within a miniaturized sample volume of only a few micro-liters and provides a tremendously improved analytical sensitivity (LODs of 0.5 μM for bilirubin and 0.13 μM for biliverdin with proposed improvements down to the pico-molar range). FERS is a less invasive method than the standard ones and could be a new analytical method for monitoring neonatal jaundice, allowing a precise control of the unconjugated serum bilirubin levels, and therefore, providing a better prognosis for newborns. The potential for sensing very low concentrations of the bile pigments may also open up new opportunities for cancer research. The abilities of FERS as a diagnostic tool are explored for the elucidation of jaundice with different etiologies including the rare, not yet well understood diseases manifested in green jaundice. This is demonstrated by quantifying clinically relevant concentrations of bilirubin and biliverdin simultaneously in the micro-molar range: for the case of hyperbilirubinemia due to malignancy, infectious hepatitis, cirrhosis or stenosis of the common bile duct (1 μM biliverdin together with 50 μM bilirubin) and for hyperbiliverdinemia (25 μM biliverdin and 75 μM bilirubin). FERS has high potential as an ultrasensitive analytical technique for a wide range of biomolecules and in various life-science applications.

Received 23rd July 2016,
Accepted 20th August 2016

DOI: 10.1039/c6an01670g

www.rsc.org/analyst

Introduction

Heme chromophores are iron protoporphyrin IX complexes and fulfil essential roles in several regulating processes in biological systems. They serve for instance as catalytically active centers of different important cytochrome enzymes, which have important functions in biochemical processes, among others in the brain,[1] and represent the prosthetic group of hemoglobin, the transporter of respiratory gases (O_2, CO_2, CO) in erythrocytes.[2] Therefore, monitoring of the oxygenation state of the red blood cells can be very helpful for the differential diagnosis of different types of anemia and hemolytic disorders. Heme and hemozoin are also key drug-targets in blood disorders and diseases, such as malaria.[3] In the blood recycling process, the aged red blood cells are degraded into their components, heme and globin. The heme group is enzymatically converted to biliverdin (BV) and bilirubin (BR),[4] which can be eliminated *via* bile after biotransformation (conjugation) in the liver (Fig. 1). When the activity of one of the participating enzymes is defect or totally absent, this detoxification process is perturbed and several diseases might occur.[5]

An increased level of bilirubin above normal, so called hyperbilirubinemia, is shown to be toxic and in most cases manifests in jaundice,[6] a yellow tint of the skin and sclera. The toxicity of hyperbilirubinemia is especially important in neonates due to incomplete formation of the blood–brain barrier,[7] in which case the circulating unconjugated excess bilirubin may pose a threat to the infant by entering the central nervous system and thereby causing irreversible neurological damage by developing kernicterus or bilirubin-encephalopathy.[8] About 60% of healthy, term neonates present detectable jaundice[9]

---

[a] *Leibniz Institute of Photonic Technology, Jena, Germany*
[b] *University Hospital, Center for Infectious Diseases and Infection Control, Jena, Germany*
[c] *Friedrich Schiller University, Institute for Physical Chemistry, Jena, Germany*
[d] *Friedrich Schiller University, Abbe Centre of Photonics, Jena, Germany.*
E-mail: torsten.frosch@uni-jena.de, torsten.frosch@gmx.de

† Electronic supplementary information (ESI) available. See DOI: 10.1039/c6an01670g

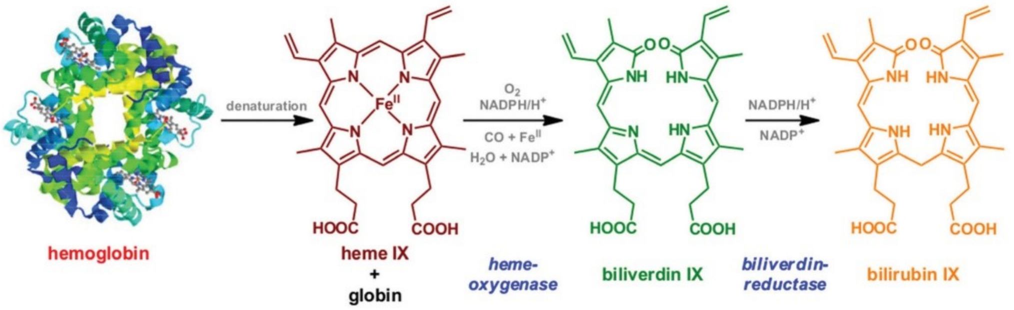

Fig. 1 Scheme of the metabolism of hemoglobin by various enzymes. The first step is the denaturation of hemoglobin tetramer by phagocytes to heme IX and globin chains. In the reticular connective tissue, the heme chromophore is enzymatically oxidized by *heme oxygenase* in presence of oxygen to the green bile pigment biliverdin IX. Due to the effect of the enzyme *biliverdin reductase* this pigment is reduced to its orange degradation product, bilirubin IX.

and even low elevations of the bilirubin level can manifest in an increased incidence of neurological abnormalities or decreased development of intellectual performance later in life.[10] Early discharged babies may only present jaundice at extremely high serum bilirubin concentrations.[11]

For ensuring a better prognosis, an earlier diagnosis of mild hyperbilirubinemia is needed, before the manifestation of jaundice. Thus, an extremely sensitive method is required for rapid monitoring of the serum bilirubin level. This technique should also be minimally invasive and require only minimal blood sample volume for quantification.

Moreover, an elevation of the bilirubin serum level from 17 μM up to 340 μM (ref. 10) was also observed in the inheritable disorders Gilbert[5c] and Crigler–Najjar syndrome.[5d] Therefore, the detection of these elevations could be very helpful as an early diagnostic indicator before genetical investigations.

Hyperbiliverdinemia, defined as elevated level of biliverdin above the normal range, is another type of jaundice, so called green jaundice.[12] Normal biliverdin levels in serum are reported as 0.9–6.5 μM and strongly correlate to the total bilirubin concentration,[13] whereas green jaundice manifests in a rise of the serum level of bilirubin above 25 μM together with an elevation of biliverdin level above 75 μM.[13] This symptom occurs in several syndromes and diseases.[13,14] The serum biliverdin concentration is found by patients diagnosed with malignancy, infectious hepatitis, cirrhosis or stenosis of the common bile duct jaundice to be in the range from one to ten percentage of the total bilirubin level.[14b] On the other hand, the absence of hyperbiliverdinemia is an indication against the diagnosis of jaundice due to neoplastic obstruction.[12] Thus, being able to simultaneously quantify slight elevations of bilirubin and biliverdin levels would be tremendously helpful for the diagnosis of the cause of jaundice.

Additionally, in the past two decades, medical scientists have discovered beneficial properties of the bile pigments. They play an important role as anti-oxidative[15] and anti-mutagenic agents[16] at slightly elevated biliverdin level of 15 μM.[16b] Also an HIV-protease inhibiting activity above the concentration of 10 μM is assigned to the bile pigments.[17] At the concentration of 25 μM, bilirubin induces apoptosis significantly in human gastric adenocarcinoma cell lines[18] and also in colon cancer cells.[19] The presence of 15 μM biliverdin successfully inhibits the mutations in mammalian cell systems.[20] These beneficial properties of the bile pigments are also reflected in clinical studies. An increase of the bilirubin level by 1.7 μM is correlated with 8% reduction of the incidence rate of lung cancer and with 6% reduction of the rate of chronic obstructive pulmonary disease.[15a]

Therefore, the simultaneous detection of minor concentration changes (micro-molar and lower concentrations) of biliverdin and bilirubin is urgently needed for the earlier diagnosis and monitoring of diseases, such as malignancy, infectious hepatitis, cirrhosis, and stenosis of the common bile duct jaundice as well as for neonatal jaundice, and also for the elucidation of important processes in cancer research.

Several methods have been developed for the analysis of bilirubin in clinical samples. The most commonly used ones are the diazo reaction[21] and the direct spectrophotometry.[22] These techniques are highly dependent on the pH-value or have interference with other heme containing proteins, and both are very time-consuming. Therefore, there is a need of extremely sensitive method for rapid monitoring the serum bilirubin level. In the last few decades the trend goes to other analytical methods like photochemical[23] or electrochemical sensors[24] and chromatography[25] which are used for the detection of bilirubin in human serum. Since there are no investigations of the biliverdin and bilirubin level in terms of the analysis of jaundice and other diseases *via* fiber enhanced Raman spectroscopy (FERS), this paper should demonstrate the potential of this technique as a tool for sensitive and chemical selective analysis of these two bile pigments together in clinically relevant concentrations. The advantage here is the minimally invasiveness and the need of minimal sample volumes for their simultaneous quantification. None of the other methods incorporate these characteristics altogether. In fiber enhanced Raman spectroscopy, the signal intensity is significantly increased by exciting and collecting the Raman signal of the liquid sample along an extended path length within the fiber hollow core with remarkable efficiency. Excellent results have been achieved in the analysis of low concentrated analytes in aqueous solutions.[26]

Materials and methods

Sample preparation

Hemin (chloroferriprotoporphyrin IX, ≥98.0%), human lyophilized hemoglobin, bilirubin (95%), biliverdin-hydrochloride (97%), and phosphate buffered saline were purchased from Sigma-Aldrich and used without further purification (Fig. 2). An ultra-clear water feed system from SG Water GmbH was employed to produce ultrapure deionized water (conductivity lower than 0.056 µS cm^{-1}). Hematin solutions (pH 7) were prepared by dissolving hemin in 0.1 M NaOH and then diluted with deionized water to various concentrations. Hemoglobin, bilirubin and biliverdin were buffered at pH 7.4 in all concentrations. Erythrocytes were separated from human blood. The human blood was centrifuged at 3000 rpm for 10 min. Then the upper part of the solution was removed from the tube, and phosphate buffered saline (PBS: 10 mM PO_4^{3-}, 137 mM NaCl, 1.8 mM KH_2PO_4, and 2.7 mM KCl) was refilled into the tube. This procedure was repeated three times. Then the erythrocytes were diluted 1 : 199 with PBS (pH 7.4). All samples were kept in the dark at 4 °C until use.

Fiber enhanced Raman spectroscopy

Raman spectra were obtained with a LabRam HR system with excitation wavelengths λ = 532 nm (I_{laser} = 10 mW at the sample), λ = 413 nm (I_{laser} = 7 mW at the sample), λ = 752 nm (I_{laser} = 350 mW at the sample) and λ = 364 nm (I_{laser} = 3.5 mW at the sample). A 10× objective lens (Olympus) and a 15× objective lens (OFR) were used for the measurements in the visible and UV ranges, respectively. The optical hollow core fiber had a length of 40 cm, an inner diameter of 168 µm and an internal volume of 9 µL. In order to keep a stable optical coupling situation for quantitative and reproducible Raman sensing, a custom-made fiber adapter which provides an optical window for laser coupling into the fiber was also developed[27] (Fig. 3). In order to avoid photo-degradation of the absorbing analytes during the measurements, the samples were kept streaming at 40 µL s^{-1} flow rate with the help of a syringe pump. Thus, the velocity of liquids in the fiber was about 1.8 m s^{-1} and the samples passed through the laser focus within a short time and were not damaged by the laser radiation. All spectra were taken with 120 s exposure time, and the performance of FERS was compared with conventional cuvette measurements with identical experimental parameters (cuvette volume 200 µL).

The Raman spectra of the solutions contained a background signal contributed by the solvent. In order to achieve reproducibility for precise quantification, the measured Raman spectra were normalized to the Raman band of the solvent water at 1645 cm^{-1} and/or the band of the phosphate buffer at approximately 990 cm^{-1}. As the analyte concentrations were extremely low, the quantity of the solvent could be considered as constant in all solutions. Thus, the Raman peak of water and/or the signal of the buffer was utilized as an internal standard[27,28] to cancel out all random factors (fluctuations in laser intensity and optical coupling, *etc.*) and to improve the quantitative detection ability. The signal-to-noise ratio (SNR) was calculated from the height of the Lorenzian fit of the target peaks and the root-mean-square (RMS) values of

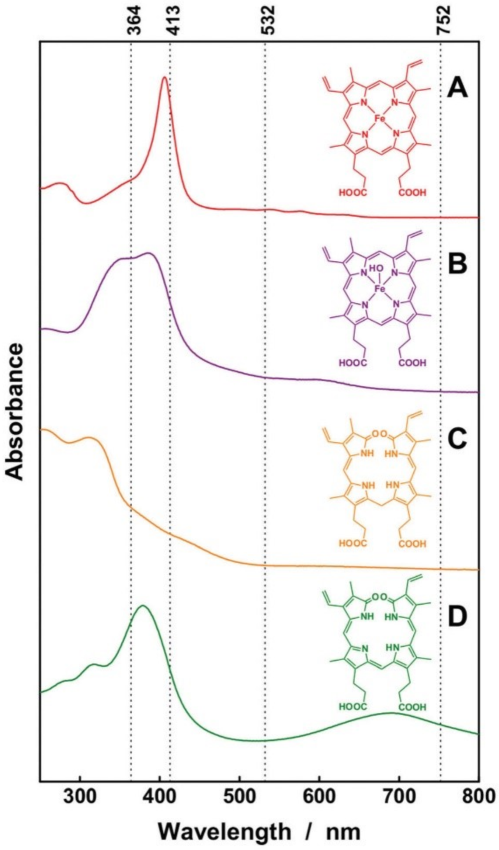

Fig. 2 Schematic chemical structures and absorption spectra in aqueous solution of the heme chromophores: chemical structures of hemoglobin (A), hematin (B), bilirubin (C) and biliverdin (D), respectively. The simplified heme structure represents the chromophoric unit of hemoglobin. The applied laser excitation wavelengths $\lambda_{exc.}$ = 364 nm, $\lambda_{exc.}$ = 413 nm, $\lambda_{exc.}$ = 532 nm, and $\lambda_{exc.}$ = 752 nm are depicted as vertical dashed lines. These selected excitation wavelengths can be carefully tuned into the electronic absorption bands of the individual chromophores and strong resonance Raman enhancements can be achieved for the vibrational modes that are coupled to these electronic transitions.

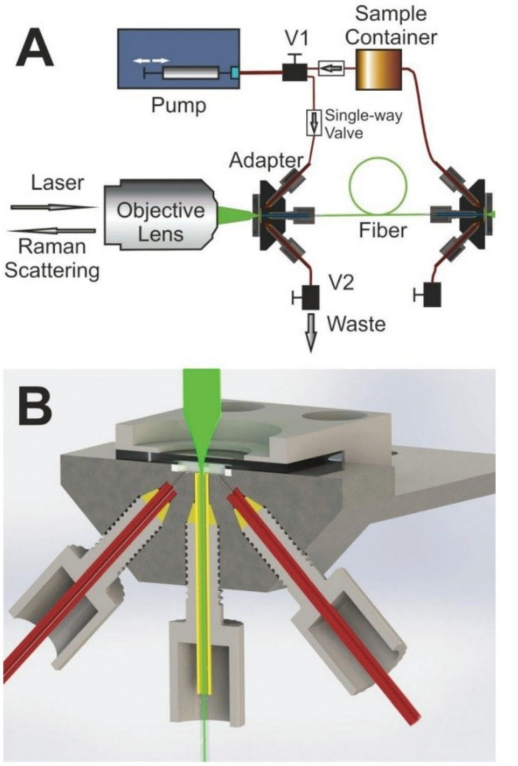

Fig. 3 A: Scheme of the fiber enhanced Raman spectroscopic (FERS) setup, consisting of laser, objective lens, fiber with adapter assembly, pump, and spectrometer. B: Detail of the fiber adapter assembly. The laser light is coupled through an optical window into the fiber hollow core and the analyte solution is pumped through the hollow core by side connectors.

the baseline. The lowest detectable concentrations were derived when the SNR was equal to three.

Estimating the potential of FERS for ultrasensitive analysis

The attenuation that is introduced by the samples and the fiber were thoroughly discussed.[27] The back scattered Raman intensity in an absorbing liquid core fiber can be expressed as following:

$$I_{\mathrm{R}}(\tilde{\nu},c) = A'\cdot I_0\cdot\sigma(\tilde{\nu})\cdot e^{-((\varepsilon_{\mathrm{l}}+\varepsilon_{\mathrm{r}})\cdot c\cdot L_{\mathrm{d}})}\cdot\frac{1-e^{-(\mu_{\mathrm{sl}}+\mu_{\mathrm{sr}}+(\varepsilon_{\mathrm{l}}+\varepsilon_{\mathrm{r}})\cdot c)\cdot L_{\mathrm{p}}}}{\mu_{\mathrm{sl}}+\mu_{\mathrm{sr}}+(\varepsilon_{\mathrm{l}}+\varepsilon_{\mathrm{r}})\cdot c}\cdot c \qquad (1)$$

In this equation, A' represents the efficiency of the instrument, I_0 the laser intensity, $\sigma(\tilde{\nu})$ the Raman scattering cross section, c the analyte concentration, $\mu_{\mathrm{sl}}(\lambda)$ and $\mu_{\mathrm{sr}}(\lambda)$ the effective scattering loss coefficients that account for waveguide imperfections at the laser and the Raman wavelengths, while $\varepsilon_{\mathrm{l}}(\lambda)$ and $\varepsilon_{\mathrm{r}}(\lambda)$ account for the analyte extinction coefficients at the wavelengths of the laser and the Raman scattered radiation.[27] Eqn (1) can be simplified to a function (2) of concentration with the parameters A, B, C and the constants L_{d} and L_{p}.[27]

$x = c$; $y = I_{\mathrm{R}}(\tilde{\nu},x)$; $A = A'\cdot I_0\cdot\sigma(\tilde{\nu})$; $B = \varepsilon_{\mathrm{l}} + \varepsilon_{\mathrm{r}}$; $C = \mu_{\mathrm{sl}} + \mu_{\mathrm{sr}}$; $L_{\mathrm{d}} = 1$ mm; $L_{\mathrm{p}} = 400$ mm.

$$y = A\cdot e^{-(B\cdot x\cdot L_{\mathrm{d}})}\cdot\frac{1-e^{-(C+Bx)\cdot L_{\mathrm{p}}}}{C+Bx}\cdot x \qquad (2)$$

Eqn (2) was applied for non-linear fitting of the experimentally derived data.

Vibrational assignment of Raman marker bands with help of density functional theory calculation

In order to give an assignment and interpretation of the Raman marker bands that were utilized for the detection of bilirubin and biliverdin, a thorough calculation of the molecular structures, vibrational modes, and Raman activities was performed with help of density functional theory calculations with Gaussian 09.[29] Hybrid exchange correlation functionals were applied with Becke's three-parameter exchange functional[30] (B3) as slightly modified by Stephens *et al.*[31] coupled with the correlation part of the functional from Lee, Yang, and Parr (B3LYP)[32] and Dunnings triple (cc-pVTZ) correlation consistent basis sets[33] of contracted Gaussian functions with polarized and diffuse functions.[34] The solvent water was simulated with the polarizable continuum model (PCM). The comparison of the calculated Raman spectra with the FT-Raman spectra of bilirubin and biliverdin is shown in the ESI (Fig. S1†).

Results and discussion

Raman spectroscopy is a chemically selective, non-invasive technique[35] that has evolved as an extremely powerful analytical tool for studying the structural properties of biomolecules[36] and their interaction with pharmaceuticals.[37] Because of the weak inelastic Raman scattering, various elaborated enhancement techniques have been developed, such as resonance Raman spectroscopy (RRS) and fiber enhanced Raman spectroscopy (FERS). In order to study these enhancements thoroughly, several laser excitation wavelengths have been chosen. The wavelengths $\lambda = 413$ nm and $\lambda = 364$ nm match the strong Soret band[38] of hematin and the electronic absorption bands of biliverdin and bilirubin, respectively (Fig. 2). Therefore, a strong signal enhancement of vibrational modes that are coupled to these electronic transitions is expected in resonance Raman spectroscopy.[3a] By exciting and collecting the Raman signals of the analytes within the hollow cores of elaborated optical fibers, a strong signal enhancement can be achieved.[39]

Fiber enhanced Raman spectroscopy of hematin, hemoglobin, and whole erythrocytes

First, the ability of fiber enhanced resonance Raman spectroscopy as an analytical tool for the highly sensitive quantification of heme was studied thoroughly. The laser excitation wavelength $\lambda = 532$ nm (Fig. 2) was applied for analyzing the enhancement provided by the fiber guiding. The strong peak of hematin in the Raman spectrum at 1626 cm^{-1}, which is assigned to the vibrational mode ν_{10},[3a,d] was detected with identical laser power and spectrometer setting in a series of concentration in conventional cuvette measurements and in fiber enhanced Raman sensing. The intensities of this Raman peak were analyzed for quantification of the limit-of-detection (LOD, 3× noise std.) of hematin as 36 μM and 3.6 μM, for conventional and fiber measurement respectively (Table 1). In order to exploit an additional resonance Raman enhancement, the excitation wavelength λ = 413 nm was applied, which matches the strong electronic absorption of hematin (Fig. 2B). The molecular vibration at 1373 cm^{-1}, which is assigned to the totally symmetric mode ν_4,[3a,d,e] was strongly enhanced with this wavelength. Thus a significantly improved LOD of only 0.1 μM was achieved with fiber enhanced resonance Raman spectroscopy and only 0.9 pmol sample was needed (Table 1). The spectra of hematin showed an excellent linearity between the Raman signal intensity and the analyte concentration, thus providing a reproducible quantification method. With help of this calibration, one can now measure the Raman signal of an unknown sample and quantify the actual hematin concentration.

In the next step, a more complex structure, hemoglobin was analyzed. Conventional and enhanced Raman spectra of hemoglobin were recorded respectively. The Raman band at 1373 cm^{-1} of hemoglobin, which was assigned to mode ν_4 of the heme group,[36e] was significantly enhanced in the fiber enhanced resonance Raman spectra. This Raman peak is also a very interesting marker band for monitoring the hemoglobin oxidation state,[36e,40] which provides additional information about the oxygenation of the monitored blood, and supports a differential diagnosis. The spectroscopic analysis shows that the LODs of heme were improved from 10.7 μM for conventional measurements with λ = 532 nm excitation down to 0.25 μM in fiber enhanced resonance Raman sensing. An excellent linearity was achieved for reliable quantification of hemoglobin (Fig. 4A). Fiber enhanced Raman sensing provided a higher sensitivity, which is seen in the steeper slope of the linear fits (Fig. 4A and B compared to Fig. 4C and D). Thus, FERS is capable of measuring very low hematin and hemoglobin concentrations that are not detectable anymore with conventional Raman measurements.

In order to prove the potential of FERS for investigating complex biological samples, also whole, intact erythrocytes were analyzed. Photodegradation of the red blood cells was very well avoided due to continuous analyte flow and the short time in the laser focus. Raman spectra of intact, oxygenated erythrocytes were nicely recorded with FERS (Fig. 5). In the resonance Raman spectra of the erythrocytes with λ = 413 nm excitation (Fig. 5A), the strongest Raman peak at 1376 cm^{-1} corresponds to the vibrational mode ν_4. This vibrational mode was not as strong in the Raman spectra excited with λ = 532 nm (Fig. 5B), in very good agreement to the pure hemoglobin spectra. Thus, fiber enhanced resonance Raman spectroscopy showed promising compatibility with delicate biological cells, such as intact oxygenated erythrocytes and has great potential for medical diagnosis of red blood cell related diseases, for example different types of anemia and hemolytic disorders.

Quantification and monitoring of the degradation products biliverdin and bilirubin and demonstration of the potential of FERS as diagnostic tool

The heme prostetic groups of hemoglobin in the erythrocytes are enzymatically degraded into biliverdin which is further reduced to bilirubin. These two molecules are found as the major metabolites of the porphyrine ring. As bilirubin is a quite reactive molecule, it is normally detoxified by glucuronidisation in the liver and then eliminated *via* bile. Still, in many diseases an elevated serum level of unconjugated bilirubin and/or biliverdin can be observed.[6,11–13,14b,41]

The bile pigments, biliverdin and bilirubin, cause extremely strong fluorescence signals with most excitation wavelengths in the ultraviolet and visible range and therefore Raman sensing was very challenging (data not shown). A thorough examination elucidated that the fluorescence signal was not obvious with excitation wavelength λ = 364 nm. Strong resonance enhancements can be achieved with this wavelength for bilirubin (Fig. 2C) and biliverdin (Fig. 2D) and the Raman bands around at 1615 cm^{-1} can be exploited as marker peaks for ultrasensitive analysis of biliverdin and bilirubin, respectively. The Raman spectra were strongly enhanced by applying FERS (Fig. 6A and B) and LODs of 0.13 μM and 0.5 μM were achieved for biliverdin and for bilirubin, respectively (Table 1). A good linearity between the Raman signal intensity and the

Table 1 Comparison of the improvement in the quantification of hematin, hemoglobin, biliverdin, and bilirubin in the cases of conventional (Conv.) and fiber enhanced Raman spectroscopy (FERS). The intensities of the chosen laser wavelengths were different ($I_{\lambda=413\text{ nm}}$ = 7 mW, $I_{\lambda=532\text{ nm}}$ = 10 mW, and $I_{\lambda=364\text{ nm}}$ = 3.5 mW) and all values were scaled to 7 mW ($I_{\lambda=413\text{ nm}}$) for better comparison. The amount of substance for each method was derived from the limit-of-detection (LOD) and the required sample volume

	Hematin				Hemoglobin				Biliverdin		Bilirubin	
$\lambda_{\text{exc.}}$	413 nm		532 nm		413 nm		532 nm		364 nm		364 nm	
Method	Conv.	FERS	Conv.	FERS	Conv.	FERS	Conv.	FERS	Conv.	FERS	Conv.	FERS
LOD (μM)	1	0.1	35.71	3.57	2.50	0.25	10.71	1.43	1.25	0.13	12.50	0.50
Amount (pmol)	200	0.9	7142	32.13	500	2.25	2142	12.87	250	1.17	2500	4.5

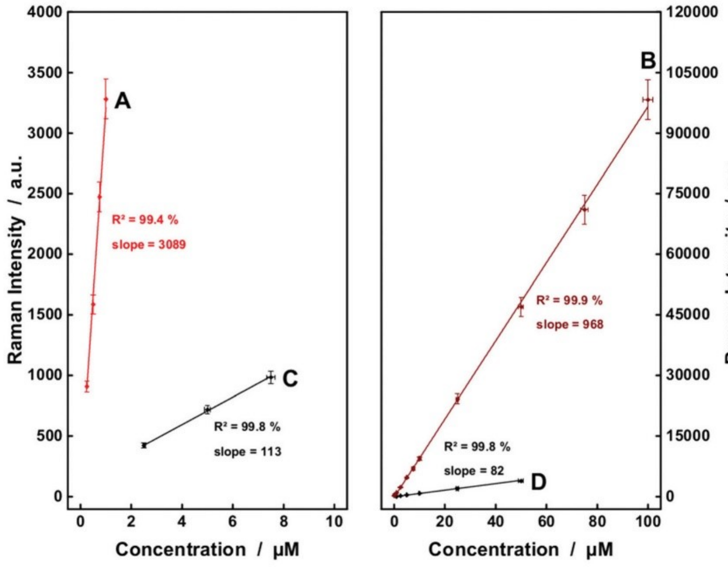

Fig. 4 Comparison of fiber enhanced Raman spectra of hemoglobin (A) and hematin (B) with conventional Raman detection of hemoglobin (C) and hematin (D) in aqueous solutions with $\lambda_{exc.}$ = 413 nm. The Raman intensities with $\lambda_{exc.}$ = 413 nm were defined by the peak heights of the Raman bands at 1373 cm^{-1} for both hematin and hemoglobin. For measurements with $\lambda_{exc.}$ = 532 nm (not shown), the Raman bands at 1626 cm^{-1} and 1638 cm^{-1} were chosen for hematin and hemoglobin, respectively.

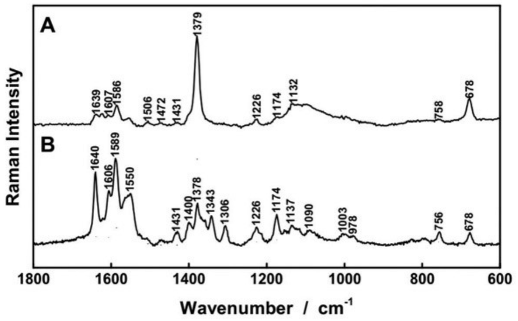

Fig. 5 Fiber enhanced Raman spectra of whole erythrocytes. Intact red blood cells (1 : 199 diluted in 1× PBS) were gently guided through the hollow core fiber and Raman spectra were taken with $\lambda_{exc.}$ = 413 nm (A) and $\lambda_{exc.}$ = 532 nm (B).

concentration was obtained, proving the potential of FERS as an analytical tool for the diagnosis of different types of diseases manifested in jaundice.[6,12] Especially the rare, not yet well understood diseases manifested in hyperbiliverdinemia[12,13,14b] need a novel tool for simultaneous sensing of very low amounts biliverdin, reported as 0.9–6.5 µM (ref. 13) and in the range from 1–10% of the total bilirubin value.[14b]

Thus, first a two component solution, consisting of 1 µM biliverdin and 50 µM bilirubin was analyzed in order to simulate typical concentrations of patients presenting hyperbilirubinemia.[13] The Raman spectra of biliverdin and bilirubin share most of the strong peaks with excitation λ = 364 nm due to the similarity in their molecular structure (Fig. 2C and D). However, some Raman bands in the wavenumber range between 1220 cm^{-1} and 1300 cm^{-1} are different and can be decomposed (Fig. 6E–G). Bilirubin contains a peak in the Raman spectrum at 1272 cm^{-1}, which is assigned to a combination of CC-stretching vibration in one pyrrole unit as well as CH-, CH_3-, and OH-wagging and scissoring vibrations (Fig. 7A). The Raman band of biliverdin at 1282 cm^{-1} can be assigned to a combined vibration which is distributed across the whole molecule and consists of strong CC- and CN-stretching vibrations in several pyrrole units as well as CH-, CH_2-, and OH-wagging and scissoring vibrations (Fig. 7B). The height of the peak at 1272 cm^{-1} in the pure Raman spectrum of a 100 µM solution of bilirubin (Fig. 6E) was quantified to 2423 counts (arbitrary units) and the height of the peak at 1282 cm^{-1} in the pure Raman spectrum of a 1 µM solution of biliverdin (Fig. 6F) was quantified to 1177 counts (arbitrary units). By deconvolution of the Raman spectrum of the two component solution (1 µM biliverdin and 50 µM bilirubin, Fig. 6G), the peak heights of the 1272 cm^{-1} and 1282 cm^{-1} bands were quantified to 1367 ± 198 and 1126 ± 212 counts (arbitrary units), respectively. Therefore, the measured concentrations were 0.9(6) ± 0.2 µM for biliverdin and 56 ± 8 µM for bilirubin. These results nicely demonstrate that FERS can be applied in the analysis of hyperbilirubinemia to quantify con-

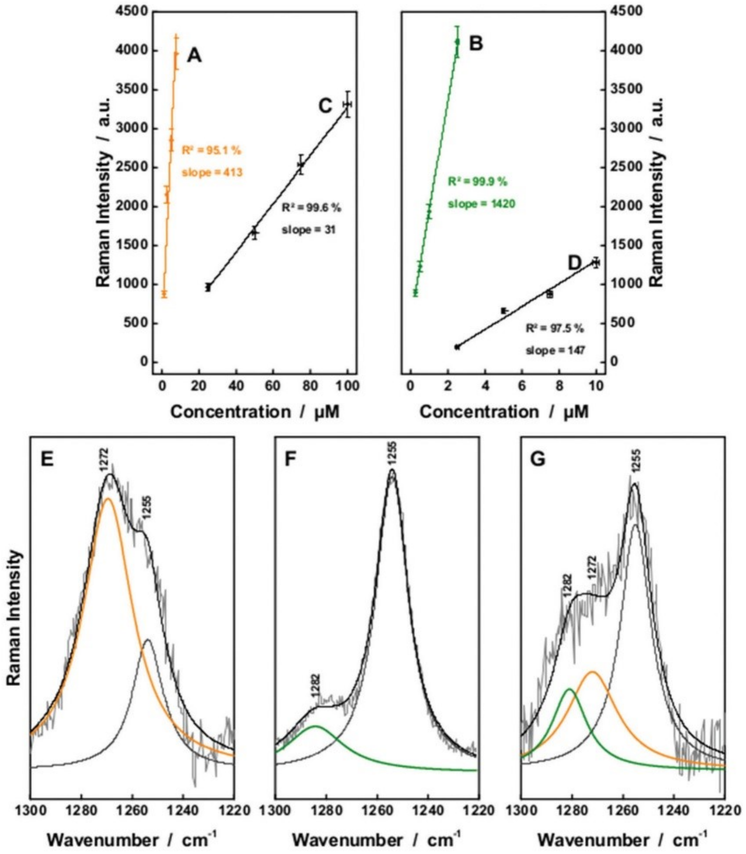

Fig. 6 The fiber enhanced and conventional Raman detection of aqueous solutions of bilirubin (A and C) as well as biliverdin (B and D) was compared with $\lambda_{exc.}$ = 364 nm. A lower limit of detection was achieved by FERS. The resonance Raman spectra of the chemically similar chromophores can be distinguished within the wavenumber range between 1220 and 1300 cm^{-1} as shown in comparison of the Raman spectra of bilirubin (E), biliverdin (F) and a mixture of 1 µM biliverdin and 50 µM bilirubin (G). Both chromophores can be quantified simultaneously in a mixture of both substances. The whole Raman spectra are given in the ESI (Fig. S2†).

centrations of biliverdin at 1 µM alongside concentrations of bilirubin at 50 µM.

For higher biliverdin concentrations of patients presenting hyperbiliverdinemia,[13] also non-resonant FERS at $\lambda_{exc.}$ = 752 nm (Fig. 2) can be applied in order to analyze a two component solution which contains 25 µM bilirubin and 75 µM biliverdin, as present in the case of green jaundice.[13] The individual solutions of 25 µM bilirubin (Fig. 8A) and 75 µM biliverdin (Fig. 8B) were thoroughly analyzed and the Raman peaks at 1253 cm^{-1} (bilirubin) and 1243 cm^{-1} (biliverdin) were identified as suitable marker bands, in order to distinguish both bile pigments. The molecular vibration of bilirubin at 1253 cm^{-1} is assigned to CH-, NH-, and OH-bending vibrations (Fig. 7C). The Raman band of biliverdin at 1243 cm^{-1} consists of CH, NH, and OH-bending vibrations (Fig. 7D). By deconvolution of the Raman spectrum of the two component mixture (Fig. 8C), the peak heights of the 1253 cm^{-1} and 1243 cm^{-1} bands in the spectrum of the mixture were quantified to 2516 ± 94 and 26 135 ± 863 counts (arbitrary units), respectively. Thus the concentrations were calculated to be 24.1 ± 1.8 µM for bilirubin and 77.2 ± 5.0 µM for biliverdin in very good agreement to the theoretical values. Hence, FERS is also a powerful technique for the analysis of the concentrations of bile pigments which appear in case of hyperbiliverdinemia.[13]

Potential of FERS for ultrasensitive analysis of heme and bile pigments

Finally, the potential of FERS was estimated considering further improvements for ultrasensitive analysis of heme and the bile pigments. The original height of the hematin peak at 1373 cm^{-1} was analyzed alongside the non-linear fitting based

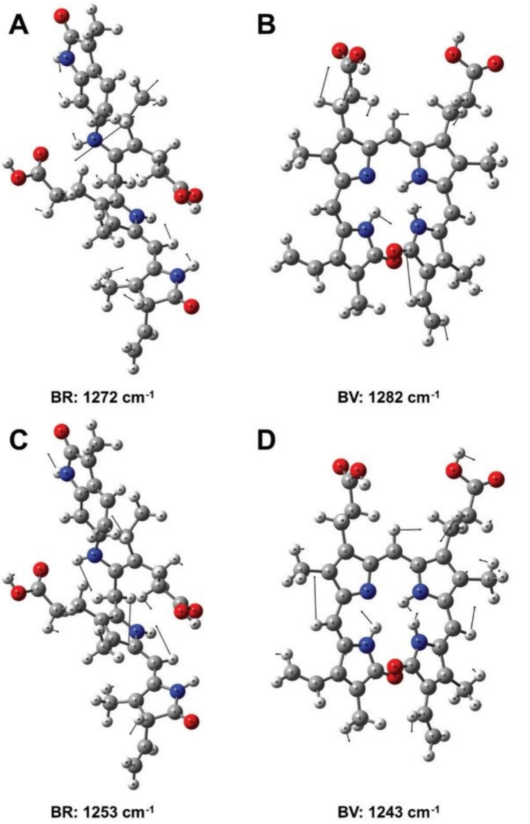

Fig. 7 Assignment of the vibrational modes of bilirubin (BR) and biliverdin (BV) that were used as Raman marker bands for sensing these molecules (see Fig. 6 and 8). The atomic displacements of the associated vibrational modes are A: BR at 1272 cm^{-1}, B: BV at 1282 cm^{-1}, C: BR at 1253 cm^{-1} and D: BV at 1243 cm^{-1}. The Raman bands originate from combined stretching and bending modes across the molecules.

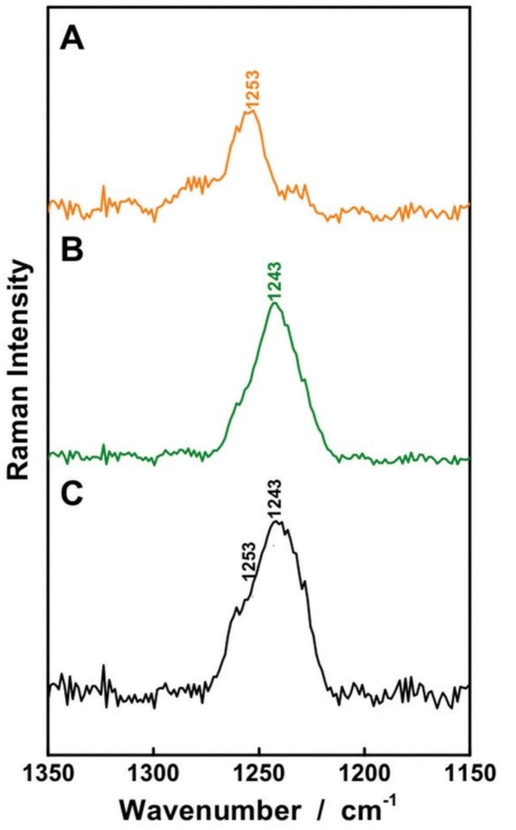

Fig. 8 Raman spectra of a 25 μM aqueous solution of pure bilirubin (A), a 75 μM aqueous solution of pure biliverdin (B), and a mixture of 25 μM bilirubin and 75 μM biliverdin (C) with $\lambda_{\text{exc.}}$ = 752 nm. The Raman bands at 1243 cm^{-1} and at 1253 cm^{-1} were utilized for the calculation of the concentrations of biliverdin and bilirubin in the mixture. The experimentally derived concentrations were 24.1 μM bilirubin (4% error) and 77.2 μM biliverdin (3% error), respectively.

on eqn (2). The peak intensities fit very well to the theoretical prediction (A = 27.6 ± 7.36 arb. unit; B = 0.00416 ± 0.00062 $\mu\text{M}^{-1}\ \text{mm}^{-1}$; C = 0.115 ± 0.046 mm^{-1}). The extinction coefficient of the liquid sample, which was derived as parameter B in the fitting function, is also very close to that adapted from absorption spectrum:

$$B_{\text{measured}} = \varepsilon_{\text{excitation}} + \varepsilon_{\text{Raman peak}} = 0.00413\ \mu\text{M}^{-1}\ \text{mm}^{-1}.$$

The original peak height of bilirubin had the same trend. The non-linear fitting based on eqn (2) derived the values A = 25.0 ± 0.4 arb. unit; B = 0.00325 ± 0.00067 $\mu\text{M}^{-1}\ \text{mm}^{-1}$; C = 0.0914 ± 0.0057 mm^{-1}. The parameter B adapted from the absorption spectrum of bilirubin solution (B_{measured} = 0.00350 $\mu\text{M}^{-1}\ \text{mm}^{-1}$) was in very good agreement to the calculated value.

The function of the Raman intensity $I_{\text{R}}(\tilde{\nu},c)$ is defined by five factors:[27] A, B, C, L_{d}, and L_{p}. Factor A expresses the intensity of the excitation laser and the overall performance of the optical coupling and sensing. Factor B is defined by the optical property of the sample and becomes larger when stronger absorbing samples are utilized. Parameter C is depending on the wave-guiding quality of the fiber. In case of ultra-low-concentration sensing, the value of x is extremely small and the influence of parameters B and L_{d} is minimized as they appear together with the analyte concentration. Thus, in further work it will be worth to develop fiber systems with better parameter C and larger L_{p}, or in other words, liquid-core fibers with superior guiding property and sufficient length.

Based on eqn (2), with improved parameters A = 20 000 arb. unit, B = 0.00416 $\mu\text{M}^{-1}\ \text{mm}^{-1}$, C = 0.0005 mm^{-1},

L_p = 4000 mm, L_d = 1 mm, one can predict an improved LOD of hematin of 1.3 pM. The accordingly predicted LODs of bilirubin and biliverdin are 66 pM and 1.6 pM, respectively.

Hence, FERS is a promising technique for rapid monitoring of slight variations of the bilirubin level at extremely low sample demand, which would be of utmost importance for an early diagnosis of mild hyperbilirubinemia in neonates[7–11] and the Gilbert[5c] and Crigler–Najjar syndrome[5d] as well as in cancer research[16a,20] and to elucidate the role of the bile pigments in brain-processes.[1]

Conclusion

This work explores the analytical potential of fiber enhanced resonance Raman spectroscopy (FERS) for ultrasensitive analysis of biologically important heme chromophores and for future applications in the diagnosis and monitoring of hyperbilirubinemia and hyperbiliverdinemia related diseases by the analysis of minimal amounts of bile pigments.

Hematin and hemoglobin were traced down to concentrations of 0.1 μM and 0.25 μM at very low sample demands of 0.9 pmol and 2.25 pmol, respectively. The FERS setup provided an excellent linearity between signal intensity and heme concentration and allowed for robust quantification of hematin and hemoglobin concentrations that were not detectable anymore with conventional Raman measurements. An improved limit of detection of only 1.3 pM hematin could be achieved based on modelling the setup performance with improved optical fibers. In order to demonstrate the abilities of the FERS technique for measuring whole cells, also intact, oxygenated erythrocytes were successfully analyzed in the hollow core optical fibers, demonstrating the great potential for medical diagnosis of red blood cell related diseases, for example different types of anemia and hemolytic disorders.

Considering the small sample volume demand of only few microliters, FERS would perfectly suit the requirements on a minimal invasive procedure for bilirubin concentration level monitoring in neonatal jaundice[11] by using capillary blood samples and for an early diagnosis of the Gilbert[5c] and Crigler–Najjar[5d] syndrome. The bile pigments biliverdin and bilirubin were quantified down to LODs of 0.13 μM and 0.5 μM, with proposed improvements down to 1.6 pM and 66 pM. This precise detection of minor elevations of the biliverdin and bilirubin levels in the micro-molar concentration range, can also open up a new prospective for further research regarding cancer and oxidative stress. Recently, efforts have been made for understanding the relationship between heme oxygenase-1 (the enzyme that converts heme to biliverdin) and the brain function.[1] With the discussed prospects for a detection of pico-molar concentration changes, a new analytical method would be available for a better understanding of the role of the bile pigments (especially biliverdin) in processes in the brain.[1]

In order to demonstrate the potential of FERS as a diagnostic tool, clinical relevant bilirubin and biliverdin concentrations were thoroughly quantified for the case of hyperbilirubinemia due to malignancy, infectious hepatitis, cirrhosis or stenosis of the common bile duct (1 μM biliverdin together with 50 μM bilirubin)[13,14b] and for hyperbiliverdinemia (75 μM biliverdin and 25 μM bilirubin).[13] Hence, FERS is a new method being capable to promote a better diagnosis.

In summary, FERS is a chemical selective, ultrasensitive technique, with extremely low sample demand and has remarkable potential for a wide range of life-science applications. The analytical benchmark experiments in this contribution provide the foundation for future clinical studies.

Acknowledgements

Funding from the federal state of Thuringia and European Union (EFRE) is highly acknowledged (2015 FE 9012 and 2015-0021). Computations at the computing centre of University Leipzig are highly acknowledged. T. F. is grateful for support from the “Studienstiftung des deutschen Volkes”. M. W. P. was supported by a grant from the German Ministry of Education and Research (01KI1501).

Notes and references

1 L. Zhang, *Heme Biology: The Secret Life of Heme in Regulating Diverse Biological Processes*, World Scientific Publishing Company, 2011.

2 M. F. Perutz, M. G. Rossmann, A. F. Cullis, H. Muirhead, G. Will and A. C. T. North, Structure of Haemoglobin: A Three-Dimensional Fourier Synthesis at 5.5-[angst]. Resolution, Obtained by X-Ray Analysis, *Nature*, 1960, **185**(4711), 416–422.

3 (*a*) B. R. Wood, S. J. Langford, B. M. Cooke, J. Lim, F. K. Glenister, M. Duriska, J. K. Unthank and D. McNaughton, Resonance Raman spectroscopy reveals new insight into the electronic structure of beta-hematin and malaria pigment, *J. Am. Chem. Soc.*, 2004, **126**(30), 9233–9239; (*b*) T. Frosch, B. Küstner, S. Schlücker, A. Szeghalmi, M. Schmitt, W. Kiefer and J. Popp, In vitro polarization-resolved resonance Raman studies of the interaction of hematin with the antimalarial drug chloroquine, *J. Raman Spectrosc.*, 2004, **35**(10), 819–821; (*c*) T. Frosch, S. Koncarevic, K. Becker and J. Popp, Morphology-sensitive Raman modes of the malaria pigment hemozoin, *Analyst*, 2009, **134**(6), 1126–1132; (*d*) T. Frosch, S. Koncarevic, L. Zedler, M. Schmitt, K. Schenzel, K. Becker and J. Popp, In Situ Localization and Structural Analysis of the Malaria Pigment Hemozoin, *J. Phys. Chem. B*, 2007, **111**(37), 11047–11056; (*e*) S. Cînta-Pînzaru, N. Peica, B. Küstner, S. Schlücker, M. Schmitt, T. Frosch, J. H. Faber, G. Bringmann and J. Popp, FT-Raman and NIR-SERS characterization of the antimalarial drugs chloroquine and mefloquine and their interaction with hematin, *J. Raman Spectrosc.*, 2006, **37**(1–3), 326–334; (*f*) M. Brückner,

K. Becker, J. Popp and T. Frosch, Fiber array based hyperspectral Raman imaging for chemical selective analysis of malaria-infected red blood cells, *Anal. Chim. Acta*, 2015, **894**, 76–84.

4 G. Kikuchi, T. Yoshida and M. Noguchi, Heme oxygenase and heme degradation, *Biochem. Biophys. Res. Commun.*, 2005, **338**(1), 558–567.

5 (*a*) R. H. Tukey and C. P. Strassburg, Human UDP-glucuronosyltransferases: metabolism, expression, and disease, *Annu. Rev. Pharmacol. Toxicol.*, 2000, **40**(1), 581–616; (*b*) A. W. Wolkoff, in *Inheritable disorders manifested by conjugated hyperbilirubinemia*, Seminars in Liver Disease, © 1983 by Thieme Medical Publishers, Inc., 2008, pp. 65–72; (*c*) P. J. Bosma, J. R. Chowdhury, C. Bakker, S. Gantla, A. de Boer, B. A. Oostra, D. Lindhout, G. N. Tytgat, P. L. Jansen and R. P. O. Elferink, The genetic basis of the reduced expression of bilirubin UDP-glucuronosyltransferase 1 in Gilbert's syndrome, *N. Engl. J. Med.*, 1995, **333**(18), 1171–1175; (*d*) I. J. Fox, J. R. Chowdhury, S. S. Kaufman, T. C. Goertzen, N. R. Chowdhury, P. I. Warkentin, K. Dorko, B. V. Sauter and S. C. Strom, Treatment of the Crigler–Najjar Syndrome Type I with Hepatocyte Transplantation, *N. Engl. J. Med.*, 1998, **338**(20), 1422–1427.

6 D. D. Houlihan, M. J. Armstrong and P. N. Newsome, Investigation of jaundice, *Medicine*, 2011, **39**(9), 518–522.

7 S. W. Ryter, Bile pigments in pulmonary and vascular disease, *Front. Pharmacol.*, 2012, **3**, 39.

8 L. Vitek and J. D. Ostrow, Bilirubin chemistry and metabolism; harmful and protective aspects, *Curr. Pharm. Des.*, 2009, **15**(25), 2869–2883.

9 M. Kaplan and C. Hammerman, Understanding severe hyperbilirubinemia and preventing kernicterus: adjuncts in the interpretation of neonatal serum bilirubin, *Clin. Chim. Acta*, 2005, **356**(1), 9–21.

10 D. Zakim, T. D. Boyer, M. P. Manns and A. J. Sanyal, *Zakim and Boyer's Hepatology*, Elsevier Health Sciences, 2011, 1096–1097.

11 J. M. Kirk, Neonatal jaundice: a critical review of the role and practice of bilirubin analysis, *Ann. Clin. Biochem.*, 2008, **45**(5), 452–462.

12 E. A. Larson, G. T. Evans and C. J. Watson, A study of the serum biliverdin concentration in various types of jaundice, *J. Lab. Clin. Med.*, 1947, **32**(5), 481.

13 M. Gåfvels, P. Holmström, A. Somell, F. Sjövall, J. O. Svensson, L. Ståhle, U. Broomé and P. Stål, A novel mutation in the biliverdin reductase-A gene combined with liver cirrhosis results in hyperbiliverdinaemia (green jaundice), *Liver Int.*, 2009, **29**(7), 1116–1124.

14 (*a*) S. M. Purcell, F. H. Wians Jr., N. B. Ackerman Jr. and B. M. Davis, Hyperbiliverdinemia in the bronze baby syndrome, *J. Am. Acad. Dermatol.*, 1987, **16**(1), 172–177; (*b*) A. J. Greenberg, I. Bossenmaier and S. Schwartz, Green jaundice, *Am. J. Dig. Dis.*, 1971, **16**(10), 873–880; (*c*) J. Prichard, Biliverdin appearing in a case of malnutrition, *Br. J. Clin. Pract.*, 1972, **26**(10), 481.

15 (*a*) L. J. Horsfall, G. Rait, K. Walters, D. M. Swallow, S. P. Pereira, I. Nazareth and I. Petersen, Serum bilirubin and risk of respiratory disease and death, *JAMA, J. Am. Med. Assoc.*, 2011, **305**(7), 691–697; (*b*) E. H. Temme, J. Zhang, E. G. Schouten and H. Kesteloot, Serum bilirubin and 10-year mortality risk in a Belgian population, *Cancer Causes Control*, 2001, **12**(10), 887–894.

16 (*a*) A. C. Bulmer, K. Ried, J. T. Blanchfield and K.-H. Wagner, The anti-mutagenic properties of bile pigments, *Mutat. Res., Rev. Mutat. Res.*, 2008, **658**(1), 28–41; (*b*) Y. Katoh, N. Nemoto, M. Tanaka and S. Takayama, Inhibition of benzo [*a*] pyrene-induced mutagenesis in Chinese hamster V79 cells by hemin and related compounds, *Mutat. Res. Lett.*, 1983, **121**(2), 153–157.

17 F. McPhee, P. Caldera, G. Bemis, A. McDonagh, I. Kuntz and C. Craik, Bile pigments as HIV-1 protease inhibitors and their effects on HIV-1 viral maturation and infectivity in vitro, *Biochem. J.*, 1996, **320**, 681–686.

18 P. Rao, R. Suzuki, S. Mizobuchi, T. Yamaguchi and S. Sasaguri, Bilirubin exhibits a novel anti-cancer effect on human adenocarcinoma, *Biochem. Biophys. Res. Commun.*, 2006, **342**(4), 1279–1283.

19 P. Keshavan, S. J. Schwemberger, D. L. Smith, G. F. Babcock and S. D. Zucker, Unconjugated bilirubin induces apoptosis in colon cancer cells by triggering mitochondrial depolarization, *Int. J. Cancer*, 2004, **112**(3), 433–445.

20 Y. Katoh, N. Nemoto, M. Tanaka and S. Takayama, Inhibition of Benzo[a]Pyrene-Induced Mutagenesis in Chinese-Hamster V79-Cells by Hemin and Related-Compounds, *Mutat. Res.*, 1983, **121**(2), 153–157.

21 M. Prezelj, Enzymic determination of total bilirubin in serum with the BA-1000, *Clin. Chem.*, 1988, **34**(1), 176–177.

22 B. T. Doumas, B. W. Perry, E. A. Sasse and J. V. Straumfjord, Standardization in bilirubin assays: evaluation of selected methods and stability of bilirubin solutions, *Clin. Chem.*, 1973, **19**(9), 984–993.

23 (*a*) X. Li and Z. Rosenzweig, A fiber optic sensor for rapid analysis of bilirubin in serum, *Anal. Chim. Acta*, 1997, **353**(2), 263–273; (*b*) C. Lu, J.-M. Lin and C. W. Huie, Determination of total bilirubin in human serum by chemiluminescence from the reaction of bilirubin and peroxynitrite, *Talanta*, 2004, **63**(2), 333–337.

24 (*a*) C.-Y. Huang, M.-J. Syu, Y.-S. Chang, C.-H. Chang, T.-C. Chou and B.-D. Liu, A portable potentiostat for the bilirubin-specific sensor prepared from molecular imprinting, *Biosens. Bioelectron.*, 2007, **22**(8), 1694–1699; (*b*) M. A. Rahman, K.-S. Lee, D.-S. Park, M.-S. Won and Y.-B. Shim, An amperometric bilirubin biosensor based on a conductive poly-terthiophene–Mn (II) complex, *Biosens. Bioelectron.*, 2008, **23**(6), 857–864.

25 (*a*) J. J. Lauff, M. E. Kasper and R. T. Ambrose, Separation of bilirubin species in serum and bile by high-performance reversed-phase liquid chromatography, *J. Chromatogr. B: Biomed. Sci. Appl.*, 1981, **226**(2), 391–402; (*b*) J. J. Lauff, M. E. Kasper, T. W. Wu and R. T. Ambrose, Isolation and

preliminary characterization of a fraction of bilirubin in serum that is firmly bound to protein, *Clin. Chem.*, 1982, **28**(4), 629–637.

26 (*a*) B. J. Marquardt, P. G. Vahey, R. E. Synovec and L. W. Burgess, A Raman waveguide detector for liquid chromatography, *Anal. Chem.*, 1999, **71**(21), 4808–4814; (*b*) M. J. Pelletier and R. Altkorn, Raman sensitivity enhancement for aqueous protein samples using a liquid-core optical-fiber cell, *Anal. Chem.*, 2001, **73**(6), 1393–1397; (*c*) R. Altkorn, I. Koev and M. J. Pelletier, Raman Performance Characteristics of Teflon®-AF 2400 Liquid-Core Optical-Fiber Sample Cells, *Appl. Spectrosc.*, 1999, **53**(10), 1169–1176; (*d*) R. Altkorn, M. D. Malinsky, R. P. Van Duyne and I. Koev, Intensity considerations in liquid core optical fiber Raman spectroscopy, *Appl. Spectrosc.*, 2001, **55**(4), 373–381; (*e*) D. Qi and A. J. Berger, Quantitative concentration measurements of creatinine dissolved in water and urine using Raman spectroscopy and a liquid core optical fiber, *J. Biomed. Opt.*, 2005, **10**(3), 031115; (*f*) Y. Tian, L. Zhang, J. Zuo, Z. Li, S. Gao and G. Lu, Raman sensitivity enhancement for aqueous absorbing sample using Teflon-AF 2400 liquid core optical fibre cell, *Anal. Chim. Acta*, 2007, **581**(1), 154–158; (*g*) D. Qi and A. J. Berger, Quantitative analysis of Raman signal enhancement from aqueous samples in liquid core optical fibers, *Appl. Spectrosc.*, 2004, **58**(10), 1165–1171; (*h*) R. Altkorn, I. Koev, R. P. VanDuyne and M. Litorja, Low-loss liquid-core optical fiber for low-refractive-index liquids: fabrication, characterization, and application in Raman spectroscopy, *Appl. Opt.*, 1997, **36**(34), 8992–8998; (*i*) R. Altkorn, I. Koev and A. Gottlieb, Waveguide capillary cell for low-refractive-index liquids, *Appl. Spectrosc.*, 1997, **51**(10), 1554–1558.

27 T. Frosch, D. Yan and J. Popp, Ultrasensitive Fiber Enhanced UV Resonance Raman Sensing of Drugs, *Anal. Chem.*, 2013, **85**(13), 6264–6271.

28 W. J. Hehre, R. F. Stewart and J. A. Pople, Self-Consistent Molecular-Orbital Methods. I. Use of Gaussian Expansions of Slater-Type Atomic Orbitals, *J. Chem. Phys.*, 1969, **51**(6), 2657–2664.

29 M. J. Frisch, G. W. Trucks, H. B. Schlegel, G. E. Scuseria, M. A. Robb, J. R. Cheeseman, G. Scalmani, V. Barone, B. Mennucci, G. A. Petersson, H. Nakatsuji, M. Caricato, X. Li, H. P. Hratchian, A. F. Izmaylov, J. Bloino, G. Zheng, J. L. Sonnenberg, M. Hada, M. Ehara, K. Toyota, R. Fukuda, J. Hasegawa, M. Ishida, T. Nakajima, Y. Honda, O. Kitao, H. Nakai, T. Vreven, J. A. Montgomery Jr., J. E. Peralta, F. Ogliaro, M. J. Bearpark, J. Heyd, E. N. Brothers, K. N. Kudin, V. N. Staroverov, R. Kobayashi, J. Normand, K. Raghavachari, A. P. Rendell, J. C. Burant, S. S. Iyengar, J. Tomasi, M. Cossi, N. Rega, N. J. Millam, M. Klene, J. E. Knox, J. B. Cross, V. Bakken, C. Adamo, J. Jaramillo, R. Gomperts, R. E. Stratmann, O. Yazyev, A. J. Austin, R. Cammi, C. Pomelli, J. W. Ochterski, R. L. Martin, K. Morokuma, V. G. Zakrzewski, G. A. Voth, P. Salvador, J. J. Dannenberg, S. Dapprich, A. D. Daniels, Ö. Farkas, J. B. Foresman, J. V. Ortiz, J. Cioslowski and D. J. Fox, *Gaussian 09*, Gaussian, Inc., Wallingford, CT, USA, 2009.

30 A. D. Becke, Density-Functional Thermochemistry .2. The Effect of the Perdew-Wang Generalized-Gradient Correlation Correction, *J. Chem. Phys.*, 1992, **97**(12), 9173–9177.

31 P. J. Stephens, F. J. Devlin, C. F. Chabalowski and M. J. Frisch, Ab-Initio Calculation of Vibrational Absorption and Circular-Dichroism Spectra Using Density-Functional Force-Fields, *J. Phys. Chem.*, 1994, **98**(45), 11623–11627.

32 C. Lee, W. Yang and R. G. Parr, Development of the Colle-Salvetti correlation-energy formula into a functional of the electron density, *Phys. Rev. B: Condens. Matter*, 1988, **37**(2), 785–789.

33 (*a*) T. H. Dunning, Gaussian-Basis Sets for Use in Correlated Molecular Calculations .1. The Atoms Boron through Neon and Hydrogen, *J. Chem. Phys.*, 1989, **90**(2), 1007–1023; (*b*) T. H. Dunning, A road map for the calculation of molecular binding energies, *J. Phys. Chem. A*, 2000, **104**(40), 9062–9080.

34 J. A. Pople, H. B. Schlegel, R. Krishnan, D. J. Defrees, J. S. Binkley, M. J. Frisch, R. A. Whiteside, R. F. Hout and W. J. Hehre, Molecular-Orbital Studies of Vibrational Frequencies, *Int. J. Quantum Chem.*, 1981, **20**(S15), 269–278.

35 (*a*) T. Frosch and J. Popp, Relationship between molecular structure and Raman spectra of quinolines, *J. Mol. Struct.*, 2009, **924–926**, 301–308; (*b*) R. Keiner, M. Herrmann, K. Kuesel, J. Popp and T. Frosch, Rapid monitoring of intermediate states and mass balance of nitrogen during denitrification by means of innovative cavity enhanced Raman multi-gas sensing, *Anal. Chim. Acta*, 2015, **864**, 39–47; (*c*) R. Keiner, T. Frosch, T. Massad, S. Trumbore and J. Popp, Enhanced Raman multigas sensing - a novel tool for control and analysis of (13)CO2 labeling experiments in environmental research, *Analyst*, 2014, **139**(16), 3879–3884; (*d*) T. Frosch, R. Keiner, B. Michalzik, B. Fischer and J. Popp, Investigation of gas exchange processes in peat bog ecosystems by means of innovative Raman gas spectroscopy, *Anal. Chem.*, 2013, **85**(3), 1295–1299.

36 (*a*) S. A. Asher, UV resonance Raman studies of molecular structure and dynamics: applications in physical and biophysical chemistry, *Annu. Rev. Phys. Chem.*, 1988, **39**(1), 537–588; (*b*) J. M. Turner, J. N. Gayles and H. M. Turner, Resonance Raman-Spectra of Hemoglobin-a and Hemoglobin-S, *Bull. Am. Phys. Soc.*, 1975, **20**(4), 729–729; (*c*) T. G. Spiro, Resonance Raman spectroscopy. New structure probe for biological chromophores, *Acc. Chem. Res.*, 1974, **7**(10), 339–344; (*d*) B. R. Wood, L. Hammer, L. Davis and D. McNaughton, Raman microspectroscopy and imaging provides insights into heme aggregation and denaturation within human erythrocytes, *J. Biomed. Opt.*, 2005, **10**(1), 14005; (*e*) B. R. Wood and D. McNaughton, Raman excitation wavelength investigation of single red blood cells in vivo, *J. Raman Spectrosc.*, 2002, **33**(7), 517–523; (*f*) T. Frosch, T. Meyer, M. Schmitt and J. Popp, Device for Raman Difference Spectroscopy, *Anal. Chem.*, 2007, **79**(16), 6159–6166.

37 (*a*) T. Frosch, M. Schmitt and J. Popp, Raman spectroscopic investigation of the antimalarial agent mefloquine, *Anal. Bioanal. Chem.*, 2007, **387**(5), 1749–1757; (*b*) T. Frosch, M. Schmitt, T. Noll, G. Bringmann, K. Schenzel and J. Popp, Ultrasensitive in situ Tracing of the Alkaloid Dioncophylline A in the Tropical Liana Triphyophyllum peltatum by Applying Deep-UV Resonance Raman Microscopy, *Anal. Chem.*, 2007, **79**(3), 986–993; (*c*) T. Frosch, M. Schmitt, K. Schenzel, J. H. Faber, G. Bringmann, W. Kiefer and J. Popp, In vivo localization and identification of the antiplasmodial alkaloid dioncophylline A in the tropical liana Triphyophyllum peltatum by a combination of fluorescence, near infrared Fourier transform Raman microscopy, and density functional theory calculations, *Biopolymers*, 2006, **82**(4), 295–300; (*d*) T. Frosch and J. Popp, Structural analysis of the antimalarial drug halofantrine by means of Raman spectroscopy and density functional theory calculations, *J. Biomed. Opt.*, 2010, **15**(4), 041516.

38 A. Smith and M. Witty, *Heme, Chlorophyll, and Bilins: Methods and Protocols*, Humana Press, 2001.

39 (*a*) A. Hartung, J. Kobelke, A. Schwuchow, K. Wondraczek, J. Bierlich, J. Popp, T. Frosch and M. A. Schmidt, Double antiresonant hollow core fiber – guidance in the deep ultraviolet by modified tunneling leaky modes, *Opt. Express*, 2014, **22**(16), 19131; (*b*) A. Hartung, J. Kobelke, A. Schwuchow, K. Wondraczek, J. Bierlich, J. Popp, T. Frosch and M. A. Schmidt, Origins of modal loss of antiresonant hollow-core optical fibers in the ultraviolet, *Opt. Express*, 2015, **23**(3), 2557–2565.

40 I. P. Torres, J. Terner, R. N. Pittman, E. Proffitt and K. R. Ward, Measurement of hemoglobin oxygen saturation using Raman microspectroscopy and 532-nm excitation, *J. Appl. Physiol.*, 2008, **104**(6), 1809–1817.

41 T. Orui, H. Yasuda, M. Yamaya, T. Matsui and H. Sasaki, Transient relief of asthma symptoms during jaundice: a possible beneficial role of bilirubin, *Tohoku J. Exp. Med.*, 2003, **199**(3), 193–196.

7.3. Fiber-enhanced Raman sensing of levofloxacin by PCF bandgap-shifting into the visible range

Reproduced from Di Yan, Juergen Popp, Mathias W. Pletz, Torsten Frosch; Fiber-enhanced Raman Sensing of Levofloxacin by PCF Bandgap-Shifting into the Visible Range. Analytical Methods (2018), 10, 586-592 with permission from Royal Society of Chemistry.

Analytical Methods

PAPER

View Article Online
View Journal

Cite this: DOI: 10.1039/c7ay02398g

Fiber enhanced Raman sensing of levofloxacin by PCF bandgap-shifting into the visible range

Di Yan,[a] Jürgen Popp,[acd] Mathias W. Pletz[b] and Torsten Frosch*[acd]

Fiber enhanced Raman spectroscopy is introduced for chemically selective and sensitive monitoring of antibiotics in aqueous media. The bandgap of a hollow core photonic crystal was blue shifted, in order to provide low loss light guidance in the important visible range in a water filled central core of the fiber. Such a sensor fiber provides a spectral window for light guidance for a complete Raman spectrum up to 4000 cm^{-1} with λ_{exc} = 532 nm and enables an extremely strong light–analyte interaction within the liquid-filled fiber core. It was shown that a precise optical coupling must be guaranteed, in order to provide strong analyte signals and to avoid background noise. The fiber itself was used as an optical waveguide and also as a miniaturized sample container for antibiotic solutions. A strongly improved analytical sensitivity could be achieved and it was possible to improve the limit-of-detection for the frequently used broad spectrum antibiotic levofloxacin down to clinically relevant concentrations of 20 μM with only 8 nL sample volume in the fiber core. Fiber enhanced Raman spectroscopy has great potential as a new point of care tool for chemical selective and ultrasensitive monitoring of antibiotic levels, enabling rapid dose adjustment in critically ill patients with severe infections, who require individual dosing due to large inter- and intra-individual changes in pharmacokinetic properties.

Received 11th October 2017
Accepted 25th November 2017

DOI: 10.1039/c7ay02398g

rsc.li/methods

Introduction

Approximately 50 to 300 cases out of 100 000 patients with infectious disease evolve severe sepsis, with high mortality rates of up to 70% when complicated by shock and multiple organ failures.[1] The risk of death due to sepsis increases by 7.6% with every hour of delay of a proper antibiotic administration.[2] Thus early administration of an appropriate antibiotic therapy is the cornerstone of treatment[3] and an individualized monitoring of antibiotic plasma concentrations is essential for setting the correct dosage for critical-care patients.[4] Clinical studies, *e.g.* of moxifloxacin, have shown that plasma levels of antibiotics exhibit large inter- and even intra-individual changes in patients with severe sepsis and septic shock.[5] This is explained by altered pharmacokinetic parameters such as increased volume of distribution and changes in the protein bound fraction as well as hepatic and renal clearance. These alterations can change quickly within hours, are not reliably predictable and result in underdosing leading to increased treatment failure or overdosing associated with increased drug toxicity.[6] Therefore it has become increasingly clear within the last few years that licensed dose recommendations, that are derived from studies in healthy volunteers or patients with mild or moderate infections, cannot be transferred to critically ill patients with severe infections. For some anti-infectives like vancomycin, aminoglycosides or voriconazole, dose adjustment based on therapeutic drug monitoring has already been shown to improve the clinical outcome.[7–9] Currently the most commonly used method for the quantification of antibiotic levels is high-performance liquid chromatography (HPLC)[10–12] which can allow the detection of levofloxacin down to the μM or even sub-μM level.[13,14] However, chromatography based methods are time consuming and labor intensive and require complex sample treatment procedures. The time-to-result intervals for these techniques are several hours or even days in practice. Therefore, they are neither suitable for high throughput analyses nor point of care diagnostics. Thus, it is important to develop an easy-to-use, highly selective and sensitive technique for a fast and individualized quantification of antibiotic concentrations.

Raman spectroscopy offers the unique advantage of selective "fingerprint" information of molecules.[15–20] However, conventionally it is very difficult to detect low-concentrated analytes due to the weak Raman signals[21–24] and thus various enhancement techniques have been developed.[25–30] A promising example is the application of elaborated micro-structured optical fibers, which guide the light with low losses in the inner hollow core[31–33] and provide great potential for biomolecular sensing.[34–37] By exciting the liquid sample in the fiber core along an extended path length, such a sensor fiber can

---

[a] *Leibniz Institute of Photonic Technology, Jena, Germany. E-mail: torsten.frosch@uni-jena.de; torsten.frosch@gmx.de*

[b] *Center for Infectious Diseases and Infection Control, Jena University Hospital, Germany*

[c] *Friedrich Schiller University, Institute of Physical Chemistry, Jena, Germany*

[d] *Friedrich Schiller University, Abbe Center of Photonics, Jena, Germany*

remarkably enhance the Raman signal and hence provide opportunities for the detection of low-concentrated analytes.[38–43] Fiber enhanced Raman spectroscopy has high potential for miniaturization. Portable or even handheld Raman devices with reusable sensor fibers will allow bedside measurements of antibiotic concentrations, and will enable clinicians to adjust doses rapidly.

In hollow core photonic crystal fibers (HC-PCFs),[31,44–47] the laser excitation wavelength has to be matched to a specific spectral bandgap. By filling the fiber hollow cores completely with liquid media the bandgap can be shifted to lower wavelengths.[48,49] This effect was used in Raman sensing in the NIR range,[38,39,49] but was not yet shown in the visible range, where the Raman scattering is much stronger ($I_R \propto \omega^4$), conventional CCD detectors have their highest sensitivities which is extremely interesting for bio-sensing. For example, the Raman intensity with excitation wavelength $\lambda = 532$ nm is about 5 times stronger compared to excitation with $\lambda = 785$ nm.[50]

HC-PCFs and other types of optical fibers are employed in various Raman enhancing approaches. In some earlier studies the laser wavelength was not matched to the shifted bandgap, but the inner hollow core of the fiber was still useful as a miniaturized sample container for SERS experiments.[51–56] Raman probes were successfully applied for Raman analysis of liquid samples at the fiber tip.[57,58]

In this work the potential of HC-PCFs with the shifted bandgap into the visible range should be explored for tracing low-concentrated analyte molecules in aqueous solutions in their inner hollow core by means of Raman spectroscopy. The preparation, the optical characterization and handling of such sensor fibers will be thoroughly studied. Finally, the quantification of levofloxacin should be evaluated, which is a second generation fluoroquinolone with high clinical importance.[59] The potential for quantification of clinically relevant concentrations of levofloxacin in minimized sample volumes will be proven with help of this new type of sensor fiber.

Materials and methods

All chemicals were purchased from Sigma-Aldrich and used without further purification. The HC-PCF provided a core diameter of 10 µm, a diameter of the holey region of 50 µm, center wavelength 1060 nm, and NA = 0.2. It features a center hollow core and a periodic array of air channels (Fig. 1A). Both ends of the fiber were cleaved and examined with a microscope, as the quality of the fiber end face is of key importance for correct light coupling. The length of the sensor fiber was 10 cm. The liquid samples were pumped through the fiber with constant pressure during the measurements. An HPLC pump (Jasco PU-2085 Plus) was used to provide constant pressure and flow of the liquid media through the HC-PCF during the measurement of the Raman spectra. Broadband light from a super-continuum source (NKT, SuperK compact) was coupled into the HC-PCF with an objective lens (Olympus, 10×/NA 0.25), and the light that propagated through the fiber was analyzed by using an optical spectrum analyzer (Ando AQ6315E) (Fig. 1C).

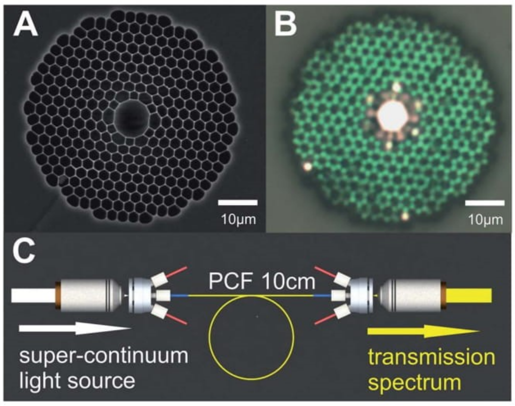

Fig. 1 (A) Electron microscopy image of the end face of the hollow core photonic crystal fiber. (B) Water filled fiber with super continuum illumination from the backside. The bright central core indicates that the light is mostly confined in the liquid core in a broad spectral range. The green color of the microstructure and the bright spots on the outer edge are caused by the imperfection of the photonic crystal. (C) Schematic sketch of the setup for fiber transmission measurements.

Raman spectra were acquired with a LabRAM system (Horiba JobinYvon, HR800) equipped with a liquid-nitrogen-cooled CCD detector and a green excitation laser ($\lambda_{exc} = 532$ nm, $I_{Laser} = 100$ mW at the sample, beam diameter $d_{beam} = 1$ mm). The laser was focused into the fiber by using an objective lens (Olympus, 10×/NA 0.25), and the backscattered Raman signal was collected with the same objective (Fig. 2).

For quantitative and reproducible Raman analysis, a stable optical coupling geometry of the fiber is of key importance. This was achieved with the application of a custom-designed fiber-adapter assembly[40] (Fig. 2 inset), which provides an optical window for coupling the laser light into the fiber and two side-ports for an analyte flow and convenient cleaning procedure (Fig. 2). Because of the small core size of the sensor fiber (approx. 10 µm), a proper optical coupling could not be achieved without such a specifically designed fiber-adapter assembly.[40]

In order to achieve high reproducibility for precise quantification of the antibiotics, all measured Raman spectra were normalized to the Raman peak of the solvent water at 1645 cm^{-1}. The quantity of water can be considered as constant for trace analysis experiments. Moreover, the target Raman peaks of the analytes are very close to this reference band (~2 nm). Thus, the Raman peak of water is a reliable internal reference for cancelling out all fluctuations of laser intensity and instrumental performance. The signal-to-noise ratio (SNR) was calculated from the height of the Lorentzian fit of the target peaks and the root-mean-square (RMS) values of the baseline. The limit-of-detection (LOD) was derived when the SNR was equal to three. This is a valid approximation for weak Raman peaks with low intensity, where the noise is comparable to the baseline. The SNR values were employed to determine the LODs, however the performance of fiber enhanced Raman

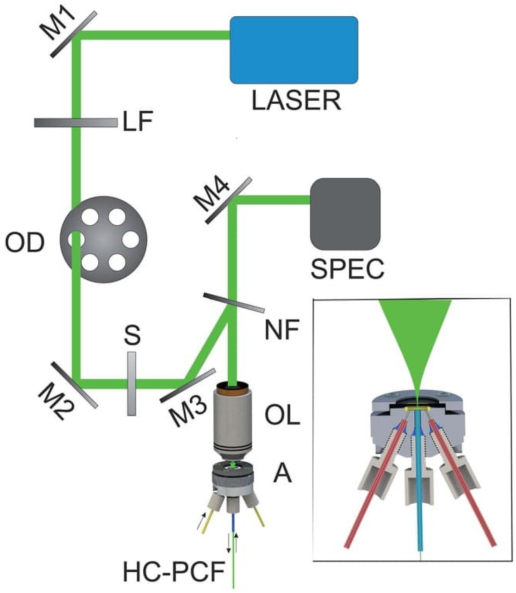

Fig. 2 Schematic sketch of the optical setup for fiber enhanced Raman spectroscopy (FERS). The setup consists of a laser, mirrors (M1–4), a laser line filter (LF), an optical density filter (OD), a shutter (S), a notch filter (NF), an objective lens (OL), a fiber adapter (A), a hollow-core photonic crystal fiber (HC-PCF), and a Raman spectrometer (SPEC). Inset: sectional view of the fiber adapter assembly. The laser light is coupled into the fiber core through an optical window and the analyte solution is pumped through the fiber by side connectors.

spectroscopy (FERS) was compared on the basis of the peak intensities. The acquisition time of the Raman spectra was always 120 s, and the slit width of a spectrometer was fixed at 100 μm, in order to compare the performance of conventional and fiber enhanced measurements with identical settings. All measurements were repeated three times.

A normal mode assignment for levofloxacin was performed with help of density functional theory calculations with Gaussian 03.[60] Hybrid exchange correlation functionals were applied with Becke's three-parameter exchange functional[61] (B3) as slightly modified by Stephens *et al.*,[62] coupled with the correlation part of the functional from Perdew and Wang[63,64] (B3PW91) and triple (6-311+G(d,p)) split valence basis sets of contracted Gaussian functions with polarized and diffuse functions.[65]

Results and discussion

In this contribution the bandgap shifting into the visible range for high efficiency Raman sensing is demonstrated and the precision requirements for the adjustment of the filigree sensor fiber are evaluated. The unique abilities of the sensor fiber are exploited for ultrasensitive analysis of the important antibiotic levofloxacin at clinically relevant levels.

Bandgap shifting into the visible range

The original bandgap of the transmission spectrum of the hollow core photonic crystal fiber is centered at 1060 nm. The diameter of the inner hollow core is 10 μm and the cladding has a pitch size of 2.75 μm (Fig. 1A). The photonic bandgap of the fiber is achieved by the periodic arrangement of air holes in silica and shifts to another wavelength range if the fiber is filled with a solution with a different refractive index.[66] The shift in the transmission band of the water filled HC-PCF can be estimated by the following equation:[48,67]

$$\lambda' = \lambda_0 \left[\frac{1 - \left(\dfrac{n_{\text{liquid}}}{n_{\text{glass}}} \right)^2}{1 - \left(\dfrac{n_{\text{air}}}{n_{\text{glass}}} \right)^2} \right]^{1/2} \qquad (1)$$

where λ_0 is the center wavelength of the original bandgap of the air-filled fiber, λ' is the center wavelength of the new bandgap, n_{liquid} is the refractive index of the liquid sample, and n_{glass} is the refractive index of the glass material.

However, eqn (1) can only predict the center of the transmission band. The precise position of the rising and falling edges of the transmission band, which strongly constrain the selection of the laser wavelength and the accessible range of the Raman spectrum, can be determined experimentally.

The visual inspection of the water filled fiber with supercontinuum illumination confirms that light of a broad spectral range is confined in the central liquid core (Fig. 1B). The cladding region is shining in green, because the white light at the other end of the fiber is not perfectly focused into the fiber core and also couples in some cladding modes. According to eqn (1), the center of the transmission spectrum of the water-filled fiber is predicted at 593 nm. The experimental results (Fig. 3) show that the transmission band ranges from 510 nm to 680 nm (with band edges at half of the maximum transmission),

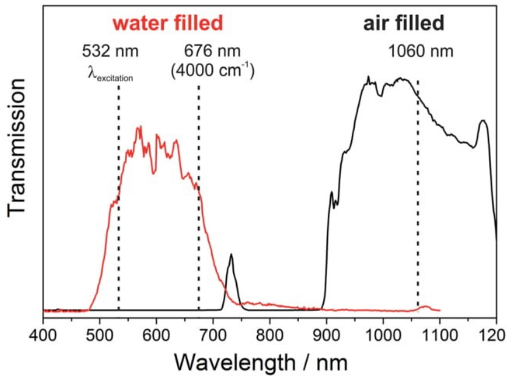

Fig. 3 Transmission spectra of an air filled and a water filled HC-PCF. The bandgap of the water filled fiber is blue-shifted into the visible spectral range. The sensor fiber provides low loss optical guidance for an excitation with a laser wavelength of λ = 532 nm and a Raman spectrum up to 4000 cm^{-1} (corresponds to 676 nm).

which is in very good agreement with the predicted values. Thus, a laser excitation wavelength of $\lambda = 532$ nm was employed, which provides excellent transmission for a Raman spectral range of up to 4000 cm^{-1}. This band-gap shifting effect applies similarly to water ($n = 1.33$) as well as to urine ($n = 1.33$) and plasma ($n = 1.34$).

Raman spectroscopic test measurements and evaluation of the necessary coupling precision

In the first step, the performance of the fiber enhanced Raman setup was tested with an ethanol–water solution (10% v/v). The refractive index of the solution (1.338) was very close to the value of water (1.333) and therefore the difference of the bandgap shifting is negligible. The solution shows a very intense Raman peak of the νC–C–O symmetric stretching mode of ethanol at 880 cm^{-1}, which can be used for the quantification of the enhancement. In order to evaluate the advantage of the sensor fiber for the Raman experiments, the laser was first focused into the bulk liquid of the solution in a cuvette and a conventional Raman spectrum was acquired. Then the cuvette was replaced with the sensor fiber and the Raman spectra were recorded with identical experimental parameters. The comparison nicely demonstrates that the fiber enhanced Raman spectrum has a much higher intensity compared to the conventional cuvette measurement (the Raman peak height at 880 cm^{-1} is 52 times higher) (Fig. 4A). For quantitative measurements of very low analyte concentrations the important parameter is the signal-to-noise ratio (SNR). The SNR level in the fiber enhanced Raman spectrum was improved by one order of magnitude (Fig. 4B). Furthermore, only 8 nL of sample solution was needed for highly efficient Raman measurements in the central hollow core of the sensor fiber. Thus the minimized volume of the fiber hollow core reduces the required sample amount significantly, but also causes challenges for the optical coupling.

In fiber based Raman sensing, the enhancement strongly relies on a very good guidance of the laser in the liquid core, and of the same importance, the collection of the Raman scattering from the mode field in the fiber core. A mismatch of the focus position of the objective lens and the fiber core will strongly affect the performance of the Raman measurements. This effect was thoroughly studied and the intensity of the Raman peak of ethanol at 880 cm^{-1} was measured for various coupling positions. The analysis shows that the Raman intensity drops to 90% with an error in the lateral coupling position of ±1.5 μm (Fig. 5A). Further offsets will not only strongly reduce the Raman intensity of the analyte peak (Fig. 5A), but also increase the background Raman bands of the silica fiber material (Fig. 5B) and thus cause an increased noise level. A mismatch of the longitudinal focus position (defocusing) has only a small effect, due to the relatively low NA of the objective and a depth of focus of 8.5 μm. The precision of the lateral position of ±1.5 μm was easily achieved in the lab-setup and guaranteed for the antibiotic measurements. These requirements have also to be considered in the design of an envisioned miniaturized setup for clinical application.

Fiber enhanced Raman sensing of levofloxacin

The plasma concentration of levofloxacin reaches 27 μM within 1 hour after intravenous administration of 500 mg levofloxacin.[59] Levofloxacin distributes widely throughout the body and drug concentrations in tissues and fluids are generally higher than those observed in plasma.[68] As the elimination is mainly by renal excretion, levofloxacin in urine is detectable at concentrations of 374 μM and 97 μM after 12 and 24 hours of dosing, respectively.

The Raman spectra of levofloxacin solutions show prominent Raman peaks within the spectral range from 1300 to 1700 cm^{-1}. The most intense peak in the Raman spectrum at 1619 cm^{-1} was chosen for the concentration measurements. This Raman band was assigned to strong combined νC=C stretching vibrations of the aromatic ring structure (Fig. 6B). The second strongest peak at 1398 cm^{-1} was assigned to the νC–C breathing vibration of the quinolone ring system (Fig. 6B) and is also supplemental for levofloxacin identification.[69,70]

A series of aqueous solutions of levofloxacin with concentrations in the range of 1 μM to 1 mM were prepared in order to

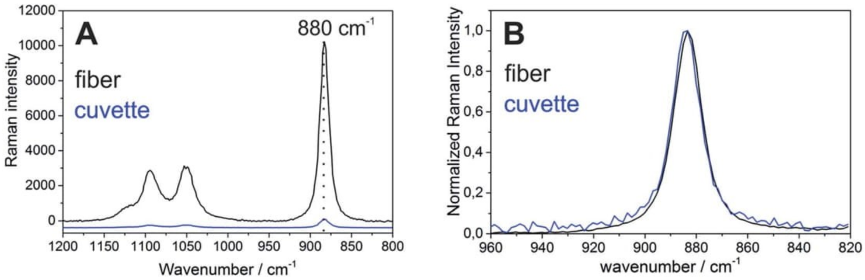

Fig. 4 Comparison of the Raman spectra of an ethanol–water mixture in a conventional cuvette measurement (blue) with a fiber enhanced measurement (black). The water background is subtracted and the spectra are slightly shifted for better visibility. (A) The Raman peak of ethanol at 880 cm^{-1} has a 52× higher intensity in the fiber enhanced spectrum compared to the conventional cuvette measurement. (B) The signal-to-noise ratio of the normalized Raman peak of ethanol in the fiber enhanced measurements is one order of magnitude higher compared to conventional cuvette experiments.

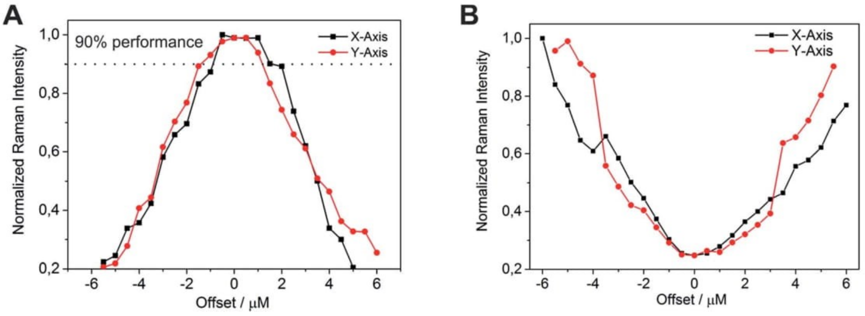

Fig. 5 Analysis of the coupling position of the sensor fiber. (A) The height of the Raman peak of ethanol at 880 cm^{-1} was measured with lateral offsets relative to the optimized coupling position. The analysis shows that the Raman signals maintain 90% peak intensity within ±1.5 µm of lateral offset and strongly decrease for higher lateral misalignments. (B) The background Raman signal of the fiber silica material (normalized Raman peak intensity at 490 cm^{-1}) increases for a misalignment of the lateral coupling position and thus causes an increase of the noise level.

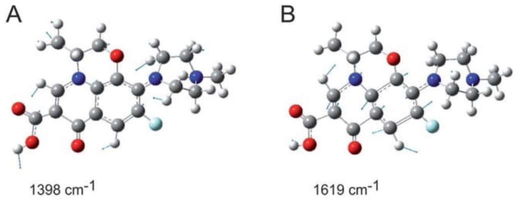

Fig. 6 Assignment of the vibrational modes of levofloxacin that were used as Raman marker bands for quantification. The atomic displacements of the associated vibrational modes are given for the Raman peaks at 1398 cm^{-1} (A) and 1629 cm^{-1} (B).

quantify the limit of detection of the drug detection and to evaluate the linearity of the measurements. The Raman spectra with a conventional cuvette and the sensor fiber were compared with identical experimental settings. The Raman signal intensity was derived from the height of the Lorentzian fit of the Raman peak at 1619 cm^{-1} and the noise was calculated from the root-mean-square (RMS) values of the baseline. The comparison of the conventional Raman spectrum and the fiber enhanced Raman spectrum of a 0.5 mM solution of levofloxacin (Fig. 7A) nicely demonstrated a more than one order of magnitude increased SNR in the measurements with the sensor fiber. The limit-of-detection (LOD) of levofloxacin was strongly improved down to a concentration of 20 µM. The Raman intensities of the levofloxacin peak show an excellent linearity to the analyte concentration in the series of measurements (Fig. 7B). The improved sensitivity of the measurements with the sensor fiber is clearly seen in the steeper slope of the linear fit (Fig. 7B). Extremely low concentrations of levofloxacin can still be quantified in fiber enhanced experiments that are not accessible anymore in the conventional measurements (Fig. 7B). The excellent linearity provides a robust calibration function for the quantification of unknown concentrations of levofloxacin, based on the intensity of the Raman marker peak.

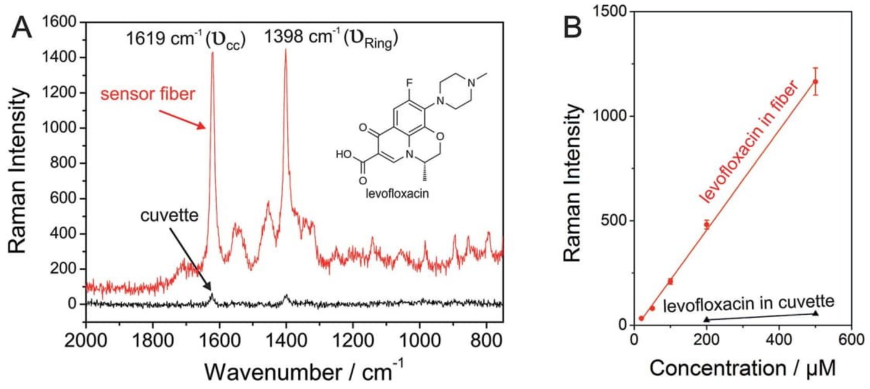

Fig. 7 Comparison of conventional and fiber enhanced Raman measurements of levofloxacin. (A) The peaks in the fiber enhanced Raman spectrum (red) show higher intensities compared to the conventional spectrum (black) of a solution of levofloxacin with a concentration of 0.5 mM ($I_{\text{Laser}} = 100$ mW). (B) The Raman peak intensities of levofloxacin show excellent linearity to the analyte concentration.

Conclusion

The abilities of fiber enhanced Raman spectroscopy with elaborated hollow core photonic crystal fibers were evaluated for sensing antibiotic drugs in aqueous solutions. These innovative all silica fibers outperform conventional polymer fibers in their optical quality. In order to provide a highly efficient sensor fiber for Raman sensing, the bandgap of the HC-PCF was shifted into the important visible range. The sensor fiber provided a spectral window for low loss light guidance for a complete Raman spectrum up to 4000 cm^{-1} with $\lambda_{\mathrm{exc}} = 532$ nm. Such a waveguide enables an extremely strong light–analyte interaction within the liquid filled fiber core and thus provides a highly increased analytical sensitivity. The fiber itself is also used as a miniaturized sample container. It was shown that a precise optical coupling must be guaranteed with a lateral misalignment of less than ±1.5 μm. This coupling precision should also be achieved in envisioned miniaturized setups for clinical use, in order to provide strong analyte signals and to avoid background noise.

Considering these requirements, it was possible to improve the limit-of-detection for the frequently used broad spectrum antibiotic levofloxacin down to clinically relevant concentrations of 20 μM with only 8 nL sample volume in the fiber core. Thus, fiber enhanced Raman spectroscopy has great potential for chemical selective and ultrasensitive monitoring of levofloxacin levels rapidly, minimal invasive, and individually for every intensive care patient. This proof of principle study will be extended in clinical settings.

Conflicts of interest

The authors declare no conflict of interest.

Acknowledgements

Funding from the Federal state of Thuringia (2015 FE 9012 and 2015 FGI 0011), the European Union (EFRE), and the German Ministry of Education and Research (01KI1501 and 01EO1502) is gratefully acknowledged.

References

1 G. P. Patel and R. A. Balk, *Am. J. Respir. Crit. Care Med.*, 2012, **185**, 133–139.
2 A. Kumar, D. Roberts, K. E. Wood, B. Light, J. E. Parrillo, S. Sharma, R. Suppes, D. Feinstein, S. Zanotti, L. Taiberg, D. Gurka, A. Kumar and M. Cheang, *Crit. Care Med.*, 2006, **34**, 1589–1596.
3 F. J. G. de Molina and R. Ferrer, *Crit. Care*, 2011, **15**, 175.
4 F. S. Taccone, P. F. Laterre, T. Dugernier, H. Spapen, I. Delattre, X. Wittebole, D. De Backer, B. Layeux, P. Wallemacq, J. L. Vincent and F. Jacobs, *Crit. Care*, 2010, **14**, R126.
5 M. W. Pletz, F. Bloos, O. Burkhardt, F. M. Brunkhorst, S. M. Bode-Boger, J. Martens-Lobenhoffer, M. W. Greer, H. Stass and T. Welte, *Intensive Care Med.*, 2010, **36**, 979–983.
6 F. Pea, P. Viale and M. Furlanut, *Clin. Pharmacokinet.*, 2005, **44**, 1009–1034.
7 T. F. Barlam, S. E. Cosgrove, L. M. Abbo, C. MacDougall, A. N. Schuetz, E. J. Septimus, A. Srinivasan, T. H. Dellit, Y. T. Falck-Ytter, N. O. Fishman, C. W. Hamilton, T. C. Jenkins, P. A. Lipsett, P. N. Malani, L. S. May, G. J. Moran, M. M. Neuhauser, J. G. Newland, C. A. Ohl, M. H. Samore, S. K. Seo and K. K. Trivedi, *Clin. Infect. Dis.*, 2016, **62**, e51–e77.
8 T. Steinmetz, N. Eliakim-Raz, E. Goldberg, L. Leibovici and D. Yahav, *Clin. Microbiol. Infect.*, 2015, **21**, 665–673.
9 P. F. Troke, H. P. Hockey and W. W. Hope, *Antimicrob. Agents Chemother.*, 2011, **55**, 4782–4788.
10 K. Vishwanathan, M. G. Bartlett and J. T. Stewart, *J. Pharm. Biomed. Anal.*, 2002, **30**, 961–968.
11 T. Lemoine, D. Breilh, D. Ducint, J. Dubrez, J. Jougon, J. F. Velly and M. C. Saux, *J. Chromatogr. B: Biomed. Sci. Appl.*, 2000, **742**, 247–254.
12 J. Vella, F. Busuttil, N. S. Bartolo, C. Sammut, V. Ferrito, A. Serracino-Inglott, L. M. Azzopardi and G. LaFerla, *J. Chromatogr. B: Anal. Technol. Biomed. Life Sci.*, 2015, **989**, 80–85.
13 A. Ebers, S. Stroup, S. Mpagama, R. Kisonga, I. Lekule, J. Liu and S. Heysell, *PLoS One*, 2017, **12**, e0170663.
14 H. W. Sun and Y. L. Zuo, *Curr. Anal. Chem.*, 2013, **9**, 157–162.
15 M. Brueckner, K. Becker, J. Popp and T. Frosch, *Anal. Chim. Acta*, 2015, **894**, 76–84.
16 T. Frosch and J. Popp, *J. Biomed. Opt.*, 2010, **15**, 041516.
17 T. Frosch and J. Popp, *J. Mol. Struct.*, 2009, **924–926**, 301–308.
18 T. Jochum, B. Michalzik, A. Bachmann, J. Popp and T. Frosch, *Analyst*, 2015, **140**, 3143–3149.
19 T. Frosch, K. L. Chan, H. C. Wong, J. T. Cabral and S. G. Kazarian, *Langmuir*, 2010, **26**, 19027–19032.
20 R. Domes, C. Domes, C. R. Albert, G. Bringmann, J. Popp and T. Frosch, *Phys. Chem. Chem. Phys.*, 2017, **19**, 29918–29926.
21 R. Keiner, M. Herrmann, K. Kuesel, J. Popp and T. Frosch, *Anal. Chim. Acta*, 2015, **864**, 39–47.
22 T. Jochum, J. C. von Fischer, S. Trumbore, J. Popp and T. Frosch, *Anal. Chem.*, 2015, **87**, 11137–11142.
23 R. Keiner, M. C. Gruselle, B. Michalzik, J. Popp and T. Frosch, *Anal. Bioanal. Chem.*, 2015, **407**, 1813–1817.
24 D. Yan, J. Popp and T. Frosch, *Anal. Chem.*, 2017, **89**, 12269–12275.
25 R. Keiner, T. Frosch, T. Massad, S. Trumbore and J. Popp, *Analyst*, 2014, **139**, 3879–3884.
26 T. Jochum, A. Fastnacht, S. E. Trumbore, J. Popp and T. Frosch, *Anal. Chem.*, 2017, **89**, 1117–1122.
27 S. Hanf, S. Fischer, H. Hartmann, R. Keiner, S. Trumbore, J. Popp and T. Frosch, *Analyst*, 2015, **140**, 4473–4481.
28 T. Frosch, R. Keiner, B. Michalzik, B. Fischer and J. Popp, *Anal. Chem.*, 2013, **85**, 1295–1299.
29 A. Sieburg, T. Jochum, S. E. Trumbore, J. Popp and T. Frosch, *Analyst*, 2017, **142**, 3360–3369.
30 T. Frosch, T. Meyer, M. Schmitt and J. Popp, *Anal. Chem.*, 2007, **79**, 6159–6166.
31 P. Russell, *Science*, 2003, **299**, 358–362.
32 A. Hartung, J. Kobelke, A. Schwuchow, J. Bierlich, J. Popp, M. A. Schmidt and T. Frosch, *Opt. Lett.*, 2015, **40**, 3432–3435.

7.4. Fiber-Enhanced Raman Multigas Spectroscopy: A Versatile Tool for Environmental Gas Sensing and Breath Analysis

Reproduced from Hanf, S.; Keiner, R.; Yan, D.; Popp, J.; Frosch, T., Fiber-enhanced Raman multigas spectroscopy: a versatile tool for environmental gas sensing and breath analysis. Anal. Chem. 2014, 86 (11), 5278-85 with permission from American Chemical Society.

analytical chemistry

Article

pubs.acs.org/ac

Fiber-Enhanced Raman Multigas Spectroscopy: A Versatile Tool for Environmental Gas Sensing and Breath Analysis

Stefan Hanf,[†] Robert Keiner,[†] Di Yan,[†] Jürgen Popp,[†,‡,§] and Torsten Frosch*[,†,‡]

[†]Leibniz Institute of Photonic Technology, Jena, Germany
[‡]Institute for Physical Chemistry, Friedrich-Schiller University, Jena, Germany
[§]Abbe School of Photonics, Friedrich-Schiller University, Jena, Germany

Supporting Information

ABSTRACT: Versatile multigas analysis bears high potential for environmental sensing of climate relevant gases and noninvasive early stage diagnosis of disease states in human breath. In this contribution, a fiber-enhanced Raman spectroscopic (FERS) analysis of a suite of climate relevant atmospheric gases is presented, which allowed for reliable quantification of CH_4, CO_2, and N_2O alongside N_2 and O_2 with just one single measurement. A highly improved analytical sensitivity was achieved, down to a sub-parts per million limit of detection with a high dynamic range of 6 orders of magnitude and within a second measurement time. The high potential of FERS for the detection of disease markers was demonstrated with the analysis of 27 nL of exhaled human breath. The natural isotopes $^{13}CO_2$ and $^{14}N^{15}N$ were quantified at low levels, simultaneously with the major breath components N_2, O_2, and $^{12}CO_2$. The natural abundances of $^{13}CO_2$ and $^{14}N^{15}N$ were experimentally quantified in very good agreement to theoretical values. A fiber adapter assembly and gas filling setup was designed for rapid and automated analysis of multigas compositions and their fluctuations within seconds and without the need for optical readjustment of the sensor arrangement. On the basis of the abilities of such miniaturized FERS system, we expect high potential for the diagnosis of clinically administered ^{13}C-labeled CO_2 in human breath and also foresee high impact for disease detection via biologically vital nitrogen compounds.

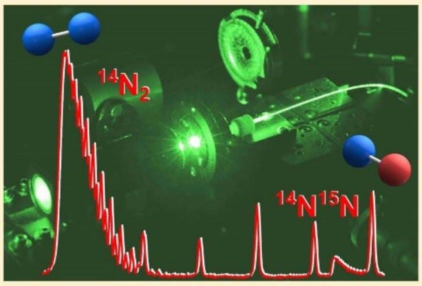

Human breath analysis bears great potential for noninvasive early stage monitoring of disease states.[1] Breath analysis is highly accepted by patients and enables rapid diagnosis and continuous bedside observation of intensive care patients. Human breath is a mixture of different major compounds like N_2, O_2, CO_2, and H_2O and traces of volatile organic compounds (VOC). The simultaneous quantification of a whole suite of gaseous components in combination with chemometric analysis yields high diagnostic potential.[2] One of the major challenges is the accurate quantification of many gases in different concentration ranges simultaneously. Important gaseous markers for the detection of lung cancer are acetone (C_3H_6O) and methane (CH_4), along with H_2, CO, CO_2, and NH_3.[3] Other important diseases and their marker gases include (mitochondrial) oxidative stress (CO),[4] colonic fermentation (CH_4, H_2),[5] and *Helicobacter pylori* infection (NH_3, $^{12}CO_2$)[6] with diagnosis by means of isotopic-labeled $^{13}CO_2$.[7]

In the field of environmental gas sensing, it is important to trace climate relevant atmospheric gases (e.g., CH_4, CO_2, N_2O, N_2, and O_2), which are also strongly influenced by microbial activities in soil.[8] Temperate forest soils, for example, have been identified as significant sinks for CH_4 and as sources for NO, CO_2, and N_2O,[9] while wetlands are a major source of CH_4.[10] Methane is an important greenhouse gas, whose global warming potential is 25 times higher than that of CO_2.[11] The excessive production of N_2O, another potent greenhouse gas, contributes to catalytic stratospheric ozone destruction.[11] The annual increase of atmospheric N_2O is also a consequence of microbial denitrification by heterotrophic bacteria (e.g., *Pseudomonas*) as well as autotrophic denitrifiers.[12] The monitoring of multigas exchanges is thus of significant importance for an understanding of the dynamic interactions between soil, microbes, and plants in climate-sensitive ecosystems.[13]

Due to the low concentrations and diversity of the complex composition of atmospheric gases and the gas markers in breath samples, the gas analysis demands highly selective and sensitive methods. The most commonly used technique for selective quantification of simple gases is mass spectrometry, which is often coupled to gas chromatography for the separation of larger molecules.[14] Although mass spectrometry is an accurate and sensitive technique, capable of fast and simultaneous monitoring of some simple gases,[15] this technique is bulky, expensive, difficult to calibrate, and limited for miniaturization. Methods based on infrared (IR) absorption spectroscopy, such

Received: December 22, 2013
Accepted: May 8, 2014
Published: May 20, 2014

as cavity ring-down spectroscopy (CRDS)[16] and photoacoustic spectroscopy,[17] provide high sensitivity for the analysis of molecules with strong dipole moment (e.g., the atmospheric gases CO_2, CH_4, and N_2O) but cannot be applied for the detection of important homonuclear diatomic gases (e.g., H_2, O_2, and N_2).[18]

Raman spectroscopy,[19] a technique based on molecular vibrations,[20] is well-suited for selective multigas detection and considered as a potential technique for human breath analysis[21] and environmental gas sensing.[22] An advantage of using Raman spectroscopy for gas sensing is the ability for simultaneous identification of all gases (except noble gases) and volatiles, in a wide range of concentrations, within a complex mixture of gases.[22] Raman gas analysis is very fast, nonconsumptive, requires no labeling or sample preparation, and also enables the detection of homonuclear diatomic gases (N_2, O_2, and H_2). The simultaneous quantification of isotopic-labeled gases[23] (e.g., $^{13}CO_2$, $^{15}N_2$) provides a capability for tracer experiments. All gases can be quantified with help of their specific Raman bands and also a priori unexpected gases can easily be identified in the Raman spectra of complex multigas-compositions, in contrast to simple gas sensors that must be calibrated for all expected gases.[18] Thus, Raman multigas sensing is a powerful technique but is not yet established in medical breath diagnosis due to the low sensitivity of the Raman scattering process.

A promising approach for the enhancement of the intrinsically weak Raman signals is the improvement of the interaction of the laser light with the analyte molecules within hollow-core optical waveguides.[24] Gas sensors based on simple capillaries or hollow metal waveguides are already known[25] but suffer from high attenuation. Hollow-core photonic crystal fibers (HC-PCF)[26] can guide the light with low attenuation within a spectral bandgap and have recently emerged as a promising tool which could be exploited for sensitive gas analysis.[27] The light within a photonic crystal fiber is guided at a low-index defect within a quasi-2D photonic crystal lattice, forming the fiber cladding. The guided wavevectors are surrounded by propagation modes with a higher and lower propagation constant β. For higher vacuum wavevectors k than β, bandgaps appear which trap the light within the inner hollow core. This leads to broad spectral transmission windows for the laser light and the Raman-scattered photons. The HC-PCF confines both, the optical field and the gaseous analyte, within a micrometer-sized central hollow core of an elaborate microstructure. Only small sample volumes (~nanoliters per centimeter fiber length) are needed, and long optical interaction lengths are achieved for highly efficient interaction of light and gas molecules and thus provide enhanced analytical sensitivity.

■ METHODS AND MATERIAL

HC-PCF Based Setup for Raman Gas Sensing. The scattering cross section of the Raman effect is very low (around 10^{-23} cm^2/sr).[28] This drawback can be circumvented with an advanced experimental setup. Several parameters can be exploited to increase the amount of Raman scattered light and therefore improve the limit of detection (LOD). The Raman scattering intensity can be expressed by the simplified equation[29,30]

$$I_R(\tilde{\nu}_R, \tilde{\nu}_0) = \eta I_0 n \left(\frac{d\sigma(\tilde{\nu}_R, \tilde{\nu}_0)}{d\Omega} \right) \Omega L_e \tag{1}$$

In this equation, I_0 represents the intensity of exciting laser, I_R the intensity of the Raman scattered light, n the molecule density of the measured gas (parts per cm^{-3}), and $(d\sigma)/(d\Omega)$ the absolute differential Raman scattering cross section (in centimeters squared per steradian). The factor η represents the detection efficiency of the experimental setup [accounting, for example, for the signal collection and optical fiber coupling efficiency, the quality of the optical components (mirrors, filters, gratings efficiencies, etc.), and the quantum efficiency of the detector]. Ω (in steradian) is the solid angle of the signal collection optic. The effective length L_e with $L_e = (1 - e^{-(\alpha_L - \alpha_R)L})/(\alpha_L + \alpha_R)$ describes the improved interaction lengths in fiber sensing with backscattering geometry, where α_L and α_R (in inverse meters) represent the attenuation of the excitation laser light and the Raman signal at a specific wavelength. A linear relationship appears between the Raman scattered signal and the laser intensity as well as the particle density of the gas (eq 1). The particle density (n) is proportional to the pressure and temperature according to the ideal gas law.

A Raman fiber-setup with detection in the visible range combines several advantages: availability of compact, high power lasers with excellent beam quality, detectors with high quantum efficiency and low noise, and high-quality gratings, mirrors, filters, and objectives.

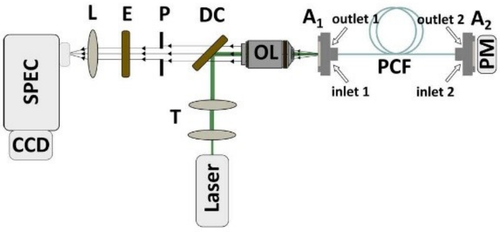

Figure 1. Design of the optical setup for fiber-enhanced Raman spectroscopy (FERS) consisting of laser, telescope (T), long-pass dichroic beam splitter (DC), objective lens (OL), fiber adapter assembly (A1 and A2), hollow-core photonic crystal fiber (PCF), powermeter (PM), pinhole (P), edge filter (E), aspheric lens (L), spectrometer (SPEC), and CCD detector.

The optical design of the HC-PCF-based Raman gas-sensing setup is schematically shown in Figure 1A. A frequency-doubled Nd:YAG laser (with λ_L = 532.2 nm, I_L = 3.2 W, and $M^2 < 1.1$) from Laser Quantum is applied. The beam passes a telescope (T) to increase the beam diameter and matches the NA of the fiber. The laser light is reflected into a plan fluorite objective lens (OL) 20×/0.5 (Olympus) via a dichroic beam splitter (DC) with edge at 532 nm, providing a reflectivity of 98% for s-polarized laser light. The focused beam is coupled into a 1 m HC-PCF (HC580-02) with a central transmission wavelength of 580 nm via a three-axis nanopositioning stage (A). The core diameter of the applied HC-PCF is about 7 μm and most of the laser power is focused well within the center of the fiber core. The fiber provides an optical bandgap with a minimal attenuation at 580 nm and a spectral range from 532−633 nm, such that the excitation wavelength λ = 532 nm lies at the low wavelength edge of the bandgap and a spectral region of more than 3000 cm^{-1} can be guided with extremely low attenuation (Figure S1 of the Supporting Information), which also includes the vibrational stretching mode of CH_4 at 2917

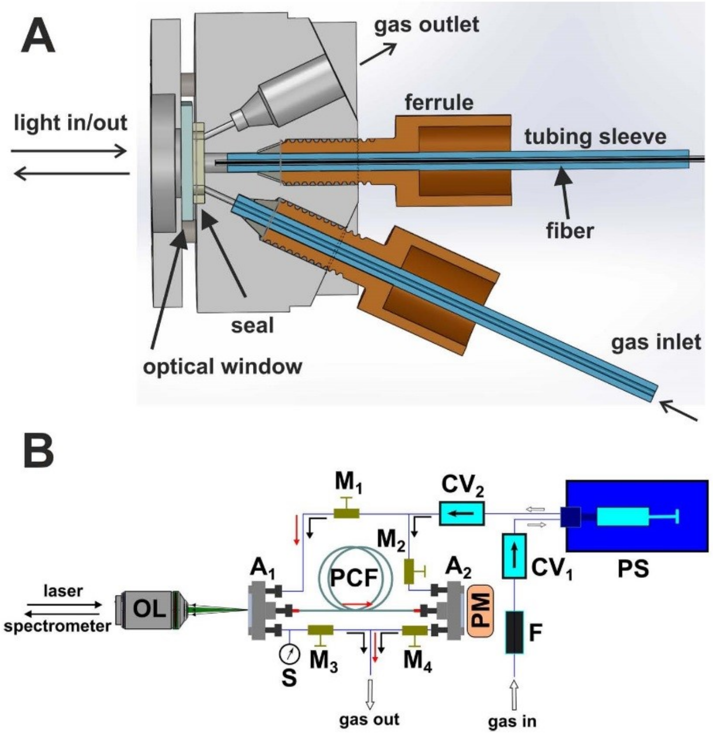

Figure 2. (A) Schematic illustration of the fiber adapter assembly for the alignment-free optical coupling and gas filling of the HC-PCF. The assembly consist of ferrules and tubing sleeves for the mounting of the HC-PCF (middle) and HPLC tubing for gas inlet and outlet (bottom and top). The laser is coupled through an optical window into the HC-PCF, and the Raman signal is collected in backscattering geometry. (B) Sketch of the setup for fast and precise filling of the HC-PCF with gas mixtures consisting of midpressure pump system (PS), fiber adapter assemblies (A_1 and A_2, see Figure 2A), check valves (CV), magnetic valves (M), powermeter (PM), hollow-core photonic crystal fiber (PCF), objective lens 20×/0.5 (OL), sensor for pressure and temperature (S), and sinter filter (F).

cm^{-1}. The transmission spectrum of the fiber is insensitive to bending, which is important for quantification, setup stability, and miniaturization.

The backscattered red-shifted Raman signal passes the dichroic mirror (DC) and edge filter (E) where the Rayleigh signal is suppressed. This backscattered light is then focused by a 75 mm achromatic lens (L) on the slit of the spectrometer (Acton 2556 with LN_2-cooled back-illuminated CCD detector). The whole collection setup magnifies the 7 μm core-diameter at the fiber exit to an approximately 60 μm diameter spot size with NA of 0.05 on the slit plane of the spectrometer in order to match the collection NA and achieve optimal etendue. The inelastically scattered photons are detected via a liquid nitrogen cooled CCD. Three gratings in the spectrometer allow overview measurements (grating with 600 lines/millimeter, which provides a resolution of 0.10 nm/pixel; equal to 3.5 cm^{-1}/pixel at 557.03 nm) and high-resolved measurements [gratings with 1800 (2400) lines/mm, with resolutions of 0.03 (0.024) nm/pixel; equal to 1.0 (0.78) cm^{-1}/pixel at 557.03 nm respectively] An additional spatial filter, consisting of a pinhole (P), is inserted between the dichroic beam splitter (DC) and edge filter (E) to suppress the Raman signal from the silica of the fiber cladding such that the Raman signal of the gas samples is not attenuated and has optimal signal-to-noise ratio (SNR).

■ RESULTS AND DISCUSSION

Reproducible Optical Coupling of the Sensor-Fiber for Reliable, Quantitative FERS Gas Analysis. High stability of the optical coupling is essential for reliable gas quantification and was achieved by specially designed fiber adapter assemblies (Figures 1 and 2). The adapters (A1 and A2) at each end of the fiber solve several crucial tasks at once: laser coupling and collection of the Raman-scattered light through an optical window, collection of the transmitted light for permanent monitoring with a power meter (PM), and fast and reproducible flushing of the fiber with gas analytes. Each adapter consists of a fitting for the fiber, while entrance and exit ports enable gas flow and flushing (Figure 2A). The adapter was designed for low working distances between the microscope objective and fiber end facet down to 3 mm to increase the possible choice of high-NA microscope objectives. The sealing and optical window enables a pressure tight volume for fiber pressures up to 20 bar. The minimized dead volume within each adapter assembly is less than 100 nL. The two-way gas flow for each adapter enables fast flushing of the dead

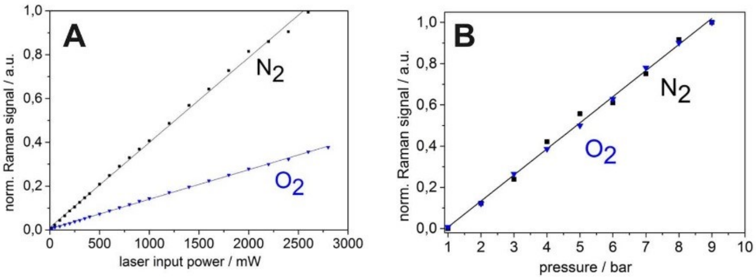

Figure 3. (A) Demonstration of the excellent linearity and scalability of the fiber-enhanced Raman signals of gaseous nitrogen and oxygen with rising laser powers (peak areas at 2331 and 1555 cm^{-1} were fitted and integrated, respectively). (B) Linearly increasing peak areas of the nitrogen and oxygen Raman signals are shown for linearly rising (absolute) gas pressure.

volume and fiber fillings within seconds for moderate gas pressures. The fast gas filling of the fiber-sensor is essential for fast FERS monitoring of changing gas concentrations and was achieved with a syringe pump system (PS), which is capable of increasing the pressure up to 20 bar in the fiber (Figure 2B). The gas mixture passes first a sinter filter (F) with a pore size of 0.5 μm, is then filled in the syringe, and afterward the dead volume of the setup gets flushed with gas (while all magnetic valves M_1−M_4 are opened and the gas flow follows the direction of the black arrows in Figure 2B). Second, the magnetic valves M_2 and M_3 are closed, and the analyte gas passes exclusively through the hollow fiber (red arrows in Figure 2B). All magnetic valves (M_1−M_4) are closed prior to quantitative FERS measurements to ensure constant pressure within the fiber. The whole measurement procedure is fully automated by a LabView (National Instruments) routine, which reads and controls magnetic valves, pump system, power meter, and spectrometer. In doing so, it is possible to perform a rapid measurement, including fast gas filling, Raman analysis, new gas filling, etc. and thus to follow the concentration changes of a complex multigas mixture within seconds and without the need for optical readjustment of the backscattering arrangement.

For online quantification of the concentrations of the individual gases in a gas mixture, the Raman spectra of gases were taken for known concentration, pressure, temperature, exposure time, laser power, transmitted power, and fiber length and were saved as calibration files in the Labview routine. This calibration is very robust due to the linearity between gas concentration and laser intensity and Raman intensity (eq 1). Thus, higher sensitivities can be achieved for the analysis of minor gas compounds by controlled adjustment of the laser power and gas pressure. An excellent linearity between laser intensity and pressure as well as Raman intensity of N_2 and O_2 was shown with laser powers up to 2.8 W (Figure 3A) and pressures up to 9 bar (Figure 3B), which provides a substantial increase in sensitivity by 2 orders of magnitude compared to conventional parameters.

Fiber-Enhanced Raman Analysis of Environmentally Relevant Multigas Compositions. The simultaneous quantification of the climate relevant gases CH_4, CO_2, N_2O, N_2, and O_2 as well as their fluctuations is of high interest for ecosystem characterization as explained in the introduction. Thus, a mixture of these five important biogenic gases was analyzed in order to demonstrate the analytical abilities of the new FERS-setup. The high specificity and reliability of the method is demonstrated in the Raman spectrum of a defined mixture of CH_4, CO_2, N_2O, N_2, and O_2 (Figure 4) with precisely defined concentrations (Table 1). All five gases show Raman peaks within the spectral bandgap of about 3100 cm^{-1}, provided by the HC-PCF (Figure S1 of the Supporting Information), and can easily be separated from each other. A calibration of the setup was performed by measurements of the individual pure gas components with known concentration, at

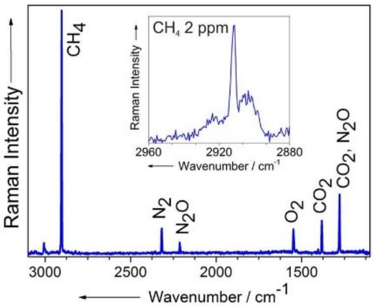

Figure 4. Fiber-enhanced Raman spectrum of a biogenic multigas composition, consisting of climate relevant gases CO_2, CH_4, and N_2O together with N_2, O_2 (each ~1 vol %, in Raman inactive argon carrier gas), which was acquired with one single measurement within a 40 ms acquisition time. All gases are spectrally well-separated from each other and can easily be quantified simultaneously. The inset shows a separate measurement, the fiber-enhanced Raman spectrum of naturally concentrated CH_4 at 2 ppm in air with SNR = 28 and thus sub-ppm LOD.

Table 1. Comparison of the Quantitative FERS Multi-Gas Measurement and the Certified Values of the Multi-Component Reference Gas from Linde AG (Prepared in Compliance with DIN EN ISO 6141)

gas component	certified concentrations (%)	measured Raman concentrations (%)	deviation absolute (%)
N_2	1.12	1.15	0.03
O_2	0.915	1.01	0.095
CO_2	1.02	1.10	0.08
N_2O	0.985	0.870	0.115
CH_4	1.08	1.00	−0.08

constant pressure, temperature, fiber length, and laser power (as explained before).

The experimentally obtained concentrations of the five biogenic gases were in very good agreement with the specified concentrations of the certified reference gas composition. The deviations of the Raman quantification of the gases N_2, O_2, CO_2, and CH_4 from the certified values were below 0.1%. The deviation of N_2O was slightly higher (0.115%) due to the small relative scattering cross section of the symmetric valence vibration between the N atoms in N_2O of around 0.51[31] (the N_2O Raman peak at 2224 cm^{-1} was preferred for the measurements because it did not superimpose with Raman peaks from other components). All data are summarized in Table 1.

The absolute sensitivity of the FERS analysis of all five biogenic gases (at pressure 20 bar and laser power 2 W) is shown in Table 2. The sensitivities for the individual gases scale with their absolute scattering cross section, which is particularly high for the four times degenerated vibration of methane. In order to demonstrate the high sensitivity of the new setup, CH_4 was analyzed at atmospheric concentration of 2 ppm, with SNR of 28 and, accordingly, an LOD of 0.22 ppm (inset in Figure 4 and Table 2).

Table 2. Overview of Raman shifts, Relative Raman Scattering Cross Sections Normalized to the Cross Section of Nitrogen, and Achieved Limits of Detection for the Multiple Biogenic Gases

component	Raman shift (cm^{-1})	relative Raman scattering cross section at 532 nm[31]	LOD (ppm)
N_2	2331	1.0	**9**
O_2	1555	1.0	**8**
CO_2	1388	1.1	**4**
N_2O	2224	0.5	**19**
CH_4	2917	8.6	**0.2**

The achieved low LOD values prove that fiber-enhanced Raman gas spectrometry is an extremely capable technique for simultaneous quantification of the climate relevant gases CH_4, CO_2, and N_2O alongside with the major biogenic gases N_2 and O_2.

Fiber-Enhanced Raman Analysis of Human Breath. In order to demonstrate the potential of fiber-enhanced Raman spectroscopy for simultaneous detection of disease markers in breath gas analysis, the Raman spectrum of 27 nL exhaled human breath was analyzed within the hollow fiber (Figure 5). The typical concentrations of endogenous breath molecules are given in Table 3. The Raman peaks of the major breath components $^{14}N_2$, $^{16}O_2$, and $^{12}CO_2$ can be found at 2331, 1555, 1388, and 1285 cm^{-1}, respectively. Minor gases that appear in the lower ppm range are highly interesting for clinical diagnosis of metabolic diseases and thus it is very promising that the natural isotopes $^{14}N^{15}N$ (inset Figure 5) and $^{13}CO_2$ could also be quantified in the Raman spectrum of the breath sample.

The experimentally derived concentrations of the different gas component of the human breath sample were in very good agreement with literature values[31] (Table 3). It should be emphasized that minor components at low concentrations (e.g., 400 ppm of the natural stable isotopic $^{13}CO_2$) were quantified simultaneously with major components (e.g., 77.8% for N_2) with just one single measurement. The result highlights the high dynamic range of about 4 orders of magnitude in this fiber-enhanced Raman gas analysis. These results are very promising because ^{13}C-labeled markers are successfully applied in breath analysis for the detection of different metabolic disorders, whereas the ^{15}N-tracer technique is not yet commonly applied in breath gas diagnosis. Besides the ability for the quantification of the low concentrated stable isotopes $^{14}N^{15}N$ and $^{13}CO_2$, the hollow fiber also provides a miniaturized sample container for the analysis of very small breath sample volumes of some tens of nanoliters.

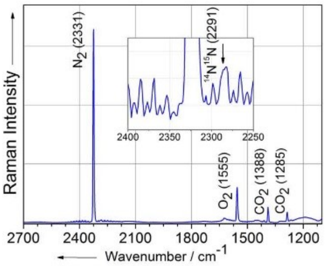

Figure 5. Fiber-enhanced Raman spectrum of 27 nL of exhaled human breath, which shows N_2, O_2, and CO_2 as the permanent gases in breath. The inset zooms the $^{14}N^{15}N$ natural isotope peak out, which superimposes with the *O*-branch of $^{14}N_2$.

Table 3. FERS Quantification of $^{14}N_2$, $^{16}O_2$, $^{12}CO_2$, $^{13}CO_2$, and $^{14}N^{15}N$ within Human Breath and Comparison with Literature Values.[31][a]

component	theoretical concentration in %	measured concentration in %	relative scattering cross section
$^{14}N_2$	78	77.8	1.00
$^{16}O_2$	16–17	16.0	1.02
$^{12}CO_2$	3–4	4.4	1.1 (1388)
$^{13}CO_2$	0.033–0.044	0.04	1.13 (1370)
$^{14}N^{15}N$	0.58	0.60	1.00

[a] The cross sections of the vibrational Raman transitions of different molecular components in human breath are given.

Highly Resolved FERS of Isotopic-Labeled Gases. In order to demonstrate the unique capabilities of FERS for selective and quantitative isotope gas analysis in a high dynamic range, a high-resolution FERS analysis on natural CO_2 and N_2 was performed, including all their natural isotopes (Figure 6).

The diagnosis of clinically administered ^{13}C-labeled CO_2 in human breath requires the selective identification of the label on a huge background of naturally exhaled CO_2, including its natural isotopes. Obviously it is an essential prerequisite, for medical gas diagnosis of administered ^{13}C-label in breath, to perform a thorough analysis of the content of natural CO_2 isotopes and to develop a reliable technique for their quantification. Thus, a fiber-enhanced Raman spectrum of CO_2 was acquired (Figure 6A), which shows the typical Fermi dyad[32] of the major natural isotope $^{12}C^{16}O_2$. The sharp Q-branches of the $\tilde{\nu}_1$ and $2\tilde{\nu}_2$ bands of $^{12}C^{16}O_2$ result from the coupling of the fundamental symmetric stretching mode $\tilde{\nu}_1$ at 1286 cm^{-1} and the first overtone of the bending mode $2\tilde{\nu}_2$ at 1388 cm^{-1}. The dyad is often simply assigned with $\tilde{\nu}_-$ and $\tilde{\nu}_+$ for the lower and higher wavenumber, respectively. The measured hot bands for $^{12}C^{16}O_2$ occur at wavenumbers 1410 cm^{-1} ($\tilde{\nu}_+^{(1)}$) and 1265 cm^{-1} ($\tilde{\nu}_-^{(1)}$), shifted relative to the fundamental bands[32] (Figure 6A). The Fermi dyad of the

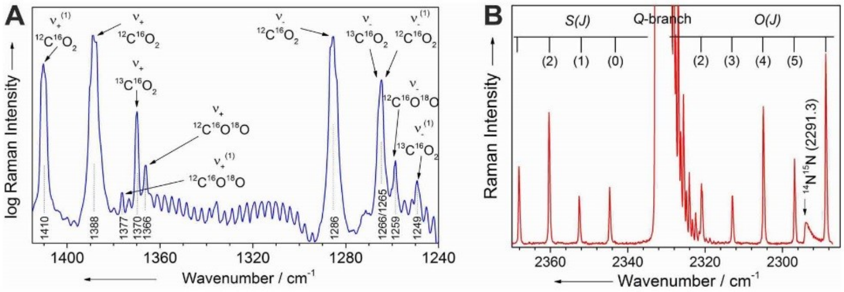

Figure 6. (A) Fiber-enhanced high-resolution Raman spectrum of pure CO_2. The spectrally resolved results show in detail the Fermi dyad of the different natural isotopes $^{12}C^{16}O_2$ ($\tilde{\nu}_+$ and $\tilde{\nu}_-$), $^{13}C^{16}O_2$ ($\tilde{\nu}_+$ and $\tilde{\nu}_-$), and $^{12}C^{16}O^{18}O$ ($\tilde{\nu}_+$ and $\tilde{\nu}_-$), respectively, as well as the hot bands of $^{12}C^{16}O_2$ ($\tilde{\nu}_+^{(1)}$ and $\tilde{\nu}_-^{(1)}$), $^{13}C^{16}O_2$ ($\tilde{\nu}_-^{(1)}$), and $^{12}C^{16}O^{18}O$ ($\tilde{\nu}_+^{(1)}$). (B) Fiber-enhanced high-resolution Raman spectrum of pure N_2. The ro-vibrational fine structure of the O- and S-branches next to the strong Q-branch is resolved, and the Raman peak of the $^{14}N^{15}N$ isotope is marked by an arrow.

isotope $^{13}C^{16}O_2$ occurs at lower wavenumbers, at 1370 cm^{-1} ($\tilde{\nu}_+$) and 1266 cm^{-1} ($\tilde{\nu}_-$) with the hot band at 1249 cm^{-1} ($\tilde{\nu}_-^{(1)}$). Even the bands of the isotope $^{12}C^{16}O^{18}O$ are detected at 1366 cm^{-1} ($\tilde{\nu}_+$) and 1259 cm^{-1} ($\tilde{\nu}_-$), respectively, as well as the hot band at 1377 cm^{-1} ($\tilde{\nu}_+^{(1)}$) and the ro-vibrational fine structure of CO_2 (Figure 6A). The natural abundance of ^{18}O and ^{13}C are 0.2% and 1.1% and result in a natural abundance of 1.09% for $^{13}C^{16}O_2$ and 0.39% for $^{12}C^{16}O^{18}O$ within the sum of all carbon dioxide isotopes.[33] For quantitative analysis, the peak area of $^{12}C^{16}O_2$ was integrated from 1385.6 to 1395.1 cm^{-1} and sums up to 150475 counts with a total peak height of 61968 counts and a baseline noise of about 27 counts (standard deviation of the baseline). The integration of the $^{13}C^{16}O_2$ peak from 1368.7−1375.9 cm^{-1} results in 1645 counts and a total peak height of 873 counts. From a comparison of both peaks, an absolute concentration of (1.08 ± 0.03)% was measured for the isotope $^{13}C^{16}O_2$, which is in very good agreement with the theoretical value of 1.09%.

The capability of FERS for highly sensitive quantification of N_2 alongside other biogenic gases and natural isotopes is unique. Natural nitrogen is contained to 78.01% absolute in ambient air (sum of all isotopes). The relative natural concentrations of the individual isotopes are 99.261% for $^{14}N_2$, 0.737% for $^{14}N^{15}N$, and 0.0001% for $^{15}N_2$.[33] The high-resolution FERS measurement of N_2 in ambient air at room temperature is dominated by the Q-branch of $^{14}N_2$ at 2329 cm^{-1} (Figure 6B). The spectrally resolved Q-branch shows the typical asymmetric shape due to different ro-vibrational energy levels with spacing, according to the model of the anharmonic oscillator.[34] The Q-branch is accompanied by O- and S-branches of the rotational transitions, which roughly extend from 2000 to 2600 cm^{-1}. The intensity alternations arise from the statistical weight of the nuclear spin states for even and odd J, with the relation 6:3 (with $J = 1$ for N_2).[29b] The Q-branch of the isotope $^{14}N^{15}N$ at position 2291 cm^{-1} was used to quantify the isotope abundance of $^{14}N^{15}N$ compared to $^{14}N_2$. The experimentally derived relative abundance of (0.0080 ± 0.0005) is in good agreement with the theoretically expected value of 0.0074.

The results highlight the high potential of fiber-enhanced Raman spectroscopy with hollow-core photonic crystal fibers as minimal volume cuvettes for quantitative analysis of isotopic tracers.

■ SUMMARY AND CONCLUSION

An advanced fiber-enhanced Raman spectroscopic (FERS) setup was presented with specially designed fiber adapter assemblies for stable and quantitative analysis and fully automated gas filling system for alignment-free and fast monitoring of multigas fluctuations down to sub-ppm levels, with a high dynamic range of 6 orders of magnitude, time resolution of seconds, and miniscule sample volumes of nanoliters. A simultaneous FERS quantification of the climate relevant gases CH_4, CO_2, and N_2O together with N_2 and O_2 was demonstrated, and limits of detection as low as 0.2 ppm for methane were achieved. The straightforward quantification of low concentrated homonuclear diatomic gases (e.g., N_2, O_2, and H_2) and chemically almost identical isotopes (e.g., $^{13}CO_2$, $^{12}CO_2$ as well as $^{14}N_2$, and $^{14}N^{15}N$) should be highlighted, since these gases cannot easily be quantified simultaneously with conventional techniques and the tracing of isotopic labels is of outmost importance for the monitoring of metabolic pathways.

The potential of FERS for early stage disease diagnostics was demonstrated with the analysis of 27 nL of exhaled human breath, and it was shown that the major breath components $^{14}N_2$, $^{16}O_2$, and $^{12}CO_2$ as well as the minor components $^{14}N^{15}N$ and $^{13}CO_2$ can be quantified simultaneously over a high dynamic range of 4 orders of magnitude with just one single measurement. While the ^{13}C breath test is already established in breath analysis, we expect that more ^{13}C-tests will be developed in the future based on reliable sensing with the new FERS technique and also foresee a high potential for disease detection via biologically vital nitrogen compounds. The determination of nitrogen ratios with FERS is much faster and simpler compared to complicated measurements with bulky and expensive analytical techniques such as isotope ratio mass spectrometry (IRMS).

Furthermore, there is great potential in the miniaturization of FERS setups with the advantage of high sensitivity and selectivity in combination with portability and affordable prices for such devices. A portable and robust FERS sensor, which is capable for real-time multicomponent quantification of biogenic gases, will be a powerful tool for the characterization of greenhouse gas fluxes and bedside clinical diagnosis of metabolic diseases.

■ ASSOCIATED CONTENT

Supporting Information

Additional information as noted in text. This material is available free of charge via the Internet at http://pubs.acs.org.

■ AUTHOR INFORMATION

Corresponding Author

*E-mail: torsten.frosch@uni-jena.de.

Notes

The authors declare no competing financial interest.

■ ACKNOWLEDGMENTS

Funding of the research project by the Free State of Thuringia (Germany) and the European Union (EFRE) is highly acknowledged (FKZ: 2012 FGR 0013). The authors thank the colleagues from the IPHT workshop for their help in the construction of the fiber adapter assembly. S.H. gratefully acknowledges support from the International Max-Planck Research School (IMPRS), “Global Biogeochemical Cycles”.

■ REFERENCES

(1) (a) Manolis, A. *Clin. Chem.* **1983**, *29* (1), 5−15. (b) Pleil, J. D.; Lindstrom, A. B. *Clin. Chem.* **1997**, *43* (5), 723−730. (c) Buszewski, B.; Kęsy, M.; Ligor, T.; Amann, A. *Biomed. Chromatogr.* **2007**, *21* (6), 553−566.

(2) (a) Hakim, M.; Broza, Y. Y.; Barash, O.; Peled, N.; Phillips, M.; Amann, A.; Haick, H. *Chem. Rev. (Washington, DC, U.S.)* **2012**, *112* (11), 5949−5966. (b) Peng, G.; Tisch, U.; Adams, O.; Hakim, M.; Shehada, N.; Broza, Y. Y.; Billan, S.; Abdah-Bortnyak, R.; Kuten, A.; Haick, H. *Nat. Nanotechnol.* **2009**, *4* (10), 669−673.

(3) (a) Houghton, A. M. *Nat. Rev. Cancer* **2013**, *13* (4), 233−245. (b) Bajtarevic, A.; Ager, C.; Pienz, M.; Klieber, M.; Schwarz, K.; Ligor, M.; Ligor, T.; Filipiak, W.; Denz, H.; Fiegl, M.; Hilbe, W.; Weiss, W.; Lukas, P.; Jamnig, H.; Hackl, M.; Haidenberger, A.; Buszewski, B.; Miekisch, W.; Schubert, J.; Amann, A. *BMC Cancer* **2009**, *9*, 348.

(4) Horvath, I.; Loukides, S.; Wodehouse, T.; Kharitonov, S. A.; Cole, P. J.; Barnes, P. J. *Thorax* **1998**, *53* (10), 867−870.

(5) (a) Olson, J. W.; Maier, R. J. *Science* **2002**, *298* (5599), 1788−1790. (b) Simren, M.; Stotzer, P. O. *Gut* **2006**, *55* (3), 297−303.

(6) (a) Marchetti, M.; Arico, B.; Burroni, D.; Figura, N.; Rappuoli, R.; Ghiara, P. *Science* **1995**, *267* (5204), 1655−1658. (b) Tummala, S.; Sheth, S.; Goldsmith, J.; Goldar-Najafi, A.; Murphy, C.; Osburne, M.; Mullin, S.; Buxton, D.; Wagner, D.; Kelly, C. *Dig. Dis. Sci.* **2007**, *52* (2), 396−401.

(7) (a) Leodolter, A.; Dominguez-Munoz, J. E.; von Arnim, U.; Kahl, S.; Peitz, U.; Malfertheiner, P. *Am. J. Gastroenterol.* **1999**, *94* (8), 2100−2104. (b) Savarino, V.; Mela, G. S.; Zentilin, P.; Bisso, G.; Pivari, M.; Mansi, C.; Mele, M. R.; Bilardi, C.; Vigneri, S.; Celle, G. *Am. J. Gastroenterol.* **1999**, *94* (5), 1203−1208.

(8) (a) Davidson, E. A.; Trumbore, S. E.; Amundson, R. *Nature* **2000**, *408* (6814), 789−790. (b) Schmidt, M. W.; Torn, M. S.; Abiven, S.; Dittmar, T.; Guggenberger, G.; Janssens, I. A.; Kleber, M.; Kogel-Knabner, I.; Lehmann, J.; Manning, D. A.; Nannipieri, P.; Rasse, D. P.; Weiner, S.; Trumbore, S. E. *Nature* **2011**, *478* (7367), 49−56. (c) Conrad, R. *Microbiol. Rev.* **1996**, *60* (4), 609−640.

(9) Luo, G. J.; Brüggemann, N.; Wolf, B.; Gasche, R.; Grote, R.; Butterbach-Bahl, K. *Biogeosciences* **2012**, *9* (5), 1741−1763.

(10) Jerman, V.; Metje, M.; Mandić-Mulec, I.; Frenzel, P. *Biogeosciences* **2009**, *6* (6), 1127−1138.

(11) Forster, P. R. V; Artaxo, P.; Berntsen, T.; Betts, R.; Fahey, D. W.; Haywood, J.; Lean, J.; Lowe, D. C.; Myhre, G.; Nganga, J.; Prinn, R.; Raga, G.; Schultz, M.; Van Dorland, R. Changes in atmospheric constituents and in radiative forcing. In *Climate Change 2007: The Physical Science Basis. Contribution of Working Group I to the Fourth Assessment Report of the Intergovernmental Panel on Climate Change*; Cambridge University Press: Cambridge, 2007.

(12) Ruser, R.; Flessa, H.; Russow, R.; Schmidt, G.; Buegger, F.; Munch, J. C. *Soil Biol. Biochem.* **2006**, *38* (2), 263−274.

(13) (a) Chikaraishi, Y.; Ogawa, N. O.; Doi, H.; Ohkouchi, N. *Ecol. Res.* **2011**, *26* (4), 835−844. (b) Thomas, K. L.; Benstead, J.; Davies, K. L.; Lloyd, D. *Soil Biol. Biochem.* **1996**, *28* (1), 17. (c) Wuebbles, D.; Hayhoe, K. *Earth-Sci. Rev.* **2002**, *57* (3−4), 177. (d) Andreae, M. O.; Schimel, D. S.; Robertson, G. P. *Exchange of Trace Gases between Terrestrial Ecosystems and the Atmosphere: Report of the Dahlem Workshop on Exchange of Trace Gases between Terrestrial Ecosystems and the Atmosphere*; Wiley: Hoboken, NJ, 1989; p 347.

(14) Deng, C.; Zhang, J.; Yu, X.; Zhang, W.; Zhang, X. *J. Chromatogr., B* **2004**, *810* (2), 269−275.

(15) Badjagbo, K. *Clin. Chem. Lab. Med.* **2012**, *50* (11), 1893−1902.

(16) Berden, G.; Peeters, R.; Meijer, G. *Int. Rev. Phys. Chem.* **2000**, *19* (4), 565−607.

(17) Koskinen, V.; Fonsen, J.; Kauppinen, J.; Kauppinen, I. *Vib. Spectrosc.* **2006**, *42* (2), 239−242.

(18) Wolfbeis, O. S.; Weidgans, B. M. Fiber Optic Chemical Sensors and Biosensors: A View Back. In *Optical Chemical Sensors*; Baldini, F., Chester, A. N., Homola, J., Martellucci, S., Eds. Springer: Dodrecht, 2006; pp 17−44.

(19) (a) Frosch, T.; Schmitt, M.; Noll, T.; Bringmann, G.; Schenzel, K.; Popp, J. *Anal. Chem.* **2007**, *79* (3), 986−993. (b) Frosch, T.; Tarcea, N.; Schmitt, M.; Thiele, H.; Langenhorst, F.; Popp, J. *Anal. Chem.* **2007**, *79* (3), 1101−1108. (c) Frosch, T.; Meyer, T.; Schmitt, M.; Popp, J. *Anal. Chem.* **2007**, *79* (16), 6159−6166. (d) Frosch, T.; Popp, J. *J. Mol. Struct.* **2009**, *924−926*, 301−308. (e) Frosch, T.; Popp, J. *J. Biomed. Opt.* **2010**, *15* (4), 041516/1−041516/9. (f) Frosch, T.; Koncarevic, S.; Zedler, L.; Schmitt, M.; Schenzel, K.; Becker, K.; Popp, J. *J. Phys. Chem. B* **2007**, *111* (37), 11047−11056.

(20) (a) Frosch, T.; Koncarevic, S.; Becker, K.; Popp, J. *Analyst (Cambridge, U.K.)* **2009**, *134* (6), 1126−1132. (b) Frosch, T.; Popp, J. *J. Mol. Struct.* **2009**, *924−926*, 301−308. (c) Frosch, T.; Schmitt, M.; Bringmann, G.; Kiefer, W.; Popp, J. *J. Phys. Chem. B* **2007**, *111* (7), 1815−1822. (d) Frosch, T.; Schmitt, M.; Popp, J. *J. Phys. Chem. B* **2007**, *111* (16), 4171−4177. (e) Frosch, T.; Schmitt, M.; Popp, J. *Anal. Bioanal. Chem.* **2007**, *387* (5), 1749−1757. (f) Frosch, T.; Schmitt, M.; Schenzel, K.; Faber, J. H.; Bringmann, G.; Kiefer, W.; Popp, J. *Biopolymers* **2006**, *82* (4), 295−300.

(21) Okita, Y.; Katagiri, T.; Matsuura, Y. *Proc. SPIE* **2010**, *7559*, 755908−755908.

(22) (a) Frosch, T.; Keiner, R.; Michalzik, B.; Fischer, B.; Popp, J. *Anal. Chem.* **2013**, *85* (3), 1295−1299. (b) Keiner, R.; Frosch, T.; Hanf, S.; Rusznyak, A.; Akob, D. M.; Kusel, K.; Popp, J. *Anal. Chem.* **2013**, *85*, 8708−8714. (c) Keiner, R.; Frosch, T.; Massad, T.; Trumbore, S.; Popp, J. *Analyst* **2014**, DOI: 10.1039/C3AN01971C. (d) Salter, R.; Chu, J.; Hippler, M. *Analyst* **2012**, *137* (20), 4669−4676.

(23) (a) Schlosser, M.; Seitz, H.; Rupp, S.; Herwig, P.; Alecu, C. G.; Sturm, M.; Bornschein, B. *Anal. Chem.* **2013**, *85* (5), 2739−2745. (b) Uda, T.; Okuno, K.; Naruse, Y. *J. Radioanal. Nucl. Chem.* **1992**, *159* (1), 145−154. (c) Uda, T.; Okuno, K.; Naruse, Y. *J. Nucl. Sci. Technol.* **1992**, *29* (3), 288−295.

(24) Frosch, T.; Yan, D.; Popp, J. *Anal. Chem.* **2013**, *85* (13), 6264−6271.

(25) (a) Buric, M. P.; Chen, K.; Falk, J.; Velez, R.; Woodruff, S. In *Raman Sensing of Fuel Gases Using a Reflective Coating Capillary Optical Fiber*; Udd, E., Du, H. H., Wang, A., Eds.; SPIE: Orlando, FL, 2009; pp 731608−731608. (b) Eftekhari, F. *J. Appl. Phys.* **2011**, *109* (11), 113104. (c) Pearman, W. F.; Carter, J. C.; Angel, S. M.; Chan, J. W. *Appl. Opt.* **2008**, *47* (25), 4627−4632.

(26) (a) Russell, P. *Science* **2003**, *299* (5605), 358−362. (b) Knight, J. C.; Broeng, J.; Birks, T. A.; Russell, P. S. J. *Science* **1998**, *282* (5393), 1476−1478.

(27) (a) Buric, M. P.; Chen, K. P.; Falk, J.; Woodruff, S. D. *Appl. Opt.* **2008**, *47* (23), 4255−4261. (b) Buric, M. P.; Chen, K. P.; Falk, J.; Woodruff, S. D. *Appl. Opt.* **2009**, *48* (22), 4424−4429.

(28) Schrötter, H. W.; Klöckner, H. W. Raman Scattering Cross Sections in Gases and Liquids. In *Raman Spectroscopy of Gases and Liquids*, Weber, A., Ed. Springer: Berlin, 1979; Vol. *11*, pp 123−166.
(29) (a) Larkin, P. *Infrared and Raman Spectroscopy: Principles and Spectral Interpretation*, 1st ed.; Elsevier: Amsterdam, 2011. (b) Demtröder, W. *Laser Spectroscopy: Experimental Techniques*, 4th ed.; Springer: Berlin, 2008; Vol. 2.
(30) Long, D. A. *The Raman Effect: A Unified Treatment of the Theory of Raman Scattering by Molecules*; John Wiley & Sons: Hoboken, NJ, 2002; p 624.
(31) Fenner, W. R.; Hyatt, H. a.; Kellam, J. M.; Porto, S. P. S. *J. Opt. Soc. Am.* **1973**, *63* (1), 73−73.
(32) Howard-Lock, H. E.; Stoicheff, B. P. *J. Mol. Spectrosc.* **1971**, *37* (2), 321−326.
(33) Rosman, K. J. R.; Taylor, P. D. P. *Pure Appl. Chem.* **1998**, *70* (1), 18.
(34) Haken, H.; Wolf, H. C. *Molecular Physics and Elements of Quantum Chemistry: Introduction to Experiments and Theory*, 2nd ed.; Springer: Heidelberg, 2004.

7.5. Analysis of fiber-enhanced Raman gas sensing based on Raman chemical imaging

Reproduced from Yan, D.; Popp, J.; Frosch, T., Analysis of Fiber-Enhanced Raman Gas Sensing Based on Raman Chemical Imaging. Anal. Chem. 2017, 89 (22), 12269-12275 with permission from American Chemical Society.

analytical chemistry

Article

Cite This: Anal. Chem. 2017, 89, 12269-12275

pubs.acs.org/ac

Analysis of Fiber-Enhanced Raman Gas Sensing Based on Raman Chemical Imaging

Di Yan,[†] Jürgen Popp,[†,‡,§] and Torsten Frosch*[,†,‡,§]

[†]Leibniz Institute of Photonic Technology, 07745 Jena, Germany

[‡]Friedrich Schiller University, Institute of Physical Chemistry, 07743 Jena, Germany

[§]Friedrich Schiller University, Abbe Center of Photonics, 07745 Jena, Germany

Supporting Information

ABSTRACT: Fiber enhanced Raman spectroscopy (FERS) is an arising new technique for versatile highly sensitive and selective multigas analysis in various applications, such as environmental monitoring and medical breath diagnosis. In this study, the performance of FERS was thoroughly studied with the help of a specially designed multichannel Raman chemical imaging. Several types of hollow core photonic crystal fibers were thoroughly analyzed in terms of their performance in light confinement and sensitive gas sensing. The optimal fiber length for Raman gas sensing was found to be 15 cm in our spectroscopic system. To separate the Raman scattering of the target gas molecules from the background generated by the silica microstructure of the fiber, the optimal diameter of a spatial filter was analyzed and quantified as Ø3.9 μm, which balances the suppression of the silica background and the attenuation of the gas signal, originating from different regions in the plane of the fiber end-face. To achieve an easy-to-use gas monitoring system with stable performance, an automated coupling-method was developed, to simplify the alignment of the FERS setup. The optimized design of the FERS setup has remarkable potential for highly sensitive, miniaturized, easy-to-use, and versatile gas sensing.

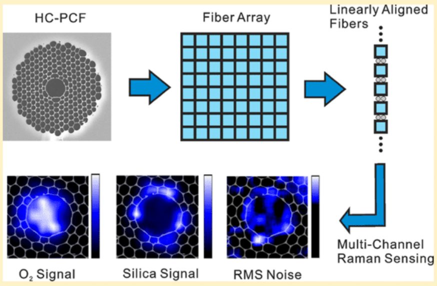

Raman spectroscopy is an emerging technique with excellent chemical selectivity.[1−5] Recently it was developed as nonconsumptive gas sensing technique, which requires no labeling, transducer, or sample preparation.[6−11] All gases except noble gases can simultaneously be identified and quantified by their corresponding Raman bands.[3,12−15] In comparison to gas sensing methods based on infrared absorption spectroscopy,[16] Raman gas sensing also enables the detection of homonuclear diatomic gases, such as oxygen,[17−19] nitrogen,[20] and hydrogen,[21] and is therefore an extremely versatile tool in environmental[22,23] and clinical research.[24] Raman gas sensing commonly suffers from low sensitivity because of the low particle densities of the gases and the weak Raman scattering process.[1] However, the development of novel photonic microstructured fibers enables light guiding in the analyte within the central hollow core with low attenuation.[25−28] Hollow core photonic crystal fibers (HC-PCF) can guide the light within a spectral band gap,[29−31] enable extremely strong light-gas interaction over an extended path length and can improved the sensitivity of Raman gas analysis down to ppm levels.[21,22] However, the sensitivity of fiber-enhanced Raman spectroscopy (FERS) is limited by the fluorescence background and the Raman bands originating from the fused silica of the fiber material.[21] These strong silica signals can saturate the CCD detector. This is a great drawback of the application of silica fibers, especially for sensing of the characteristic Raman bands of oxygen (1555 cm^{-1}) and other interesting gas analytes in the fingerprint wavenumber region (<1800 cm^{-1}). In order to suppress the background and to achieve a highly sensitive gas detection, a separation of the silica signal originating from the cladding region and the gas Raman signal from the central fiber hollow core must be achieved, based on their different spatial distribution, by inserting a pinhole in the confocal plane.

The light confinement of the sensor fiber and the spatial distribution of the gas Raman signals and silica signals at the fiber end-face are important parameters and should be evaluated by means of chemical imaging,[32−35] to evaluate the sensor enhancement and to reveal the potential of further improvements. A common method to obtain the spatial distribution of Raman signals is the application of a motorized sample stage, and the point-by-point scanning of the laser focus scans over an area of the sample by moving the stage after each exposure. A confocal hole is often included in the system, to reduce the scattering volume in each Raman spectroscopic acquisition and to achieve a better spatial resolution. The total time elapse of the scanning procedure consists of the exposure time of all points plus a gap-time for sample movement and

Received: August 9, 2017
Accepted: October 19, 2017
Published: October 31, 2017

DOI: 10.1021/acs.analchem.7b03209
Anal. Chem. 2017, 89, 12269−12275

data processing. There can be a long time gap between the first measurement point and the last one, bringing the challenge that the sample might be altered over time or affected by the movement of the stage.

A recent approach for Raman imaging is multichannel Raman imaging based on fiber arrays.[32−34] Fiber array spectroscopy was first reported in astrophysics as an imaging technique[32] and provides the opportunity to obtain spatially resolved spectra simultaneously without any moving parts. A wide-field illumination of the sample over a certain field-of-view is achieved instead of a focus spot, and the back scattered Raman signal is focused onto an optical fiber array (Figure 1, inset 1). The optical fibers at the distal end are linearly aligned at the slit of the spectrometer (Figure 1, inset 2). The spectral information on all fibers is dispersed along the vertical axis of the CCD detector in a single frame acquisition (Figure 1, inset 3). By separating the Raman spectral information on the CCD along the vertical axis into multiple ROIs (region-of-interest), the spatial distribution of the measured Raman spectra can be reconstructed in the sample plane.

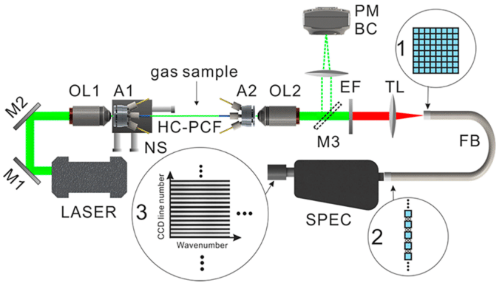

Figure 1. Schematic sketch of the setup, combining forward FERS with multichannel Raman imaging. The laser beam was coupled into the hollow-core photonic crystal fiber, and the forward scattered Raman signal was projected on the input face of the fiber bundle to obtain chemical information with spatial resolution: OL1, 20× objective lens; OL2, 100× objective lens; A1 and A2, custom-made adapters; PM, laser power-meter; BC, beam camera; EF, edge filter; TL, tube lens (180 mm); FB, fiber bundle; SPEC, spectrometer; NS, 3-axis nanostage. Inset 1: Schematic sketch of the fiber bundle. Inset 2: Fibers linearly aligned with spacer in between. Inset 3: Spectral information on the fibers is dispersed along the vertical axis of the CCD.

■ MATERIALS AND METHODS

An experiment setup was developed (Figure 1), which combines forward scattering FERS with multichannel Raman imaging. The setup was equipped with a Nd:YAG laser ($\lambda_{\text{exc.}}$ = 532 nm). The laser beam was coupled into the HC-PCF with a 20× objective lens (OL1), and coupled out of the fiber with a 100× objective lens (OL2) through the optical window of a custom-designed fiber adapter assembly (A1 and A2). The out-coupled beam at the fiber end was inspected subsequently with a power-meter (PM) and a beam camera (BC). The laser wavelength was suppressed by a long-pass edge filter (EF) for Raman sensing, and the scattered Raman signal was focused by a tube lens (TL) with 180 mm focal length. The Raman signal in the conjugate focal plane (rear focal plane of the tube lens) was collected with a fiber bundle (FB) of 64 quadratic fibers. The end faces of these fibers were arranged in an 8 by 8 array. The side lengths of the array were 1 mm by 1 mm. Thus, a field-of-view of 10 μm by 10 μm on the sample was achieved with the 100× objective lens. The pixel pitch of the Raman image was 1.25 μm, as the pitch between the fibers was 125 μm. The fibers of the bundle were arranged linearly with spacers of 60 μm in between the fibers at the entrance slit of the spectrometer. The linear line of fibers was carefully positioned at the entrance slit of the spectrometer. An Acton and an IsoPlane spectrometer (Princeton Instruments) were employed.

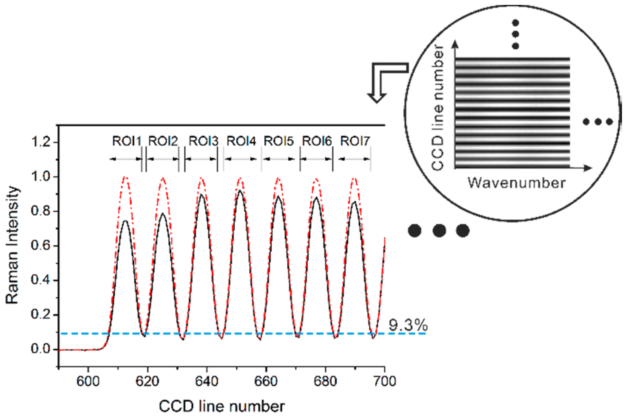

Figure 2. Region-of-interest of each Raman spectrum was recognized automatically with a peak-finding algorithm, and used the peak positions as the centers of the ROIs. The plot of the total counts of each horizontal CCD line showed a multipeak pattern (black solid-line, only the first 7 peaks are displayed in this figure). The Raman signal in all ROIs was normalized to the same intensity to obtain data points with correct intensity distribution (red dash-line). The CCD counts at the valley positions had values of 9.3% of the values at the peaks in average (blue dash-line), indicating very little cross-talk from one fiber to another. Inset: Raman spectra of all fibers were recorded on the CCD in single frames with vertical offsets.

■ RESULTS AND DISCUSSION

System Calibration and Evaluation. The Raman spectra of all the fibers were simultaneously recorded with defined vertical offsets, provided by the spacers, with the CCD of the spectrometer. To obtain a precise spatial distribution of the Raman signals, a calibration of the system was needed. The calibration was performed with a measurement of a homogeneous light source. The first step of the data processing was recognizing the regions-of-interest (ROIs) on the CCD for each spectrum. The plot of the total counts of each horizontal CCD lines showed a multipeak pattern (Figure 2). The peaks are the horizontal CCD lines with strong Raman signal from the fibers and the valleys are the spacers in between. As the spacers do not transfer any Raman signal, the CCD counts at the valley positions represent the cross-talk between adjacent fibers. In the data processing, each peak was located with a peak-finding function, and the peak positions were used as the centers of the ROIs. The width of all ROIs was set to 11 lines, to obtain sufficient Raman signal with minimized cross-talk (Figure 2). The second step of the data processing was intensity normalization. As the guiding efficiencies of the fibers are not perfectly homogeneous, the signal from a homogeneous light source did not have the same intensities in all ROIs. In order to obtain corrected data points, the Raman signals in all ROIs were normalized to the same intensity (Figure 2, red dashed line), and the different guiding efficiencies of the fibers were corrected. With the calibrated system, 64 Raman spectra could be recorded in each exposure. The Raman peaks of interest could then be selected, and the acquired data (peak height, noise, and SNR) were utilized to recreate the Raman images with chemical information.

The image of the homogeneous light source was now recreated with excellent flatness of ±1.3% peak-to-peak with the corrected system (Figure SM1). The CCD counts at the valleys were 9.3% of the peak in average (Figure 2), therefore the average peak contrast achieved was 90.7%, indicating very little cross-talk between adjacent fibers. The distribution of the intensity was assumed as a multi-Gaussian pattern, and each Gaussian peak only partly overlapped with the two peaks next to it. In this condition, the problem can be simplified to 2 peaks (Figure 3). The peak function is a Gaussian function with normalized peak height. The valley locates at $x = 0$, and the center of two peaks locates at $x = \pm b$ (eq 1).

$$\begin{cases} f_1(x) = e^{-(x-b)^2/2c^2} \\ f_2(x) = e^{-(x+b)^2/2c^2} \end{cases} \tag{1}$$

The values at the valleys are 9.26% of the peaks in average

$$f_1(0) + f_2(0) = 2 \times e^{-b^2/2c^2} = 0.0926 \tag{2}$$

$$\frac{b}{c} = \sqrt{-2 \times \ln \frac{0.0926}{2}} = 2.48 \tag{3}$$

According to the calibration data, the average distance between two peaks is 11.8 CCD lines, therefore $b = 5.9$ and $c = 2.38$. As the width of ROIs is set to $w = 11$ CCD lines, the ROI for the left peak (red dash line in Figure 3) is $\left(-b - \frac{w}{2}, -b + \frac{w}{2}\right) = (-11.4, -0.4)$. For the right peak with $b = 5.9$, $c = 2.38$, and the Gauss error function $\mathrm{erf}(x)$, describing the probability for a random variable falling in the range $[-x, x]$, the part of signal that leaks into the ROI of the left peak is

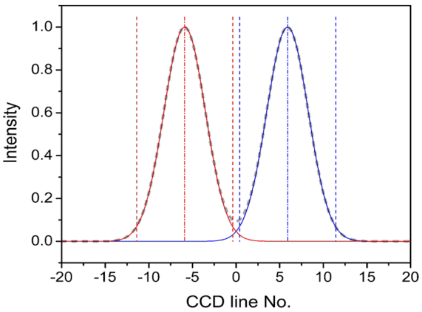

Figure 3. Multipeak pattern of the signal intensity on the CCD lines was simplified as a two-peak model to evaluate the cross-talk between channels. The position of the valley was defined as 0 (gray dash line), and the two normalized peaks located symmetrically to the valley (red and blue solid line). The distance between the two peaks was 11.8 lines and the count at the valley was 0.0926, according to the calibration data. The width of the ROI (region-of-interest) was 11 CCD lines for all measurements. In the left ROI (red dash line), only a very small part of the intensity originated from the tail of the blue peak. As a result, the cross-talk was quantified as 0.4%.

$$F(x) = \frac{1}{2}\left[1 + \mathrm{erf}\left(\frac{x-b}{\sqrt{2}\,c}\right)\right] \tag{4}$$

$$F(-0.4) = 0.00406 \tag{5}$$

As a result, the cross-talk of the signal from one fiber to another neighbor fiber is only 0.406% of the transmitted light intensity.

Raman Imaging of Hollow Core Photonic Crystal Fibers. Two types of HC-PCFs (HC-532 and HC-580) at length of 60 cm were analyzed and coupled with the excitation laser (100 mW, $\lambda_{\mathrm{exc.}}$ = 532 nm). The laser intensity map captured with the beam camera shows that the laser power was mainly confined in the hollow cores of the photonic crystal fibers (Figure 4). However, a small part of the laser power leaked into the microstructure, mainly in the first ring of the surrounding cladding holes (Figure 4). This part of the guided laser power excites signals from the fused silica material. Signals

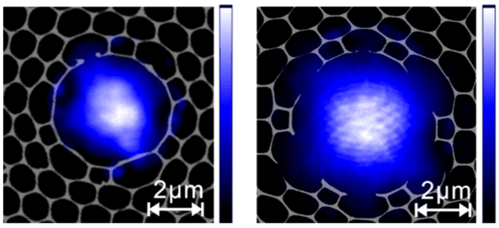

Figure 4. Intensity map at the fiber end, captured with the beam camera (left, HC-532; right, HC-580). The laser power was mainly confined in the hollow cores of the photonic crystal fibers. A small part of the laser power leaked into the microstructure of the fiber cladding, mainly in the first ring of the surrounding air holes and excited Raman signals from the fused silica material.

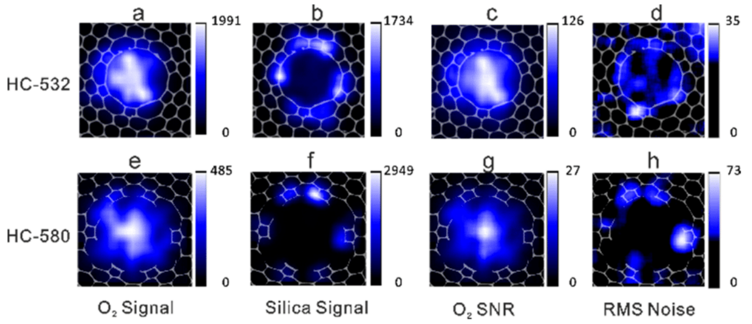

Figure 5. Raman images of the photonic crystal fibers HC-532 (a−d) and HC-580 (e−h) with 60 cm fiber length. The Raman scattering of oxygen (Raman peak at 1555 cm^{-1}) originated mainly from the central hollow core of the HC-PCF (a, e). The signal of the fused silica (Raman peak at 1061 cm^{-1}) appeared strong at the first ring of the surrounding microstructure (5, f). The results from HC-532 showed a higher oxygen Raman signal (a) and higher SNR (c). The baseline noise (d, h) showed a similar distribution as the silica signal (b, f), which was the main source of the baseline noise.

from the fused silica material result in additional fluorescence background, Raman bands, and random noise and therefore affect the performance of Raman gas sensing. The laser was better confined in the HC-532 fiber in comparison to the HC-580 fiber (higher laser power at the fiber output), and thus a lower amount of laser power leaked into the microstructure of the HC-532 photonic crystal fiber.

The Raman spectra were acquired from the HC-PCF with the described multichannel Raman imaging setup (Figure 1). With this method the Raman image can be captured with one measurement over the entire hollow core of the fiber. In conventional Raman scanning microspectroscopy, the Raman distribution at the end of the HC-PCF would be affected by the movement of the scanning stage. In multichannel Raman spectroscopy, the HC-PCF keeps static during the measurement and the drawbacks of scanning methods can be overcome. The Raman images collected from the fiber ends show that the Raman scattering of oxygen (Raman band at 1555 cm^{-1}) mainly originated from the central hollow core of the HC-PCF (Figure 5a and 5e). As a small part of the laser power leaked into the silica material, the surrounding microstructure was also excited. The Raman images acquired provided a very good resolution of the spatial distribution of the Raman signals and showed that the signal of fused silica (Raman band at 1061 cm^{-1}) was strong at the first ring of the surrounding cladding microstructure (Figure 5b and 5f). The maximum values of the Raman signals of the fused silica were 1734 and 2949 counts in the HC-532 and HC-580 fibers, respectively. The HC-532 fiber showed weaker Raman bands from the fused silica, compared to the HC-580 fiber. The Raman peak of oxygen had a higher SNR in HC-532 (126 in maximum) compared to HC-580 (27 in maximum) (Figure 5c and 5g). The plot of the baseline noise (Figure 5d and 5h) showed a similar spatial distribution as the silica signals (Figures 5b and 5f), indicating that the fused silica causes the baseline noise. Thus, the laser excitation of the silica microstructure is the source of the noise and limits the spectroscopic system from achieving a high signal-to-noise ratio (SNR) of the Raman band of the analyte gases.

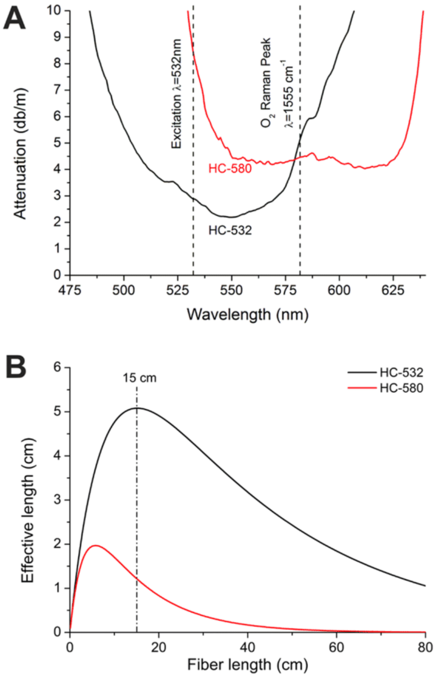

Figure 6. (a) Transmission spectra of the two types of PCFs: HC-532 and HC-580. (b) Effective lengths of the fibers.[36]

Optimization of the Fiber Length. To optimize the analytical performance of the fiber enhanced Raman gas sensing setup, the influence of the optimal fiber length was studied. The transmission spectra of two HC-PCFs were measured with the standard cutback method (Figure 6A). The attenuation of the laser excitation (532 nm) was 2.8 and 8.5 db/m for the HC-532 and HC-580 fibers, respectively. The attenuations at the wavelength of the Raman peak of oxygen (580 nm or 1555 cm^{-1} shift from 532 nm) were 5 db/m and 4.5 db/m, for HC-532 and HC-580, respectively. The HC-532 fiber provided a better optical guidance for the excitation laser and the Raman scattered photons in the fingerprint region. In forward fiber enhanced Raman scattering, the optimal fiber length depends on the loss coefficient at the wavelengths of the laser and the Raman signal. The effective length of the fiber can be derived from the fiber physical length and the attenuation,[36,37] based on eq 6, where α_l is the fiber attenuation at the laser wavelength (532 nm), and α_r is the attenuation at the oxygen Raman peak (580 nm).

$$L_{\mathrm{eff}} = \frac{(e^{-\alpha_l L_p} - e^{-\alpha_r L_p})}{\alpha_r - \alpha_l} \qquad (6)$$

The effective length elucidates the ability of the sensor fiber for the enhancement of the Raman signal. According to the calculation (Figure 6B), the performance of FERS can be further improved by employing a piece of HC-532 with the optimal fiber length of 15 cm. The cleaved fiber piece of 15 cm was measured with a shorter exposure time (1 s instead of 5 s) and a maximum value of 101 was achieved as SNR in the fiber core region, compared to a SNR of 126 that was achieved with the 60 cm fiber piece with 5s acquisition time (Figure 5c). Therefore, the sensitivity improved approximately 4 times with the optimized fiber length of the HC-PCF.

Optimization of the Spatial Filter. Spatial filtering can be of high advantage for background reduction and SNR improvement, as the Raman signal of the gaseous analyte mostly originates from the fiber core and the silica Raman signal mainly distributes on the surrounding microstructure. Pinholes of various diameter were inserted in the intermediate image plane to eliminate the silica signal, and the suitable pinhole sizes were determined according to the SNR of the gas Raman signal.[21] The effect of spatial filtering can be revealed by summing the Raman signal within the filter diameter in the Raman image of the 15 cm HC-532 fiber (Figure 7A). With the decrease of the filter diameter, both - normalized silica signal and normalized O_2 signal were decreasing (Figure 7B). The difference of the normalized silica signal and the gas signal reached a maximum with a 3.9 μm pinhole diameter (Figure 7B). This optimal diameter of the spatial filter balanced the suppression of the silica signal and the decrease of the Raman gas signal in the setup.

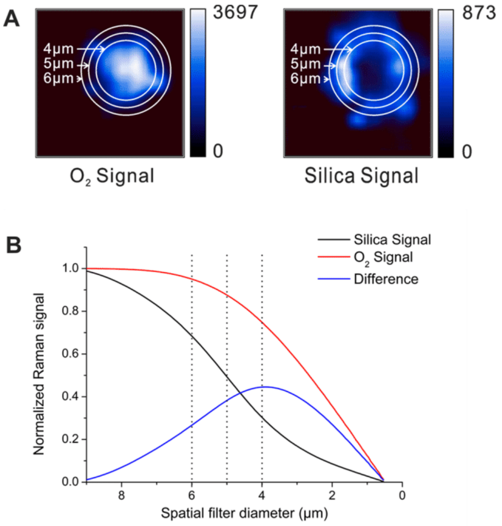

Figure 7. (A) Raman images of the photonic crystal fiber HC-532 (15 cm length). Circles: Spatial filters with various diameters. (B) With the decrease of the filter diameter, both normalized silica signal (black) and normalized O_2 Raman signal (red) were decreasing. The difference between the normalized silica signal and the O_2 Raman signal (blue) reached the maximum at 3.9 μm. This optimal diameter of the spatial filter balanced the suppression of the silica signal and the decrease of the Raman gas signal.

Development of an Automatic Fiber Alignment System. In practice, the alignment of the laser coupling can be tedious and time-consuming, because of the small mode field. The mode field diameter of the HC-532 photonic crystal fiber is only 4 μm and the out-coupled laser power strongly decreases with an offset to the optimized coupling position (Figure 8A). Even small offsets of the laser coupling can cause a strong reduction of the laser transmission. A low laser transmission of the fiber indicates a leakage of the laser power from the core to the cladding region and, therefore, leads to high silica signals and strong baseline noise. The Raman signal in the plane of the fiber end-face can strongly change from analyte signal to background signal (Figure 8B), with an offset of only 1 μm away from the optimal position (center of the core mode field). The oxygen Raman signal from the fiber core decreased tremendously to 189 counts (compared to 1991 counts, Figure 5a), and the Raman signal of fused silica from the surrounding microstructure raised by 1 order of magnitude, especially on the fiber side closer to the (wrong) laser coupling position (Figure 8B compared to Figure 5b). Therefore, a very precise alignment of the laser coupling is of key importance in fiber enhanced Raman gas sensing.

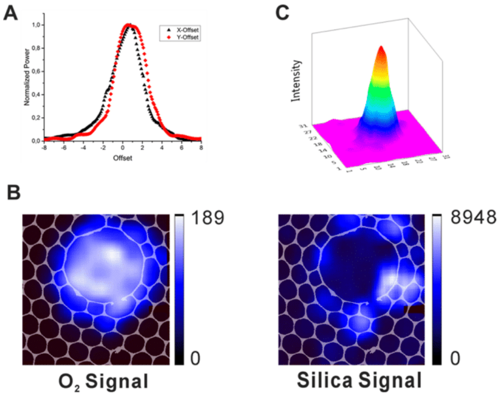

Figure 8. (A) Out-coupled laser power at various coupling positions. Even small offsets of the laser coupling position caused a strong reduction of the laser transmission. (B) Raman images of the photonic crystal fiber HC-532 with 15 cm length, when the coupling position had an offset of 1 μm from the optimized position. The oxygen Raman signal from the fiber core was weak and the Raman signal of fused silica from the surrounding microstructure became very strong on the right lower side (direction of the laser offset). (C) Plot of the out-coupled laser power with various coupling positions in the x−y plane (radial direction) acquired within 3.6 min. A clear peak of the out-coupled laser power indicated the correct coupling position with low fiber attenuation.

To achieve an easy-to-use gas monitoring system with stable performance, a fast, automatic alignment system was developed, based on a 3-axis automated stage (NS in Figure 1), which was equipped with step-motors and close-loop piezo actuators on all three axes. The fiber adapter was installed on the stage, and the coupling system tuned the position of the fiber adapter in three dimensions in order to achieve optimized laser coupling. The out-coupled laser power was measured to evaluate the quality of the coupling. The mode field of the HC-PCF was very small and the complex microstructures guided modes with suboptimal alignment (local maxima). Therefore, the conventional climbing-hill algorithm could not be applied to find the correct coupling position. In order to find the position of the fiber hollow core rapidly, the system first moved the fiber end-face in the $x-y$ plane (radial direction) through an array of positions along a square spiral route starting from the center of the array, and recorded simultaneously the out-coupled laser power and the $x-y$ coordinate. Then the fiber was moved back to the position with the maximum laser power. Subsequently, the laser coupling was tested at various positions with z-offset (focus position), and then the stage moved to the position of the maximum power. This position was set as the center point of the next square spiral route in $x-y$ plane, and the procedure was repeated in a narrower range with a smaller step size. After several loops of searching, the system could achieve an optimized laser coupling (flowchart in Figure SM2a). The speed of the system was approximately 250 points per minute. Depending on the radius of the range and the step size, each loop of scanning lasted several minutes. A typical result of the $x-y$ plane search is shown in Figure 8C, which was achieved within 3.6 min. The automated coupling system ensures the optimized tuning of the setup, and greatly eases the work of replacing and aligning the photonic crystal fiber. As the laser coupling of the optical fiber was influenced by temperature change and float over time, it was necessary to retune the coupling in a small range (typically within 2 μm) after the system warm-up, or after the system had been kept on for more than 1 day. To achieve optimized laser coupling again promptly, a fine-tuning mode that used the closed-loop piezo actuators was designed. There was no need to scan the whole fiber end face again, as the coupling status was usually still very close to the optimized coupling position. Furthermore, the laser coupling position was not very sensitive on the z-axis, and therefore no adjustment on z-axis was needed in this situation. The system moved first the fiber end to several offset positions on the x axis and moves to the observed best coupling position. Then the system searched positions on the y axis for the optimal coupling. The procedure was repeated several times on the x and y axes iteratively, until the expected out-coupling laser power was achieved (flowchart in Figure SM2b).

CONCLUSION

In this study, the performance of FERS gas sensing was studied. A special multichannel Raman imaging system was designed and coupled to the FERS setup. The Raman imaging system can be exploited to display the chemical structure of the distributions of the signals with good spatial resolution in a $10 \times 10\ \mu\text{m}^2$ field-of-view on the fiber end-face. With a proper calibration procedure, the system provides excellent Raman images with an error of the signal intensity of ±1.3%, and a cross-talk from one channel to the neighbor channel of only 0.4%. According to the results achieved with the Raman imaging system and a laser beam camera, the major parts of the laser power and the scattered Raman signal of the gas analyte were confined in the hollow core of the HC-PCF. As a part of the excitation laser leaked out of the central hollow core of the HC-PCF, strong signals of fused silica originated mainly from the first ring of the cladding microstructure of the hollow fiber. The Raman signal from fused silica resulted in additional Raman bands, fluorescence background, and baseline noise, which was acquired in sum spectra and therefore limited the system from achieving high signal-to-noise ratios (SNR). By comparing several types of HC-PCFs, it was found that the fiber HC-532 showed the best signal-to-noise ratio of oxygen (1555 cm^{-1} peak) in its core region. According to the transmission spectra of two types of fibers, HC-532 provided excellent optical guiding at the wavelength of the excitation laser (2.8 dB/m) and the Raman signal (5 dB/m). The optimal fiber length of the sensor fiber was found to be 15 cm. To suppress the unwanted silica signal from the gas sensing measurements, the effect of spatial filtering was thoroughly analyzed at the fiber end-face with the help of the Raman imaging system. As a result, the optimal diameter of the spatial filter was found at 3.9 μm, which can balance the filtering of the silica signal at optimal SNR of the analyte gas signal. The precision of the laser coupling position was studied, and the result showed that only 1 μm offset in the coupling position decreased the sensitivity of the system for more than 1 order of magnitude (Figure 8B). In order to achieve an easy-to-use gas monitoring system, an automated laser coupling system was developed, based on a motorized 3-axis stage and a feedback loop. With this coupling system, it was ensured that the gas sensing setup worked with optimal laser coupling. The automated system also simplified the procedure of aligning the photonic crystal fiber in the FERS setup.

In summary, a FERS gas sensing setup was thoroughly examined with help of Raman chemical imaging. The optimization of the fiber type, fiber length, and the size of the spatial filter for high sensitivity Raman gas analysis were thoroughly discussed. An automated coupling method was developed to simplify the alignment of the FERS setup. The optimal design of the FERS gas-sensing setup provides great potential as versatile, miniaturized, easy-to-use, and highly sensitive gas sensor in various applications.

ASSOCIATED CONTENT

Supporting Information

The Supporting Information is available free of charge on the ACS Publications website at DOI: 10.1021/acs.analchem.7b03209.

Normalized intensity as a function of the fiber and flowchart describing the algorithm for finding the laser coupling (PDF)

AUTHOR INFORMATION

Corresponding Author

*E-mail: torsten.frosch@uni-jena.de, torsten.frosch@gmx.de.

ORCID

Torsten Frosch: 0000-0003-3358-8878

Notes

The authors declare no competing financial interest.

ACKNOWLEDGMENTS

Funding from the federal state of Thuringia (Forschergruppe Biadifa; FKZ: 2016 FGR 0051, 2015-0021) and ESF is highly acknowledged.

REFERENCES

(1) Long, D. A. *The Raman Effect: A Unified Treatment of the Theory of Raman Scattering by Molecules*; Wiley, 2002.
(2) Frosch, T.; Popp, J. *J. Biomed. Opt.* **2010**, *15* (4), 041516.
(3) Smith, T. W.; Hippler, M. *Anal. Chem.* **2017**, *89* (3), 2147−2154.
(4) Frosch, T.; Popp, J. *J. Mol. Struct.* **2009**, *924*−*926*, 301−308.
(5) Yan, D.; Domes, C.; Domes, R.; Frosch, T.; Popp, J.; Pletz, M. W.; Frosch, T. *Analyst* **2016**, *141* (21), 6104−6115.
(6) Salter, R.; Chu, J.; Hippler, M. *Analyst* **2012**, *137* (20), 4669−76.
(7) Kiefer, J.; Seeger, T.; Steuer, S.; Schorsch, S.; Weikl, M. C.; Leipertz, A. *Meas. Sci. Technol.* **2008**, *19* (8), 085408.
(8) Keiner, R.; Frosch, T.; Hanf, S.; Rusznyak, A.; Akob, D. M.; Kusel, K.; Popp, J. *Anal. Chem.* **2013**, *85* (18), 8708−8714.
(9) Friss, A. J.; Limbach, C. M.; Yalin, A. P. *Opt. Lett.* **2016**, *41* (14), 3193−3196.
(10) Keiner, R.; Gruselle, M. C.; Michalzik, B.; Popp, J.; Frosch, T. *Anal. Bioanal. Chem.* **2015**, *407* (7), 1813−7.
(11) Domes, C.; Domes, R.; Popp, J.; Pletz, M. W.; Frosch, T. *Anal. Chem.* **2017**, *89* (18), 9997−10003.
(12) Jochum, T.; von Fischer, J. C.; Trumbore, S.; Popp, J.; Frosch, T. *Anal. Chem.* **2015**, *87* (21), 11137−42.
(13) Schrötter, H. W. *J. Mol. Struct.* **2003**, *661-662*, 465−468.
(14) Keiner, R.; Frosch, T.; Massad, T.; Trumbore, S.; Popp, J. *Analyst* **2014**, *139* (16), 3879−3884.
(15) Keiner, R.; Herrmann, M.; Kusel, K.; Popp, J.; Frosch, T. *Anal. Chim. Acta* **2015**, *864*, 39−47.
(16) Stelmaszczyk, K.; Rohwetter, P.; Fechner, M.; Queisser, M.; Czyzewski, A.; Stacewicz, T.; Woste, L. *Opt. Express* **2009**, *17* (5), 3673−8.
(17) Frosch, T.; Keiner, R.; Michalzik, B.; Fischer, B.; Popp, J. *Anal. Chem.* **2013**, *85* (3), 1295−1299.
(18) Hanf, S.; Fischer, S.; Hartmann, H.; Keiner, R.; Trumbore, S.; Popp, J.; Frosch, T. *Analyst* **2015**, *140* (13), 4473−4481.
(19) Jochum, T.; Michalzik, B.; Bachmann, A.; Popp, J.; Frosch, T. *Analyst* **2015**, *140* (9), 3143−9.
(20) Jochum, T.; Fastnacht, A.; Trumbore, S. E.; Popp, J.; Frosch, T. *Anal. Chem.* **2017**, *89* (2), 1117−1122.
(21) Hanf, S.; Boegoezi, T.; Keiner, R.; Frosch, T.; Popp, J. *Anal. Chem.* **2015**, *87* (2), 982−988.
(22) Hanf, S.; Keiner, R.; Yan, D.; Popp, J.; Frosch, T. *Anal. Chem.* **2014**, *86* (11), 5278−85.
(23) Sieburg, A.; Jochum, T.; Trumbore, S. E.; Popp, J.; Frosch, T. *Analyst* **2017**, *142* (18), 3360−3369.
(24) Boegoezi, T.; Popp, J.; Frosch, T. *Bioanalysis* **2015**, *7* (3), 281−284.
(25) Khetani, A.; Riordon, J.; Tiwari, V.; Momenpour, A.; Godin, M.; Anis, H. *Opt. Express* **2013**, *21* (10), 12340−50.
(26) Hartung, A.; Kobelke, J.; Schwuchow, A.; Bierlich, J.; Popp, J.; Schmidt, M. A.; Frosch, T. *Opt. Lett.* **2015**, *40* (14), 3432−5.
(27) Jochum, T.; Rahal, L.; Suckert, R. J.; Popp, J.; Frosch, T. *Analyst* **2016**, *141* (6), 2023−9.
(28) Hartung, A.; Kobelke, J.; Schwuchow, A.; Wondraczek, K.; Bierlich, J.; Popp, J.; Frosch, T.; Schmidt, M. A. *Opt. Express* **2014**, *22* (16), 19131−19140.
(29) Knight, J. C.; Birks, T. A.; Russell, P. S. J.; de Sandro, J. P. *J. Opt. Soc. Am. A* **1998**, *15* (3), 748−752.
(30) Russell, P. *Science* **2003**, *299* (5605), 358−362.
(31) Yan, D.; Popp, J.; Pletz, M. W.; Frosch, T. *ACS Photonics* **2017**, *4* (1), 138−145.
(32) Okuno, M.; Hamaguchi, H. *Opt. Lett.* **2010**, *35* (24), 4096−4098.
(33) Brueckner, M.; Becker, K.; Popp, J.; Frosch, T. *Anal. Chim. Acta* **2015**, *894*, 76−84.
(34) Samuel, A. Z.; Yabumoto, S.; Kawamura, K.; Iwata, K. *Analyst* **2015**, *140* (6), 1847−1851.
(35) Frosch, T.; Chan, K. L.; Wong, H. C.; Cabral, J. T.; Kazarian, S. G. *Langmuir* **2010**, *26* (24), 19027−32.
(36) Altkorn, R.; Malinsky, M. D.; Van Duyne, R. P.; Koev, I. *Appl. Spectrosc.* **2001**, *55* (4), 373−381.
(37) Frosch, T.; Yan, D.; Popp, J. *Anal. Chem.* **2013**, *85* (13), 6264−71.

7.6. Highly sensitive broadband Raman sensing of antibiotics in step-index hollow-core photonic crystal fibers

Reproduced from Yan, D.; Popp, J.; Pletz, M. W.; Frosch, T., Highly Sensitive Broadband Raman Sensing of Antibiotics in Step-Index Hollow-Core Photonic Crystal Fibers. ACS Photonics 2017, 4 (1), 138-145. with permission from American Chemical Society.

ACS Photonics
Article
pubs.acs.org/journal/apchd5

Highly Sensitive Broadband Raman Sensing of Antibiotics in Step-Index Hollow-Core Photonic Crystal Fibers

Di Yan,[†] Jürgen Popp,[†,‡,§] Mathias W. Pletz,[∥] and Torsten Frosch*[,†,‡,§]

[†]Leibniz Institute of Photonic Technology, 07745 Jena, Germany
[‡]Friedrich Schiller University, Institute for Physical Chemistry, 07743 Jena, Germany
[§]Friedrich Schiller University, Abbe Centre of Photonics, 07745 Jena, Germany
[∥]University Hospital, Center for Infectious Diseases and Infection Control, 07747 Jena, Germany

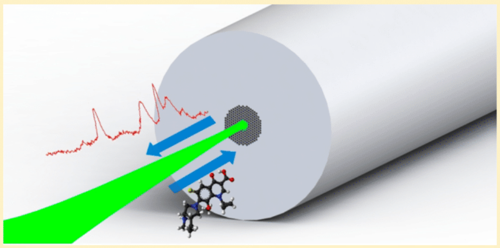

ABSTRACT: Broadband fiber enhanced Raman spectroscopy (FERS) in aqueous media is introduced in elaborated hollow-core photonic crystal fibers. The high requirements on the filigree fiber structure were thoroughly analyzed. A preparation technique was developed for the precise selective filling of such high-performance sensor fibers. Broadband step-index light guidance in aqueous solutions was achieved for the first time in photonic crystal fibers across the whole visible and NIR spectral range. Thus, strong Raman signal enhancements could be demonstrated with various excitation wavelengths and for the high-wavenumber region. The novel fiber enhancement technique was exploited for low-concentration measurements of the frequently used broad-spectrum antibiotic moxifloxacin down to 1.7 μM in only a 4 nL sample volume. These unique abilities for chemical-selective, highly sensitive antibiotic monitoring will pave the way for rapid, minimally invasive analysis of antibiotic concentrations in serum and other body fluids from infected sites. This will allow a precise therapeutic drug monitoring and consecutive rapid dose adjustment in critically ill patients who require individual dosing due to large inter- and intraindividual changes in pharmacokinetic properties.

KEYWORDS: *antibiotic, fiber-enhanced Raman spectroscopy, hollow-core photonic crystal fiber, selective filling, broadband light guidance*

Severe sepsis and septic shock are some of the most common reasons for admission to intensive care units[1,2] in hospitals. Sepsis is defined as an out of proportion inflammatory response to infections leading to organ damage that may progress to organ failure and death.[3] Pneumonia, followed by intra-abdominal infections, skin and skin structure infections, and intravascular catheter related infections are the most frequent sources of sepsis.[4] An optimal antibacterial strategy should achieve therapeutic drug concentrations in the serum[5] of the individual patient and at the site of infection.[6] Clinical studies, e.g., for moxifloxacin, have shown that plasma levels of antibiotics exhibit large inter- and even intraindividual changes in patients with severe sepsis and septic shock.[7] This is explained by altered pharmacokinetic parameters such as increased volume of distribution and changes in the protein-bound fraction as well as hepatic and renal clearance. These alterations can change quickly within hours, are not reliably predictable, and result in underdosing, leading to increased treatment failure, or overdosing, associated with increased drug toxicity.[8] Therefore, it has become increasingly clear within the last years that licensed dose recommendations that are derived from studies in healthy volunteers or patients with mild or moderate infections cannot be transferred to critically ill patients with severe infections. For some anti-infectives, such as vancomycin, aminoglykosides, or voriconazole, dose adjustment based on therapeutic drug monitoring has already been shown to improve clinical outcomes.[9−11] Techniques that are employed to determine the antibiotic level in body fluids are nowadays mainly based on chromatography[12] and electrophoresis,[13] which are time-consuming and require complex procedures of sample preparation. These techniques and the time for sample transport to central laboratories require a time-to-result interval of several hours or even days, making immediate dose adjustments impossible. Therefore, there is an urgent need for easy-to-use, chemically selective and sensitive techniques for the rapid detection of the individual antibiotic level of intensive care patients that is suitable for a point-of-care test.

Raman spectroscopy is a noninvasive analytical technique[14−17] with high potential for chemically selective analysis of biomolecules[18−23] and pharmaceuticals.[24−27] However, Raman scattering is a weak process and has to be enhanced for the analysis of low-concentrated solutions.[28−31] A very promising approach is the development of optical sensor fibers, which guide the light with very low losses and increase the interaction with

Received: September 11, 2016

DOI: 10.1021/acsphotonics.6b00688
ACS Photonics XXXX, XXX, XXX−XXX

the analyte molecules in the fiber hollow core tremendously.[32−34]

In some early studies, fused silica was employed to form the cladding of liquid core fibers.[35−37] As the refractive index (RI) of fused silica is approximately 1.46, the sample in the fiber core is limited to liquids of high RI such as benzene and carbon disulfide. Light cannot be guided in the core of simple silica capillaries that are filled with low-RI liquids such as clinically relevant aqueous solutions. In order to fulfill step-index guiding in water, materials with low refractive indices were employed in various approaches to establish the liquid waveguide,[28,29,38−41] and direct light coupling into a water stream was also performed.[42−44] However, most of these techniques suffer from the insufficient optical quality of the material, strong power losses in the waveguide, and instabilities in the setup.

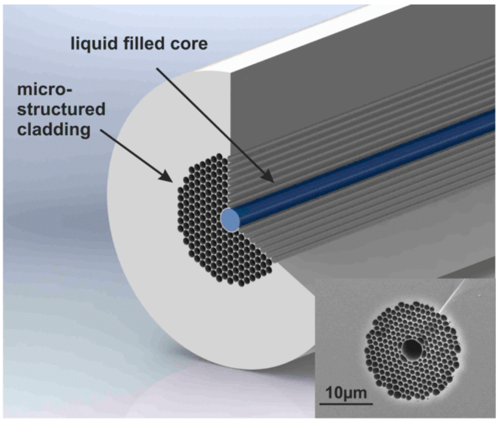

Figure 1. Schematic drawing of the hollow core photonic crystal fiber with selectively filled central core. Inset: Electron microscopic picture of the fiber cross section with scale bar.

Hollow core photonic crystal fibers (HC-PCFs) are a novel type of optical fibers that feature a hollow core surrounded by a periodic array of small air holes (Figure 1). The microstructure in the cladding of the HC-PCF provides an optical band gap and guidance of a defined spectral region within the inner hollow core.[45] In the past decade, efforts have been dedicated in the field of HC-PCF-enhanced Raman sensing.[46−66] The simplest way to utilize an HC-PCF for Raman enhancement of aqueous samples is the nonselective filling of the entire structure with liquid.[46−50,58−60,62,66] In doing so, the band gap of the HC-PCF is shifted to shorter wavelengths when the air cladding holes are filled with liquids, due to the change in the contrast of the refractive indices.[50] By guiding the excitation light and the scattered Raman signal in this shifted band gap region, fiber enhancements of the Raman signal were acquired in prior studies.[46−50,58−60,62,66] However, the decreased dielectric contrast narrows the spectral width of the band gap,[67] which in turn limits the choice of the excitation laser wavelength and the available spectral range for the Raman spectra.

In order to overcome this disadvantage of a narrow band gap in nonselectively filled HC-PCFs, the liquid of interest can be filled selectively into the central hollow core of the HC-PCF (Figure 1). In doing so, the refractive index of the water-filled central hollow core can be higher than the effective refractive index of the cladding structure, as explained later. Thus, step-index guidance in the analyte solution could be achieved, which might allow Raman sensing in a very broad spectral range with various excitation wavelengths.

Due to the extremely high requirements on the fiber structure, broadband step index guidance in a water core was not demonstrated yet in transmission spectra, and existing work was limited to high refractive index solvents ($n_{\text{ethylene glycol}}$ = 1.43).[63] As water has a low refractive index of 1.33, an air cladding with a very low effective refractive index is needed in order to achieve step-index guiding in the fiber core. If the effective refractive index of the air cladding is higher than that of water, the HC-PCF is not suitable for Raman enhancement in aqueous solutions. This work explores for the first time broadband step-index guidance in water-filled hollow core photonic crystal fibers, demonstrates low-loss guidance experimentally in transmission spectra, and evaluates these new abilities of the sensor fiber for ultrasensitive and chemically selective fiber-enhanced Raman spectroscopy of clinically relevant concentrations of important antibiotic drugs.

■ MATERIALS AND METHODS

All chemicals were purchased from Sigma-Aldrich and used without further purification. The hollow core photonic crystal fibers were obtained from NKT. Raman spectra were acquired with a LabRam system (Horiba JobinYvon, HR800) equipped with liquid-nitrogen-cooled CCD detectors and different laser excitation wavelengths: λ = 532 nm (I_{Laser}= 100 mW at the sample), λ = 676 nm (I_{Laser}= 40 mW at the sample), and λ = 752 nm (I_{Laser}= 60 mW at the sample). An Olympus 20× objective was used for the measurements. In order to keep a stable optical coupling situation for Raman sensing, a custom-made fiber adapter was employed, which has an optical window for laser coupling into the HC-PCF[29] (Figure 2). An HPLC pump (Jasco PU-2085 Plus) was used to provide constant pressure and flow through the liquid media. The laser excitation light was focused into the fiber with an objective lens, and the backscattered Raman signal was collected by the same lens. Subsequently, the Raman signals were collected and analyzed with the spectrometer system. The transmission spectrum of the hollow fiber was analyzed with a broadband xenon light source and an optical spectrum analyzer (Ando, AQ-1425).

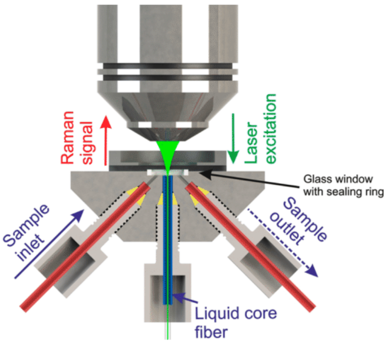

Figure 2. Schematic sketch of the fiber adapter assembly. The laser light is coupled into the fiber core through an optical window, and the analyte solution is pumped through the fiber by side connectors.

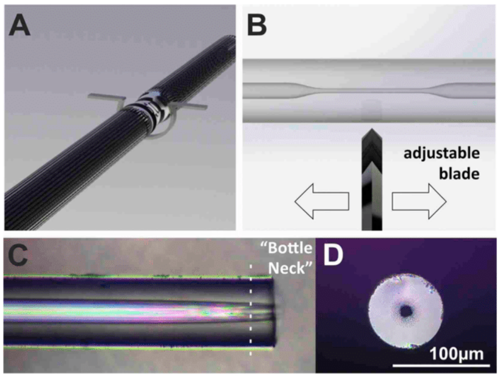

Figure 3. Sensor fiber preparation: The end of the hollow fiber was processed to provide a single channel in the fiber central hole. (A) Process step 1: The fiber is fixed on the fusion splicer and heated with an omega-shaped filament. With carefully tuned parameter, the air cladding is collapsed and the central hole is still open. (B) Process step 2: Cleaving of the HC-PCF with an adjustable diamond blade. The fiber is precisely cleaved in the fusing region, and only a very short bottleneck remains. (C and D) The prepared sensor fiber end face has a flat facet and very short bottleneck (typically 20 μm).

In order to achieve precise quantification of antibiotics at micromolar concentrations, the Raman peak of water was utilized as an internal standard.[29,68] The measured Raman spectra were first normalized to the 1645 cm^{-1} Raman band of the solvent water, and then the water background was subtracted from the spectra. As the solvent concentration could be considered as constant in all low-concentrated solutions, this normalization is able to cancel out all random factors (fluctuations in laser intensity and optical coupling, etc.). The signal-to-noise ratio (SNR) was calculated from the height of the Lorentzian fit of the target peaks and the root-mean-square (RMS) values of the baseline. The limit-of-detection (LOD) was derived when the SNR was equal to 3. The exposure time for the moxifloxacin measurements was 60 s, and the sensor fiber had a length of 20 cm.

■ RESULTS AND DISCUSSION

In this contribution the preparation and the optical properties of a hollow core sensor fiber are first thoroughly analyzed. Broadband step-index guiding in aqueous media is demonstrated and successively exploited for highly sensitive Raman sensing across the whole visible and near-infrared (NIR) range. These unique abilities are exploited for highly sensitive analysis of the important antibiotic moxifloxacin at clinically relevant levels.

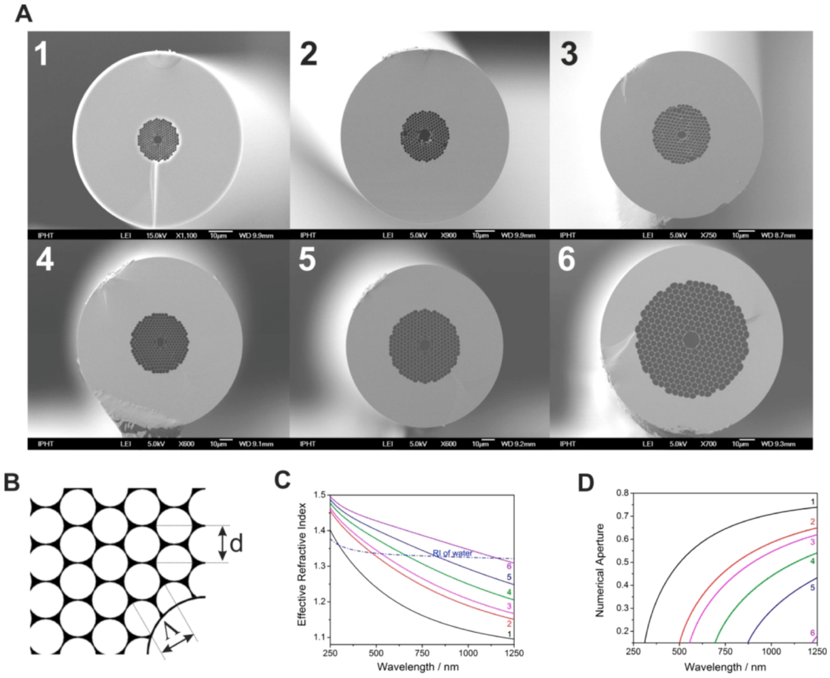

Figure 4. Comparison of several possible hollow core photonic crystal fibers. (A) Electron microscopic images of the cross sections of different HC-PCFs. (B) Schematic sketch of the fiber cross section and assignment of the paramters Λ (pitch size) and d (hole diameter). The filling fraction (R) can be calculated as $R = \frac{\pi}{2\sqrt{3}}\left(\frac{d}{\Lambda}\right)^2$. (C) Predicted effective refractive indices of the hollow core photonic crystal fibers. Parameters: 1: $\Lambda = 1.02$ μm, $R = 73.5\%$; 2: $\Lambda = 1.60$ μm, $R = 70.2\%$; 3: $\Lambda = 1.77$ μm, $R = 67.1\%$; 4: $\Lambda = 2.20$ μm, $R = 64.0\%$; 5: $\Lambda = 2.75$ μm, $R = 61.0\%$; 6: $\Lambda = 3.80$ μm, $R = 58.0\%$. The effective refractive index needs to be lower than that of water in order to provide step-index guidance. (D) Numerical apertures (NA) at various wavelength of all hollow core photonic crystal fibers based on the effective refractive indices of the fiber cladding and water.

Sensor Fiber Preparation. In order to fill the liquid sample selectively into the central hollow core of the fiber, it is necessary to seal the air holes in the cladding region and prevent their undesired filling. The sealing at both ends of the HC-PCF provides a single channel to the fiber central hole, while the main part of the sensor fiber remains unchanged. The most common technique for hollow fiber sealing is filling it with a polymer and subsequent curing.[69−74] However, this technique is not suitable in fiber-enhanced Raman spectroscopy (FERS) due to the strong fluorescence background from the polymer material itself. A more promising method is to collapse the air cladding with heat and thus to avoid the introduction of any foreign material into the fiber. In order to collapse the fiber cladding at the fiber ends, a fiber splicer can be employed to form a bottleneck at the fiber end.[52,63−65,75,76] The bottleneck region forms a glass capillary, which connects to the central hole of the HC-PCF. As water has a lower refractive index than that of glass, the length of the bottleneck should be minimized for the best optical coupling efficiency.

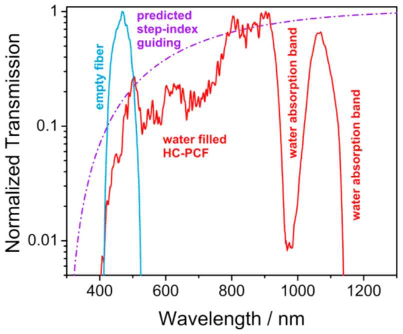

Figure 5. Transmission spectra of an empty and a selectively water-filled HC-440 fiber. The guiding mechanism of the empty HC-PCF is band gap guiding in a narrow spectral region from 400 to 520 nm. The specially prepared, selectively water-filled sensor fiber shows a tremendously increased broadband transmission spectrum from 400 nm up to the NIR range. The water absorption bands appear at 0.98 and 1.2 μm. The calculated transmission spectrum is the ideal broadband transmission spectrum of step-index guiding (shown as a dashed line) and in principal agreement with the experimentally acquired spectrum.

In this work, we developed a novel two-step technique that maintains excellent optical guidance properties. Step 1: A piece of HC-PCF is fixed on the fiber splicer, and then heat is applied (Figure 3A). The fine-structured air cladding in the fiber melts and collapses under the influence of the heat. As the central hollow core of the HC-PCF is larger than the air cladding holes, more heat is needed to collapse the central hollow core. The settings of the heating parameters have to be chosen precisely in order to find the optimal conditions for the respective fiber cladding. When the heating process is insufficient, the microstructure is not completely collapsed and the liquid sample can leak into the microstructure. If the heating process is too strong, the central hollow core size shrinks, or it is even completely sealed. Thus, the heating parameters were adjusted to collapse only the air cladding and keep the central hole open (Figure 3C and D). The fiber ends were prepared on a Vytran FFS-2000 fiber splicer with a standard tungsten filament, at 16.7 W heating strength and 0.9 s heating duration. During the process, the filament and the fiber were protected by 0.4 L/min argon flow. Step 2: The fiber is precisely cleaved as close as possible to the edge of the fused region with a customized cleaving setup, consisting of a microscope and an adjustable diamond blade (Figure 3B). With precise adjustment of the blade position, flat fiber ends were obtained and a minimized length of the bottleneck of typically only 20 μm was achieved (Figure 3C). In the conventional one-step method,[63] a long bottleneck (more than 200 μm) is inevitable, as the heat always influences a large part of the fiber. However, such a long bottleneck region is a main source of power loss and additional background signal[52] from the silica material of the fiber itself. In this novel two-step method, the precise cleaving process avoids a long bottleneck and therefore ensures high-quality optical guidance and coupling of the fiber ends (Figure 3C and D).

Index-Guiding Mechanism of the Selectively Filled HC-PCF. The numerical aperture (NA) of an index-guiding fiber can be calculated from the refractive indices of the fiber core and the cladding. In a HC-PCF, the effective refractive

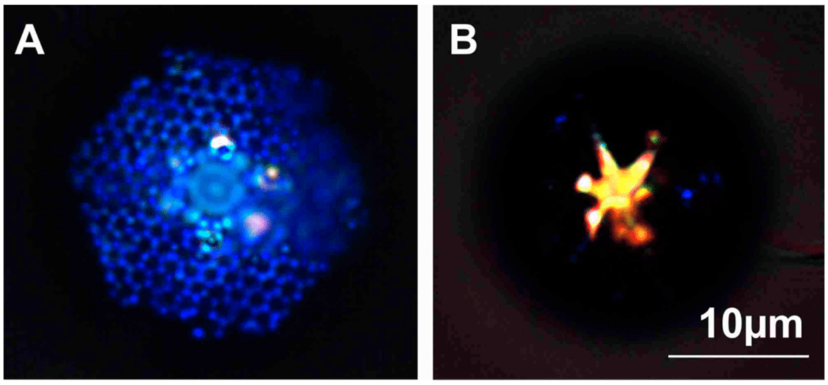

Figure 6. Light guidance in the empty fiber and the selectively filled fibers. (A) The air-filled fiber provides spectrally narrow light guidance in the blue and violet region (see Figure 5), based on the photonic band gap effect. (B) The fiber with a selectively water-filled central hollow core shows broadband light guidance (see Figure 5), based on the step index effect.

index of the cladding depends on the air−silica lattice geometry and the air fill fraction.[77] The effective refractive index can be predicted numerically according to the fiber pitch size (Λ), the air-filling ratio (R), and the wavelength (λ)[77] (Figure 4B). In doing so, the effective refractive indices for various possible geometries of HC-PCFs were calculated (Figure 4C). A low effective refractive index of a HC-PCF (high numerical aperture) is preferred, as it governs the performance of the light confinement in the liquid core. The refractive index of the cladding should at least be lower than that of water ($n = 1.33$) in order to form a step-index liquid guidance for measurements in aqueous samples. The calculation of the NAs of different types of HC-PCF (Figure 4A) at various wavelengths shows that only fiber HC-440 (number 1 in Figure 4) provides a high NA across the whole visible−NIR spectral range (Figure 4D).

The transmission spectra of an empty (air-filled) and a selectively water-filled HC-440 fiber show the expected guidance mechanisms (Figure 5). The empty hollow fiber shows band gap guidance in a narrow spectral region from 400 to 520 nm (Figure 5). However, the specially modified sensor fiber with a selectively water-filled central hollow core provides a tremendously improved broadband transmission spectrum from 400 nm up to the NIR range (Figure 5). The transmission of the fiber was calculated based on the acceptance angle (dashed line in Figure 5) and shows the theoretical broadband transmission spectrum for step-index guiding (Figure 5). The mismatch between the theoretical and experimentally acquired spectra around 400 nm can be caused by the low intensity of the light source and the light absorption of the glass material at this wavelength. The water absorption bands appear at 0.98 and 1.2 μm,[78] which are enhanced by the extended path length. The change from spectrally narrow band gap guidance in the blue/violet region (Figure 6A) to spectrally broadband step-index guidance (Figure 6B) can also nicely be seen by visual inspection of the fiber transmission spectra. These results confirm that the light guiding mechanism of the designed sensor fiber is based on step-index guiding in the fiber core. The wide spectral range of the step-index guiding in the sensor fiber provides excellent abilities for Raman sensing at various excitation wavelengths and for Raman sensing up to the high-wavenumber range. The specially prepared sensor fiber is thus perfectly suited for Raman sensing of antibiotics in aqueous media.

Proof of Principle Studies. In the first step, the sensor fiber was tested with ethanol in order to benchmark the performance of the enhancement of the Raman signals. The refractive index of ethanol (1.36) is close to that of aqueous solutions and is much lower than that of glass material. Ethanol shows strong Raman scattering with an intense Raman band at 880 cm^{-1} (νC−O−O symmetric stretching), which was selected for the quantification of the Raman enhancement. The enhanced Raman signal provided by the sensor fiber was compared with conventional Raman spectra, which were taken with identical experimental parameters. Thus, the conventional spectra were first acquired by focusing the laser in the bulk volume of the liquid sample without fiber installation, and then the HC-PCF was included and the fiber-enhanced Raman spectra were taken. The Raman spectra of ethanol show an enhancement of approximately 1 order of magnitude with a range of different excitation wavelengths (λ_{exc} = 532 nm, λ_{exc} = 676 nm, and λ_{exc} = 752 nm) across the whole visible and NIR range (Figure 7).

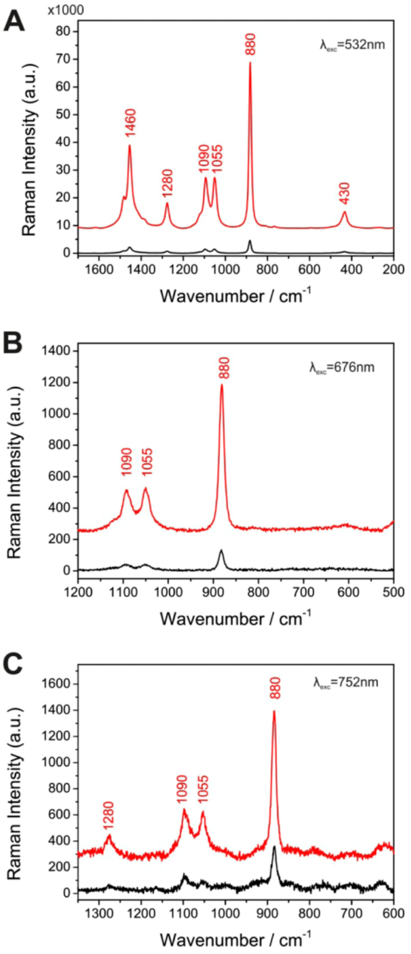

Figure 7. Comparison of the fiber-enhanced Raman spectra (red) with conventional Raman sensing (black) of ethanol with excitation wavelengths 532 nm (A), 676 nm (B), and 752 nm (C), respectively. Thus, the strong enhancement of the Raman signals can be provided over a wide spectral range. The spectra in the graph are slightly vertically shifted for the sake of clarity.

Fiber-Enhanced Raman Spectroscopy of Moxifloxacin. The fluoroquinolone moxifloxacin is a fourth-generation antibacterial agent against Gram-positive and anaerobic bacteria. The moxifloxacin concentration is reported to be 8 μM in plasma[79] in the first 4 h after a single 400 mg oral administration. As the elimination of moxifloxacin is mainly by renal excretion, and approximately 45% of moxifloxacin is excreted as unchanged drug, the moxifloxacin concentration in urine is found to be 161 μM after a single standard dose.[80] As quinolone antibiotics penetrate into lung tissues more efficiently than β-lactams,[81] they have good efficacy in the treatment of inflammation in the lungs (pneumonia).[79] Moxifloxacin concentrations of 54 μM have been shown in epithelial lining fluid.[79] The intense characteristic Raman band detected at 1620 cm^{-1}, which is the νC═C

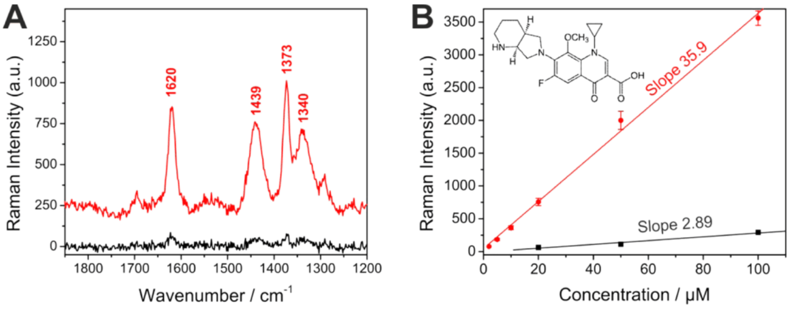

Figure 8. Fiber-enhanced Raman spectroscopy of antibiotics. (A) Comparison of the fiber-enhanced Raman spectrum (red) with the conventional Raman spectrum (black) of 20 μM moxifloxacin with λ_{exc} = 532 nm. The signal-to-noise ratios of the Raman peak at 1620 cm^{-1} (νC═C stretching vibration of the aromatic ring) was enhanced by 1 order of magnitude. The spectra in the graph are slightly vertically shifted for the sake of clarity. (B) Raman intensity dependency from the drug concentration (fiber-enhanced Raman spectrum (red), conventional (black)). A very good linearity and thus a robust calibration can be achieved. The inset shows the chemical structure of moxifloxacin.

stretching vibration of the aromatic ring, was chosen for the concentration study. The peak at 1373 cm^{-1} is an additional peak suitable for low-concentration sensing and is assigned to the stretching vibration of the quinolone ring system of moxifloxacin. The Raman spectra of a 20 μM solution of moxifloxacin, which are enhanced by the sensor fiber (red), show a 1 order of magnitude higher signal intensity in comparison to the conventional Raman spectra (black) of the same sample (Figure 8A). In order to show the abilities for quantification, a series of concentrations in the physiological range (from 1 μM to 1 mM) was prepared. The height of the Raman peaks at 1620 cm^{-1} shows excellent linearity to the moxifloxacin concentration (Figure 8B). Thus, the linear fits can be taken as a calibration function to predict the concentration of moxifloxacin in an unknown sample based on the Raman peak measurement. The higher sensitivity of the fiber-enhanced Raman sensing is clearly seen on the steeper slope of the linear fit of the Raman peak height (Figure 8B), indicating the great potential of FERS as an analytical tool for the chemically selective sensing of moxifloxacin in low concentrations. For quantification purpose, the signal-to-noise ratio of the Raman peak was calculated from the Raman signal (the height of the fitted Lorentzian peak) and the noise (which is calculated from the RMS values of the baseline). In summary, the limit-of-detection of moxifloxacin (SNR = 3) was improved down to 1.7 μM, very well in the clinically relevant range. Furthermore, only a volume of 4 nL of liquid sample was needed in the sensor fiber, providing great potential for minimally invasive clinical applications.

■ CONCLUSION

The abilities of novel elaborated hollow core photonic crystal fibers for light guidance in aqueous media and for the enhancement of Raman signals were thoroughly evaluated. The novel HC-PCF type of fiber consists of fused silica and thus outperforms conventional low-RI polymer fibers in terms of the optical properties. The abilities of broadband step-index light guidance in water were analyzed for various possible HC-PCFs, and it was found that extremely high requirements have to be fulfilled for the microstructure of the fiber cladding (fiber pitch size (Λ) and filling fraction (R)). Thus, only one fiber can provide a sufficient NA for efficient light guidance in the visible range. A novel fiber preparation technique was developed that maintains excellent optical guidance properties and allows for selective filling of the fiber hollow core. Strong enhancements could be achieved for the Raman spectra across the whole spectral range, with laser excitation wavelengths of 532, 676, and 752 nm.

The unique properties of the novel sensor fiber were applied for tracing the important antibiotic moxifloxacin down to concentrations of only 1.7 μM in a 4 nL sample volume. These results nicely demonstrate that FERS increases the sensitivity and reduces the demand of sample volume tremendously. This technique has therefore remarkable potential as a rapid and precise diagnostic tool for point-of-care monitoring of antibiotic levels in patients with severe sepsis and septic shock, enabling rapid dose adjustment that may improve the outcome of these critically ill patients.

■ AUTHOR INFORMATION

Corresponding Author
*E-mail: torsten.frosch@uni-jena.de, torsten.frosch@gmx.de.

ORCID
Torsten Frosch: 0000-0003-3358-8878

Notes

The authors declare no competing financial interest.

■ ACKNOWLEDGMENTS

Funding from the federal state of Thuringia and European Union (EFRE) is highly acknowledged (2015 FE 9012 and 2015-0021). M.W.P. was supported by a grant from the German Ministry of Education and Research (01KI1501).

■ REFERENCES

(1) Patel, G. P.; Balk, R. A. Systemic steroids in severe sepsis and septic shock. *Am. J. Respir. Crit. Care Med.* **2012**, *185*, 133−139.

(2) Vazquez-Grande, G.; Kumar, A. Optimizing antimicrobial therapy of sepsis and septic shock: focus on antibiotic combination therapy. *Semin. Respir. Crit. Care Med.* **2015**, *36*, 154−166.

(3) Seymour, C. W.; Liu, V. X.; Iwashyna, T. J.; Brunkhorst, F. M.; Rea, T. D.; Scherag, A.; Rubenfeld, G.; Kahn, J. M.; Shankar-Hari, M.; Singer, M.; Deutschman, C. S.; Escobar, G. J.; Angus, D. C. Assessment of Clinical Criteria for Sepsis: For the Third International Consensus Definitions for Sepsis and Septic Shock (Sepsis-3). *JAMA* **2016**, *315*, 762−774.

(4) Engel, C.; Brunkhorst, F. M.; Bone, H. G.; Brunkhorst, R.; Gerlach, H.; Grond, S.; Gruendling, M.; Huhle, G.; Jaschinski, U.;

DOI: 10.1021/acsphotonics.6b00688

John, S.; Mayer, K.; Oppert, M.; Olthoff, D.; Quintel, M.; Ragaller, M.; Rossaint, R.; Stuber, F.; Weiler, N.; Welte, T.; Bogatsch, H.; Hartog, C.; Loeffler, M.; Reinhart, K. Epidemiology of sepsis in Germany: results from a national prospective multicenter study. *Intensive Care Med.* **2007**, *33*, 606−618.

(5) Taccone, F. S.; Laterre, P. F.; Dugernier, T.; Spapen, H.; Delattre, I.; Wittebole, X.; De Backer, D.; Layeux, B.; Wallemacq, P.; Vincent, J. L.; Jacobs, F. Insufficient beta-lactam concentrations in the early phase of severe sepsis and septic shock. *Crit. Care* **2010**, *14*, R126.

(6) Taccone, F. S.; Hites, M.; Beumier, M.; Scolletta, S.; Jacobs, F. Appropriate antibiotic dosage levels in the treatment of severe sepsis and septic shock. *Curr. Infect. Dis. Rep.* **2011**, *13*, 406−415.

(7) Pletz, M. W.; Bloos, F.; Burkhardt, O.; Brunkhorst, F. M.; Bode-Boger, S. M.; Martens-Lobenhoffer, J.; Greer, M. W.; Stass, H.; Welte, T. Pharmacokinetics of moxifloxacin in patients with severe sepsis or septic shock. *Intensive Care Med.* **2010**, *36*, 979−983.

(8) Pea, F.; Viale, P.; Furlanut, M. Antimicrobial therapy in critically ill patients: a review of pathophysiological conditions responsible for altered disposition and pharmacokinetic variability. *Clin. Pharmacokinet.* **2005**, *44*, 1009−1034.

(9) Barlam, T. F.; Cosgrove, S. E.; Abbo, L. M.; MacDougall, C.; Schuetz, A. N.; Septimus, E. J.; Srinivasan, A.; Dellit, T. H.; Falck-Ytter, Y. T.; Fishman, N. O.; Hamilton, C. W.; Jenkins, T. C.; Lipsett, P. A.; Malani, P. N.; May, L. S.; Moran, G. J.; Neuhauser, M. M.; Newland, J. G.; Ohl, C. A.; Samore, M. H.; Seo, S. K.; Trivedi, K. K. Implementing an Antibiotic Stewardship Program: Guidelines by the Infectious Diseases Society of America and the Society for Healthcare Epidemiology of America. *Clin. Infect. Dis.* **2016**, *62*, e51−77.

(10) Steinmetz, T.; Eliakim-Raz, N.; Goldberg, E.; Leibovici, L.; Yahav, D. Association of vancomycin serum concentrations with efficacy in patients with MRSA infections: a systematic review and meta-analysis. *Clin. Microbiol. Infect.* **2015**, *21*, 665−673.

(11) Troke, P. F.; Hockey, H. P.; Hope, W. W. Observational study of the clinical efficacy of voriconazole and its relationship to plasma concentrations in patients. *Antimicrob. Agents Chemother.* **2011**, *55*, 4782−4788.

(12) Vishwanathan, K.; Bartlett, M. G.; Stewart, J. T. Determination of moxifloxacin in human plasma by liquid chromatography electrospray ionization tandem mass spectrometry. *J. Pharm. Biomed. Anal.* **2002**, *30*, 961−968.

(13) Möller, J. G.; Staß, H.; Heinig, R.; Blaschke, G. Capillary electrophoresis with laser-induced fluorescence: a routine method to determine moxifloxacin in human body fluids in very small sample volumes. *J. Chromatogr., Biomed. Appl.* **1998**, *716*, 325−334.

(14) Keiner, R.; Herrmann, M.; Kusel, K.; Popp, J.; Frosch, T. Rapid monitoring of intermediate states and mass balance of nitrogen during denitrification by means of cavity enhanced Raman multi-gas sensing. *Anal. Chim. Acta* **2015**, *864*, 39−47.

(15) Frosch, T.; Popp, J. Relationship between molecular structure and Raman spectra of quinolines. *J. Mol. Struct.* **2009**, *924−926*, 301−308.

(16) Keiner, R.; Gruselle, M. C.; Michalzik, B.; Popp, J.; Frosch, T. Raman spectroscopic investigation of (CO2)-C-13 labeling and leaf dark respiration of Fagus sylvatica L. (European beech). *Anal. Bioanal. Chem.* **2015**, *407*, 1813−1817.

(17) Jochum, T.; Michalzik, B.; Bachmann, A.; Popp, J.; Frosch, T. Microbial respiration and natural attenuation of benzene contaminated soils investigated by cavity enhanced Raman multi-gas spectroscopy. *Analyst* **2015**, *140*, 3143−3149.

(18) Spiro, T. G. Resonance Raman spectroscopy. New structure probe for biological chromophores. *Acc. Chem. Res.* **1974**, *7*, 339−344.

(19) Bruckner, M.; Becker, K.; Popp, J.; Frosch, T. Fiber array based hyperspectral Raman imaging for chemical selective analysis of malaria-infected red blood cells. *Anal. Chim. Acta* **2015**, *894*, 76−84.

(20) Keiner, R.; Frosch, T.; Hanf, S.; Rusznyak, A.; Akob, D. M.; Kusel, K.; Popp, J. Raman Spectroscopy-An Innovative and Versatile Tool To Follow the Respirational Activity and Carbonate Biomineralization of Important Cave Bacteria. *Anal. Chem.* **2013**, *85*, 8708−8714.

(21) Frosch, T.; Keiner, R.; Michalzik, B.; Fischer, B.; Popp, J. Investigation of Gas Exchange Processes in Peat Bog Ecosystems by Means of Innovative Raman Gas Spectroscopy. *Anal. Chem.* **2013**, *85*, 1295−1299.

(22) Hanf, S.; Fischer, S.; Hartmann, H.; Keiner, R.; Trumbore, S.; Popp, J.; Frosch, T. Online investigation of respiratory quotients in Pinus sylvestris and Picea abies during drought and shading by means of cavity-enhanced Raman multi-gas spectrometry. *Analyst* **2015**, *140*, 4473−4481.

(23) Jochum, T.; von Fischer, J. C.; Trumbore, S.; Popp, J.; Frosch, T. Multigas Leakage Correction in Static Environmental Chambers Using Sulfur Hexafluoride and Raman Spectroscopy. *Anal. Chem.* **2015**, *87*, 11137−11142.

(24) Frosch, T.; Schmitt, M.; Popp, J. Raman spectroscopic investigation of the antimalarial agent mefloquine. *Anal. Bioanal. Chem.* **2007**, *387*, 1749−1757.

(25) Frosch, T.; Schmitt, M.; Popp, J. In situ UV resonance Raman micro-spectroscopic localization of the antimalarial quinine in cinchona bark. *J. Phys. Chem. B* **2007**, *111*, 4171−4177.

(26) Frosch, T.; Schmitt, M.; Schenzel, K.; Faber, J. H.; Bringmann, G.; Kiefer, W.; Popp, J. In vivo localization and identification of the antiplasmodial alkaloid dioncophylline A in the tropical liana Triphyophyllum peltatum by a combination of fluorescence, near infrared Fourier transform Raman microscopy, and density functional theory calculations. *Biopolymers* **2006**, *82*, 295−300.

(27) Frosch, T.; Popp, J. Structural analysis of the antimalarial drug halofantrine by means of Raman spectroscopy and density functional theory calculations. *J. Biomed. Opt.* **2010**, *15*, 041516.

(28) Yan, D.; Domes, C.; Domes, R.; Frosch, T.; Popp, J.; Pletz, M. W.; Frosch, T. Fiber enhanced Raman spectroscopic analysis as a novel method for diagnosis and monitoring of diseases related to hyperbilirubinemia and hyperbiliverdinemia. *Analyst* **2016**, *141*, 6104−6115.

(29) Frosch, T.; Yan, D.; Popp, J. Ultrasensitive fiber enhanced UV resonance Raman sensing of drugs. *Anal. Chem.* **2013**, *85*, 6264−6271.

(30) Frosch, T.; Meyer, T.; Schmitt, M.; Popp, J. Device for Raman difference spectroscopy. *Anal. Chem.* **2007**, *79*, 6159−6166.

(31) Frosch, T.; Schmitt, M.; Noll, T.; Bringmann, G.; Schenzel, K.; Popp, J. Ultrasensitive in situ tracing of the alkaloid dioncophylline A in the tropical liana Triphyophyllum peltatum by applying deep-UV resonance Raman microscopy. *Anal. Chem.* **2007**, *79*, 986−993.

(32) Hanf, S.; Bogozi, T.; Keiner, R.; Frosch, T.; Popp, J. Fast and highly sensitive fiber-enhanced Raman spectroscopic monitoring of molecular H2 and CH4 for point-of-care diagnosis of malabsorption disorders in exhaled human breath. *Anal. Chem.* **2015**, *87*, 982−988.

(33) Bogozi, T.; Popp, J.; Frosch, T. Fiber-enhanced Raman multi-gas spectroscopy: what is the potential of its application to breath analysis? *Bioanalysis* **2015**, *7*, 281−284.

(34) Hanf, S.; Keiner, R.; Yan, D.; Popp, J.; Frosch, T. Fiber-enhanced Raman multigas spectroscopy: a versatile tool for environmental gas sensing and breath analysis. *Anal. Chem.* **2014**, *86*, 5278−5285.

(35) Walrafen, G. E.; Stone, J. Intensification of Spontaneous Raman Spectra by Use of Liquid Core Optical Fibers. *Appl. Spectrosc.* **1972**, *26*, 585−589.

(36) Yin, J.-H.; Xiao, Z.-Y.; Li, Z.-W. Ultralow concentration β-carotene molecule detection by liquid-core optical fiber resonance Raman spectroscopy. *Vib. Spectrosc.* **2012**, *62*, 7−9.

(37) Görner, H.; Maier, M.; Kaiser, W. Raman gain in liquid-core fibers. *J. Raman Spectrosc.* **1974**, *2*, 363−371.

(38) Mackenzie, S. J.; Dakin, J. P. In *Internally Teflon-AF Coated Capillary Cell for Optical Fibre Remote Spectroscopy, Lasers and Electro-optics Europe, 1996*; CLEO/Europe, Sept 8−13, 1996; 1996; pp 206−206.

(39) Altkorn, R.; Koev, I.; Gottlieb, A. Waveguide capillary cell for low-refractive-index liquids. *Appl. Spectrosc.* **1997**, *51*, 1554−1558.

(40) Sugiya, K.; Harada, M.; Okada, T. Water-ice chip with liquid-core waveguide functionality. Toward lab on ice. *Lab Chip* **2009**, *9*, 1037−1039.

DOI: 10.1021/acsphotonics.6b00688

(41) Gopalakrishnan, N.; Sagar, K. S.; Christiansen, M. B.; Vigild, M. E.; Ndoni, S.; Kristensen, A. UV patterned nanoporous solid-liquid core waveguides. *Opt. Express* **2010**, *18*, 12903−12908.

(42) Persichetti, G.; Bernini, R. Water monitoring by optofluidic Raman spectroscopy for in situ applications. *Talanta* **2016**, *155*, 145−152.

(43) Persichetti, G.; Testa, G.; Bernini, R. Optofluidic jet waveguide enhanced Raman spectroscopy. *Sens. Actuators, B* **2015**, *207*, 732−739.

(44) Persichetti, G.; Testa, G.; Bernini, R. High sensitivity UV fluorescence spectroscopy based on an optofluidic jet waveguide. *Opt. Express* **2013**, *21*, 24219−24230.

(45) Knight, J. C.; Birks, T. A.; Russell, P. S. J.; de Sandro, J. P. Properties of photonic crystal fiber and the effective index model. *J. Opt. Soc. Am. A* **1998**, *15*, 748.

(46) Khetani, A.; Momenpour, A.; Alarcon, E. I.; Anis, H. Hollow core photonic crystal fiber for monitoring leukemia cells using surface enhanced Raman scattering (SERS). *Biomed. Opt. Express* **2015**, *6*, 4599−4609.

(47) Khetani, A.; Momenpour, T.; Monfared, A.; Tiwari, V. S.; Anis, H.; Riordon, J.; Godin, M. *Proc. SPIE* **2013**, 85760F-85760F−85766.

(48) Khetani, A.; Tiwari, V. S.; Harb, A.; Anis, H. Monitoring of heparin concentration in serum by Raman spectroscopy within hollow core photonic crystal fiber. *Opt. Express* **2011**, *19*, 15244−15254.

(49) Naji, M.; Khetani, A.; Lagali, N.; Munger, R.; Anis, H. A novel method of using hollow-core photonic crystal fiber as a Raman biosensor. *Proc. SPIE* **2008**, 68650E-68650E−68658.

(50) Antonopoulos, G.; Benabid, F.; Birks, T. A.; Bird, D. M.; Knight, J. C.; Russell, P. S. J. Experimental demonstration of the frequency shift of bandgaps in photonic crystal fibers due to refractive index scaling. *Opt. Express* **2006**, *14*, 3000−3006.

(51) Eftekhari, F.; Irizar, J.; Hulbert, L.; Helmy, A. S. A comparative study of Raman enhancement in capillaries. *J. Appl. Phys.* **2011**, *109*, 113104.

(52) Irizar, J.; Dinglasan, J.; Goh, J. B.; Khetani, A.; Anis, H.; Anderson, D.; Goh, C.; Helmy, A. S. Raman Spectroscopy of Nanoparticles Using Hollow-Core Photonic Crystal Fibers. *IEEE J. Sel. Top. Quantum Electron.* **2008**, *14*, 1214−1222.

(53) Yan, H.; Gu, C.; Yang, C.; Liu, J.; Jin, G.; Zhang, J.; Hou, L.; Yao, Y. Hollow core photonic crystal fiber surface-enhanced Raman probe. *Appl. Phys. Lett.* **2006**, *89*, 204101.

(54) Cox, F. M.; Argyros, A.; Large, M. C.; Kalluri, S. Surface enhanced Raman scattering in a hollow core microstructured optical fiber. *Opt. Express* **2007**, *15*, 13675−13681.

(55) Zhang, Y.; Shi, C.; Gu, C.; Seballos, L.; Zhang, J. Z. Liquid core photonic crystal fiber sensor based on surface enhanced Raman scattering. *Appl. Phys. Lett.* **2007**, *90*, 193504.

(56) Han, Y.; Oo, M. K. K.; Zhu, Y. N.; Xiao, L. M.; Demohan, M. S.; Jin, W.; Du, H., Index-guiding liquid-core photonic crystal fiber for solution measurement using normal and surface-enhanced Raman scattering. *Opt. Eng.* **2008**, *47*.04050210.1117/1.2902463

(57) Shi, C.; Lu, C.; Gu, C.; Tian, L.; Newhouse, R.; Chen, S.; Zhang, J. Z. Inner wall coated hollow core waveguide sensor based on double substrate surface enhanced Raman scattering. *Appl. Phys. Lett.* **2008**, *93*, 153101.

(58) Yang, X.; Shi, C.; Wheeler, D.; Newhouse, R.; Chen, B.; Zhang, J. Z.; Gu, C. High-sensitivity molecular sensing using hollow-core photonic crystal fiber and surface-enhanced Raman scattering. *J. Opt. Soc. Am. A* **2010**, *27*, 977−984.

(59) Yang, X.; Shi, C.; Newhouse, R.; Zhang, J. Z.; Gu, C. Hollow-Core Photonic Crystal Fibers for Surface-Enhanced Raman Scattering Probes. *Int. J. Opt.* **2011**, *2011*, 1−11.

(60) Yang, X.; Zhang, A. Y.; Wheeler, D. A.; Bond, T. C.; Gu, C.; Li, Y. Direct molecule-specific glucose detection by Raman spectroscopy based on photonic crystal fiber. *Anal. Bioanal. Chem.* **2012**, *402*, 687−691.

(61) Sun, J.; Chan, C. C.; Zhang, Y. F.; Shum, P. Analysis of hollow-core photonic bandgap fibers for evanescent wave biosensing. *J. Biomed. Opt.* **2008**, *13*, 054048.

(62) Antonoppolos, G.; Benabid, F.; Birks, T. A.; Bird, D. M.; Bouwmans, G.; Knight, J. C.; Russell, P. S. J. In *Experimental demonstration of refractive index scaling in photonic bandgap fibers*, Lasers and Electro-Optics, 2004. (CLEO), May 16−21, 2004; 2004; Vol. *2*, p 2.

(63) Smolka, S.; Barth, M.; Benson, O. Highly efficient fluorescence sensing with hollow core photonic crystal fibers. *Opt. Express* **2007**, *15*, 12783−12791.

(64) Smolka, S.; Barth, M.; Benson, O. Selectively coated photonic crystal fiber for highly sensitive fluorescence detection. *Appl. Phys. Lett.* **2007**, *90*, 111101.

(65) Nielsen, K.; Noordegraaf, D.; Sørensen, T.; Bjarklev, A.; Hansen, T. Selective filling of photonic crystal fibres. *J. Opt. A: Pure Appl. Opt.* **2005**, *7*, L13.

(66) Tiwari, V. S.; Khetani, A.; Momenpour, A.; Anis, H. Optimum Size and Volume of Nanoparticles Within Hollow Core Photonic Crystal Fiber. *IEEE J. Sel. Top. Quantum Electron.* **2014**, *20*, 205−212.

(67) Joannopoulos, J. D.; Meade, R. D.; Winn, J. N. *Photonic Crystals: Molding the Flow of Light*; Princeton University Press, 1995.

(68) Hehre, W. J. Self-Consistent Molecular-Orbital Methods. I. Use of Gaussian Expansions of Slater-Type Atomic Orbitals. *J. Chem. Phys.* **1969**, *51*, 2657.

(69) Huang, Y.; Xu, Y.; Yariv, A. Fabrication of functional microstructured optical fibers through a selective-filling technique. *Appl. Phys. Lett.* **2004**, *85*, 5182.

(70) Kuo, S. M.; Huang, Y. W.; Yeh, S. M.; Cheng, W. H.; Lin, C. H. Liquid crystal modified photonic crystal fiber (LC-PCF) fabricated with an un-cured SU-8 photoresist sealing technique for electrical flux measurement. *Opt. Express* **2011**, *19*, 18372−18379.

(71) Gerosa, R. M.; Bozolan, A.; de Matos, C. J. S.; Romero, M. A.; Cordeiro, C. M. B. Novel Sealing Technique for Practical Liquid-Core Photonic Crystal Fibers. *IEEE Photonics Technol. Lett.* **2012**, *24*, 191−193.

(72) De Matos, C. J.; Cordeiro, C. M.; Dos Santos, E. M.; Ong, J. S.; Bozolan, A.; Brito Cruz, C. H. Liquid-core, liquid-cladding photonic crystal fibers. *Opt. Express* **2007**, *15*, 11207−11212.

(73) Bennet, F. H.; Farnell, J. Waveguide arrays in selectively infiltrated photonic crystal fibres. *Opt. Commun.* **2010**, *283*, 4069−4073.

(74) Vieweg, M.; Gissibl, T.; Pricking, S.; Kuhlmey, B. T.; Wu, D. C.; Eggleton, B. J.; Giessen, H. Ultrafast nonlinear optofluidics in selectively liquid-filled photonic crystal fibers. *Opt. Express* **2010**, *18*, 25232−25240.

(75) Meneghini, C.; Caron, S.; Proulx, A.; Emond, F.; Paradis, P.; Pare, C.; Fougeres, A.; Poulin, A. C. J. Determination of Ethanol Concentration by Raman Spectroscopy in Liquid-Core Microstructured Optical Fiber. *IEEE Sens. J.* **2008**, *8*, 1250−1255.

(76) Xiao, L.; Jin, W.; Demokan, M.; Ho, H.; Hoo, Y.; Zhao, C. Fabrication of selective injection microstructured optical fibers with a conventional fusion splicer. *Opt. Express* **2005**, *13*, 9014−9022.

(77) Mahnke, C.; Mitschke, F. A useful approximation for the cladding index of holey fibers. *Appl. Phys. B: Lasers Opt.* **2010**, *99*, 241−245.

(78) George, M.; Hale, M. R. Q. Optical Constants of Water in the 200-nm to 200-μm Wavelength Regin. *Appl. Opt.* **1973**, *12*, 555−563.

(79) Soman, A.; Honeybourne, D.; Andrews, J.; Jevons, G.; Wise, R. Concentrations of moxifloxacin in serum and pulmonary compartments following a single 400 mg oral dose in patients undergoing fibre-optic bronchoscopy. *J. Antimicrob. Chemother.* **1999**, *44*, 835−838.

(80) Wagenlehner, F. M.; Kees, F.; Weidner, W.; Wagenlehner, C.; Naber, K. G. Concentrations of moxifloxacin in plasma and urine, and penetration into prostatic fluid and ejaculate, following single oral administration of 400 mg to healthy volunteers. *Int. J. Antimicrob. Agents* **2008**, *31*, 21−26.

(81) Honeybourne, D.; Andrews, J. M.; Ashby, J. P.; Lodwick, R.; Wise, R. Evaluation of the penetration of ciprofloxacin and amoxycillin into the bronchial mucosa. *Thorax* **1988**, *43*, 715−719.

DOI: 10.1021/acsphotonics.6b00688
ACS Photonics XXXX, XXX, XXX−XXX

Acknowledgements

I would like to start by thanking Prof. Jürgen Popp for the opportunity to work in the research group. Many thanks go to Dr. Torsten Frosch for the supervision, creative ideas, and constructive discussions. He helps me improve all skills related to this research work and gives me the opportunity to take part in many different projects.

I am deeply grateful to Christian Domes, Robert Domes, Andreas Knebl, Sebastian Wolf, Timea Frosch, Anna Sieburg, Annika Düver, Robert Keiner and Stefan Hanf for their support with the laboratory experiments and literature research. I would like to also thank Tycho Kirchner for the nice collaboration and the help with Labview programming. Many thanks to my colleagues for the very nice work: Markus Lindner, Maximilian Dorn, Elisabeth Wyrwich. I am also grateful to Anka Schwuchow for her help with fiber characterization.

Last, but not least, I would like to thank my family for their unconditional, unlimited support and trust.

Curriculum Vitae

Selbständigkeitserklärung

Ich erkläre, dass ich die vorliegende Arbeit selbständig und unter Verwendung der angegebenen Hilfsmittel, persönlichen Mitteilungen und Quellen angefertigt habe.

Ort, Datum   Unterschrift des Verfassers